# Scintillation Screen Materials for Beam Profile Measurements of High Energy Ion Beams

Szintillator Materialien zur Profilmessung hochenergetischer Ionenstrahlen

Zur Erlangung des akadamischen Grades eines Doktor rerum naturalium (Dr. rer. nat) genehmigte Dissertation von M.Sc. Renuka Krishnakumar aus Karur
Darmstadt 2016 - D 17

TECHNISCHE UNIVERSITÄT DARMSTADT

Fachbereich Material-und Geowissenschaften
Fachgebiet Materialanalytik

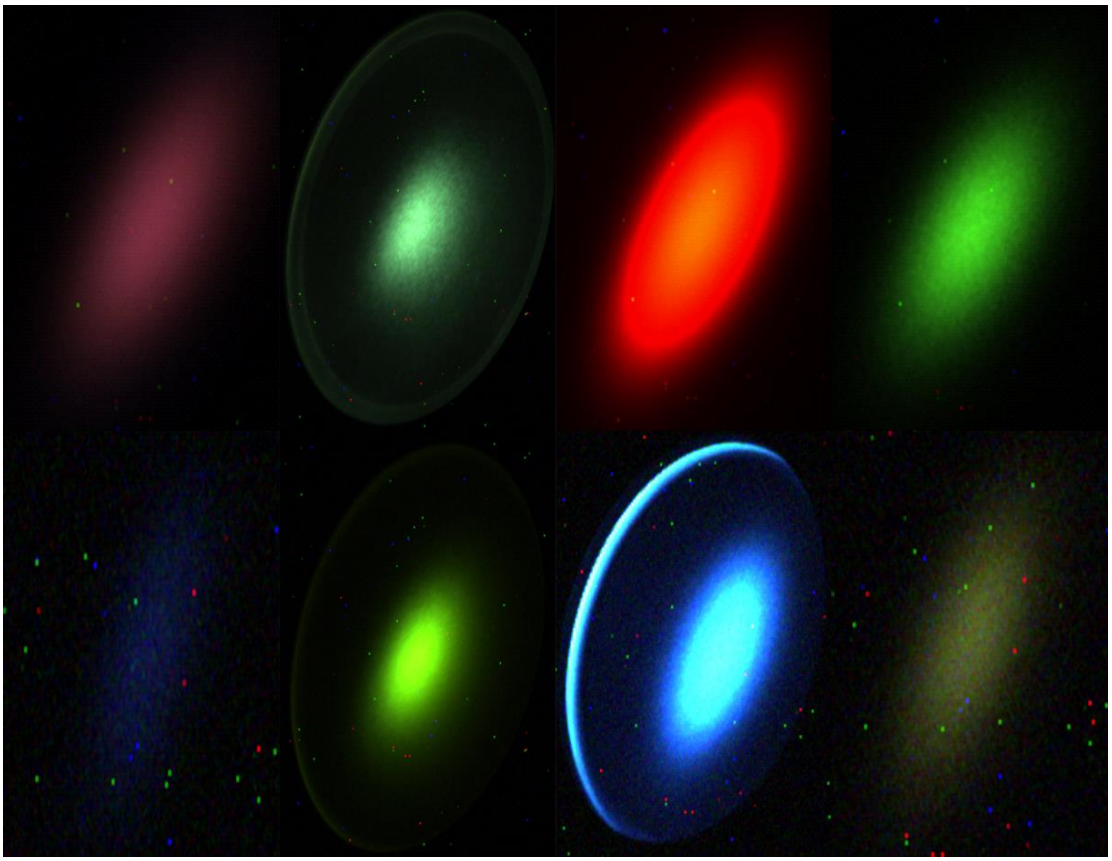

**Scintillation Screen Materials for Beam Profile Measurements of High Energy Ion Beams.**

Szintillator-Materialien zur Profilmessung hochenergetischer Ionenstrahlen

Genehmigte Dissertation von M.Sc. Renuka Krishnakumar aus Indien

1. Gutachten: Prof. Dr. rer. nat. Wolfgang Ensinger

2. Gutachten: Prof. Dr. phil. Christina Trautmann

Tag der Einreichung: 08.12.2014

Tag der Prüfung: 26.04.2016

Darmstadt- D17



# Erklärung zur Dissertation

Hiermit versichere ich, die vorliegende Dissertation ohne Hilfe Dritter nur mit den angegebenen Quellen und Hilfsmitteln angefertigt zu haben. Alle Stellen, die aus Quellen entnommen wurden, sind als solche kenntlich gemacht. Diese Arbeit hat in gleicher oder ähnlicher Form noch keiner Prüfungsbehörde vorgelegen.

Darmstadt, den 22.06.2016

_____

(K. Renuka)

# 1 Contents


**1. Contents** **1**

**Abstract** **5**

**List of Figures** **7**

**List of Tables** **10**

**2. Introduction** **11**

2.1 Beam diagnostics 11

2.1.1 Motivation 12

2.2 GSI Accelerators 13

2.3 FAIR facility 14

**3. Theory** **17**

3.1 Interaction of charged particles with matter 17

3.1.1 Electronic and nuclear energy loss 17

3.1.2 Bragg curve 19

3.2 Scintillation 20

3.3 Types of Scintillators 21

3.3.1 Classification of scintillators 21

3.3.2 Self activated materials 21

3.3.3 Activated materials 21

3.3.4 Cross luminescent materials 21

3.4 Scintillation mechanism 22

3.4.1 Energy bands in materials 22

3.4.2 Scintillation light yield 22

3.4.3 Mechanism of scintillation 23

3.4.4 Harmonic oscillator model 26

3.4.5 Scintillation decay and non-radiative decays 28

3.4.6 Defects and trappings 29

3.4.7 Presence of destructive ions 29

3.4.8 Self-trapping of excitations 30

3.4.9 Interaction between the adjacent excitations 31
3.5 Raman spectroscopy 31
3.5.1 Basic principle 31
3.6 X-ray diffraction 33

**4. Experiments 35**
4.1 Diagnostic devices 35
4.1.1 High Energy Beam Transport line (HEBT) 35
4.1.2 HTP beam line 35
4.1.3 Beam intensity measurement 37
4.1.4 Ionization Chamber (IC) 38
4.1.5 Secondary Electron Monitor (SEM) 39
4.1.6 Multi Wire Proportional Chamber (MWPC) 40
4.2 Scintillation screens 42
4.2.1 Standard device 42
4.2.2 Choice of the materials 42
4.2.3 Materials investigated 42
4.2.4 Beam parameters 45
4.2.5 Energy loss in the beam line 45
4.3 Experimental setup 47
4.3.1 Hardware 47
4.3.2 Camera and optics 51
4.3.3 Camera trigger 52
4.3.4 Data acquisition 53
4.3.5 Extended measurement 55
4.4 Data analysis 58
4.4.1 Quantitative characterization 58
4.4.2 Projections and background subtraction 59
4.4.3 Relative and absolute light yield 60
4.4.4 Performed algorithms 61
4.5 Comparison of algorithms 64
4.6 Raman spectroscopy 67
4.7 X-ray diffraction 67
4.8 UV-Vis Absorption spectroscopy 68

**5. Results and Discussion 69**
5.1 Linearity measurements 69
5.1.1 Preliminary experiment 69
5.1.2 Results from Carbon ions 69
5.1.3 Results from Neon ions 73

5.1.4 Results from Argon ions 74
5.1.5 Results from Uranium ions 80
5.1.6 Results from Tantalum ions 85
5.1.7 Comparison with reference detector 85
5.1.8 Relative and absolute comparisons 86
5.2 Performance concerning possible irradiation damage 88
5.2.1 Low energy ion beam measurements 89
5.2.2 Measurements with moderate beam energy 90
5.2.3 Stability under reduced intensity 94
5.3 Radiation modification analysis 97
5.3.1 Powder screens 97
5.3.2 Ceramics samples 99
5.3.3 X-ray Diffraction analysis 101
5.3.4 Formation of color centers 103

**6. Summary and Outlook 105**

**7. Bibliography 109**

**Abbreviations 119**

**Appendix 121**

**Acknowledgement 134**

# Abstract

For the application as a transverse ion beam diagnostics device, various scintillation screen materials were analysed. The properties of the materials such as light output, image reproduction and radiation stability were investigated with the ion beams extracted from heavy ion synchrotron SIS-18. The ion species (C, Ne, Ar, Ta and U) were chosen to cover the large range of elements in the periodic table. The ions were accelerated to the kinetic energies of 200 MeV/u and 300 MeV/u extracted with 300 ms pulse duration and applied to the screens. The particle intensity of the ion beam was varied from $10^4$ to $10^9$ particles per pulse. The screens were irradiated with typically 40 beam pulses and the scintillation light was captured using a CCD camera followed by characterization of the beam spot. The radiation hardness of the screens was estimated with high intensity Uranium ion irradiation.

In the study, a linear light output for 5 orders of magnitude of particle intensities was observed from sensitive scintillators and ceramic screens such as $Al_2O_3$:Cr and $Al_2O_3$. The highest light output was recorded by CsI:Tl and the lowest one by Herasil. At higher beam intensity saturation of light output was noticed from Y and Mg doped $ZrO_2$ screens. The light output from the screen depends not only on the particle intensity but also on the ion species used for irradiation. The light yield (i.e. the light intensity normalised to the energy deposition in the material by the ion) is calculated from the experimental data for each ion beam setting. It is shown that the light yield for light ions is about a factor 2 larger than the one of heavy ions. The image widths recorded exhibit a dependence on the screens material and differences up to 50 % were registered.

On radiation stability analysis with high particle intensity of Uranium ions of about $6\times10^8$ ppp, a stable performance in light output and image reproduction was documented from $Al_2O_3$:Cr screen over 1000 pulses while slight saturation effects was noticed from some other screens. No considerable radiation induced damage for an irradiation by maximal fluence of $1.7\times10^{11}$ $cm^{-2}$ Uranium ions was seen in the samples except the formation of point defects and color centers. Among the investigated screens P43 ($Gd_2O_2S$:Tb) powder seems to be a good candidate up to certain energy deposition threshold while for very high intensity measurements $Al_2O_3$:Cr screens are recommended.

# Zusammenfassung

Es wurden verschiedene Leuchtschirm Materialien in Hinsicht auf ihren Einsatz für transversale Strahldiagnose untersucht. Materialeigenschaften wie Lichtausbeute, Abbildungseigenschaften und Strahlenhärte wurden mit Ionenstrahlen untersucht, die aus dem SIS-18 Synchrotron extrahiert wurden. Die Ionenarten (C, Ne, Ar, Ta und U) wurden ausgewählt, um einen großen Bereich von Elementen des Periodensystems abzudecken. Die Ionen wurden auf eine Energie von 200 MeV/u und 300 MeV/u beschleunigt, als Puls mit 300 ms Pulslänge extrahiert und auf die Leuchtschirme geschossen. Die Intensität des Ionenstrahls wurde von $10^4$ bis $10^9$ Teilchen pro Puls variiert. Typischerweise wurden die Leuchtschirme mit 40 Strahlpulsen bestrahlt, das Szintillationslicht von einer CCD Kamera aufgenommen und der Strahlfleck charakterisiert. Die Strahlenhärte der Leuchtschirme wurde mit einem hochintensiven Uranionen strahl abgeschätzt.

Die Untersuchungen ergaben eine lineare Lichtausbeute bei sensitiven und keramischen Szintillatoren wie $Al_2O_3$:Cr und $Al_2O_3$ über fünf Größenordnungen hinweg. Die höchste Lichtausbeute wurde mit CsI:Tl erziehlt, die niedrigste mit Herasil. Bei höheren Intensitäten ging die Lichtausbeute bei den Materialien Y- und Mg- dotiertes $ZrO_2$ in die Sättigung. Die Lichtausbeute der Leuchtschirme hängt nicht nur von der Partikelintensität ab, sondern auch von der Ionenart, die zur Bestrahlung verwendet wird. Die Lichtausbeute (z.B. die auf die Energiedeposition normierte Lichtausbeute) wurde aus den Experimentaldaten für jede Beschleunigereinstellung berechnet. Es wird gezeigt, dass die Lichtausbeute für leichte Ionen ca. um den Faktor zwei höher ist als bei schweren Ionen. Die gemessenen Strahlbreiten zeigen eine Abhängigkeit vom Leuchtschirmmaterial mit mehr als 50 % Abweichung.

Bis auf das Entstehen von Punktdefekten und Farbzentren konnte kein bedeutender strahlungsinduzierter Schaden an den Leuchtschirmen für eine Bestrahlung von maximal $1.7\times10^{11}$ $cm^{-2}$ Uran Ionen festgestellt werden. Unter den eruierten Leuchtschirmen scheint der P43 ($Gd_2O_2S$:Tb) ein guter Kandidat bis zu einer bestimmten Energiedeposition zu sein. Hochintensive Messungen können mit $Al_2O_3$:Cr Leuchtschirmen durchgeführt werden.

# List of Figures

Figure 2:1: The existing accelerator facility in GSI . ..... 13
Figure 2:2: The planned FAIR facility ..... 15

Figure 3:1. Electronic and nuclear energy loss vs. specific energy ..... 18
Figure 3:2: The electronic energy loss and Bragg peak. ..... 20
Figure 3:3: Schematic picture of scintillation mechanism in activated materials. ..... 22
Figure 3:4: The energy zones formation in semiconductors and insulators . ..... 23
Figure 3:5: Schematic representation of scintillation mechanism. ..... 24
Figure 3:6: General representation of relaxation of electronic excitations ..... 25
Figure 3:7: Symmetrical stretching vibration of a square planar complex. ..... 27
Figure 3:8: Scheme of luminescence transition in configurational coordinate diagram. ..... 27
Figure 3:9: Spectral absorption and luminescence depicting Stokes shift . ..... 28
Figure 3:10: The configurational coordinate diagram. ..... 29
Figure 3:11: Tunnelling effect from the lowest vibrational level ..... 30
Figure 3:12: The schematic representation of excitation and relaxation of Raman scattering. 32
Figure 3:13: Schematic diagram of X-ray diffractometer and the principle of diffraction ..... 33

Figure 4:1: The sketch of HEBT of SIS-18. ..... 36
Figure 4:2: Scheme of detector systems deployed for beam current measurement ..... 37
Figure 4:3: The ionization chamber installed in HEBT of GSI ..... 38
Figure 4:4: The schematic representation of the SEM detector.. ..... 39
Figure 4:5: The SEM detector installed in GSI HEBT line.. ..... 40
Figure 4:6: The schematic diagram of a MWPC detector.. ..... 41
Figure 4:7: The actual MWPC device used for transverse profile measurement. ..... 41
Figure 4:8: Schematic representation and the corresponding scintillation screen device. ..... 44
Figure 4:9 : Schematic representation of the experimental setup installed. ..... 47
Figure 4:10: The aluminium target holder with different scintillation screens. ..... 47
Figure 4:11: Auto CAD picture of the HTP beam line. ..... 49
Figure 4:12: The HTP beam line with beam diagnostics detectors and experimental setup. ... 50
Figure 4:13: The experimental setup used for ion beam profile measurements.. ..... 51
Figure 4:14: The resolution target used for calibration of the camera and optics. ..... 52
Figure 4:15: The spectral sensitivity of the CCD sensor and hysteresis curve ..... 52
Figure 4:16: Beam spot generated for measuring the vignetting. ..... 53
Figure 4:17: Screen shot of oscilloscope taken during experiments. ..... 54
Figure 4:18: Gain curve obtained for camera 1. ..... 55
Figure 4:19: Screen shot of the data acquisition system BeamView. ..... 56
Figure 4:20: Spill structure obtained from ABLASS ..... 56
Figure 4:21: Transmission gradient measured for ITOS NG4 grey filter. ..... 57
Figure 4:22: Modified experimental setup. ..... 57
Figure 4:23: Examples for higher statistical moments Skewness and Kurtosis ..... 59

Figure 4:24: (a) The beam spot obtained from P43 scintillation screen..... 60
Figure 4:25: The background image recorded before beam delivery ..... 61
Figure 4:26: (a) Image profile in horizontal direction after background subtraction. ..... 63
Figure 4:27: Image profiles obtained from $Al_2O_3$:Cr ..... 63
Figure 4:28: An example for curve fitting to measure the standard deviation.. ..... 64
Figure 4:29: Image widths obtained from the data obtained after background subtraction.... 65
Figure 4:30: Image widths calculated by reducing the light intensity (second algorithm) ..... 65
Figure 4:31: Image widths calculated by the third algorithm ..... 66
Figure 4:32: Image width obtained by performing Gaussian curve fits ..... 66
Figure 4:33: Schematic representation of Raman spectrometer ..... 67

Figure 5:1: Light output from various scintillation screens vs. particle intensity..... 70
Figure 5:2: Image width σ calculated using Gaussian fit (algorithm 4, Chapter 4.5)..... 71
Figure 5:3: Skewness calculated from the profiles acquired for the Carbon ion beam. ..... 71
Figure 5:4: Kurtosis calculated for Carbon ion beam image profiles. ..... 72
Figure 5:5: Normalized horizontal projection of the beam spot obtained from P43 ..... 72
Figure 5:6: Light output from various scintillation screens vs. particle intensity..... 74
Figure 5:7: The plot shows the relative error calculated ..... 75
Figure 5:8: Image width σ calculated using Gaussian fit. ..... 76
Figure 5:9: The skewness calculated from the profiles for Neon ion beam. ..... 76
Figure 5:10: The statistical moment kurtosis obtained for Neon ion beams of 295 MeV/u.... 77
Figure 5:11: Beam image profiles obtained from the scintillation screens. ..... 77
Figure 5:12: Normalised beam image profiles obtained from the scintillation screens..... 78
Figure 5:13: Light output obtained from selected scintillation screens.. ..... 79
Figure 5:14: Image width σ calculated using Gaussian fit (algorithm 4, Chapter 4.5) ..... 79
Figure 5:15: Kurtosis calculated for Argon ion beams.. ..... 80
Figure 5:16: Light output from several scintillation screens. ..... 82
Figure 5:17: Image width σ calculated using Gaussian fits ..... 83
Figure 5:18: (a) Kurtosis calculated from $ZrO_2$:Y using the reduced intensity ..... 84
Figure 5:19: Image profiles obtained from $ZrO_2$:Y at various particle intensities..... 84
Figure 5:20: Light output from various scintillation screens vs. particle intensity..... 85
Figure 5:21: Image width σ calculated using Gaussian fit. ..... 86
Figure 5:22: Comparison of Tantalum ion beam image profiles. ..... 87
Figure 5:23: The light yield per energy deposition by a single ion..... 88
Figure 5:24: Light output and image width obtained from aluminium oxide scintillators. ..... 90
Figure 5:25: Light output and image width calculated from selected scintillation screens. .... 91
Figure 5:26: Statistical moments calculated for the selected scintillation screens..... 92
Figure 5:27: Image profiles obtained from the screens at various pulse numbers. ..... 93
Figure 5:28: Image profiles obtained from P43 screen at different beam pulses. ..... 94
Figure 5:29: The statistical moments calculated for different screens for 300 MeV/u Uranium ion beams. ..... 95
Figure 5:30: Image profiles obtained from scintillation screens at different pulse numbers.... 96
Figure 5:31: Raman spectra of P43 powder screen. ..... 98
Figure 5:32: Raman spectra of P46 (YAG:Ce) powder screens.. ..... 98
Figure 5:33: (Top) Raman spectra obtained from $Al_2O_3$ irradiated with Ne, Ar and Ta ions; . 99
Figure 5:34: Raman spectra obtained from $Al_2O_3$ before and after exposing to laser ..... 101
Figure 5:35: The X-ray diffraction obtained from $Al_2O_3$ sample..... 102
Figure 5:36: The X-ray diffraction obtained from $Al_2O_3$:Cr sample ..... 103

Figure 5:37: Color centers formation in $Al_2O_3$, $ZrO_2$:Mg and $ZrO_2$:Y samples..... 103
Figure 5:38: Absorption spectra vs. photon energy recorded from $Al_2O_3$..... 104
Figure 5:39: Absorption spectra vs. photon energy recorded from $ZrO_2$:Y screens ..... 104

# List of Tables

Table 4:1: The list of beam diagnostics devices installed in HTP beam line ..... 37
Table 4:2: List of scintillation screens investigated for profile measurement ..... 43
Table 4:3: The energy loss in the vacuum windows and foils located in the beam line..... 46
Table 4:4: The list of ion beams and their parameters in chronological order. ..... 48
Table 5:1: Compilation of the relative light output from different scintillation materials ..... 87
Table 5:2: Calculated energy loss in materials by a single ion. ..... 89
Table 5:3: Electronic energy loss, nuclear energy loss and range of Uranium ions. ..... 97

# 2 Introduction

Particle accelerators are giant machines constructed around the world to conduct various research works in the branch of atomic physics, biophysics, elementary particle physics, material research etc. The physics of particle accelerators dates back to 1911 when Rutherford discovered nucleus by scattering alpha particles off a gold foil. The progress of particle accelerators took place in such a way that the accelerated particle energy MeV was reached in 1930s and TeV in 1990s. This development in accelerator physics serves as a basic tool for high energy physics experiments [1-2].

## 2.1 Beam diagnostics

One of the essential constituents of any accelerator facility is beam diagnostics. It is the integrated tool that displays behaviour and characteristic property of the ion beam. Diagnostic instruments are vital components for monitoring and assessing any beam experiment. The diagnostics devices provide information on the state of the beam and on the development of experiments performed on the beam, monitoring critical beam parameters such as current, size, energy, position, chromaticity and emittance [3]. The role of beam diagnostic instruments becomes more important during the commissioning of new accelerator facilities and after a long shutdown. The demands on a beam diagnostic system can vary due to the multifarious machines, such as LINACs, cyclotrons, synchrotrons, storage rings and transport lines. Further taking the wide range of particles, such as electrons, protons, anti-protons and heavy ions into account together with their different accelerating principles, it is necessary to develop adequate techniques for beam diagnostics [4]. In order to build an effective beam diagnostic instrument it is necessary to understand the physics of the beam and sensors which are used to detect the beam.

There is a variety of detectors such as ionization chamber, drift tubes, proportional counters, Cherenkov detectors, photomultiplier which are being deployed for beam diagnostics. These detectors are working based on the principle of particle detection [5-6]. Among these different methods, the particle detection systems using scintillation screens have specific advantages.

The basics of particle detection started in 1896 when Henri Becquerel noticed the radiation from Uranium salts blackening the photosensitive papers. X-ray films were used as particle detectors in early days. In 1903, Sir William Crookes accidentally discovered the first scintillation material by spilling highly radioactive radium bromide on some activated ZnS layers. A flash of light was produced due to the interaction of $\alpha$ particles produced from radium bromide with ZnS [6] and later this phenomena was called “scintillation” effect. After this event, scintillation screens were employed for particle detection. The scintillation process is one of the most useful phenomena for detecting ionizing radiation [7]. In accelerator facilities, scintillation screens are being used for the purpose of beam alignment [8-10]. In

daily operation, scintillation screens play an important role for guiding the beam from the ion source to different experimental locations. The advantage of deploying scintillation screens is their simplicity, cheapness and power of conviction. They produce a high resolution two-dimensional beam image upon irradiation.

### 2.1.1 Motivation

In beam diagnostics, the density distribution of particles over the horizontal and vertical co-ordinates is called beam profile [4]. Monitoring the beam profiles helps to understand the space charge effects. In accelerator facility, quadrupole and dipole magnets were installed in the beam line for beam transportation and the ion beam profiles are greatly influenced by these magnets. This leads to a necessary installation of devices to measure beam profiles at various positions in the beam line [4].

The basic aim of this work is to investigate different scintillation screen materials for beam diagnostics application. The transverse beam profile of the high energy ion beams were characterised using scintillation screens. The image reproduction behaviour of various scintillation screen materials such as ceramics, single crystals, powder screens and glass were analysed by irradiating the screens with different ion beams. The experiments were performed at GSI Helmholtz Centre for Heavy Ion Research, Darmstadt. The scintillation screens were irradiated with ions delivered by the heavy ion synchrotron SIS-18. The measurements were performed with different particle intensities ranging from $10^4$ to $10^9$ ppp (particles per pulse). In addition, the performance of the screens was also analysed with irradiation with the heaviest available ion Uranium with about $6x10^{11}$ ions to evaluate possible material modifications.

Due to the restricted amount of beam time available for the accelerator machine experiments, and the fluctuations in the ion source, the screens were irradiated with 1000 beam pulses of Uranium ion of particle intensity $6\times10^8$ ppp with 0.25 Hz repetition rate and the image reproduction behaviour on continuous irradiation was monitored. The total number of particles received by the scintillation screens after 1000 pulses ($6\times10^{11}$ ions in total) is in the order of maximum particles to be accelerated in the FAIR accelerators.

Along with the imaging properties investigation, an additional characterization of the scintillation screens was carried out in order to understand the modifications created by the ions in the scintillation screens at this experimental condition. The material characterization techniques such as Raman spectroscopy, X-ray diffraction and UV-Vis absorption spectroscopy were performed to analyse the radiation induced modifications in the scintillation screen materials.

In FAIR accelerators (under construction in Darmstadt), scintillation screens will be installed at about 40 locations for ion beam profile measurements. Even though the beam energy and the particle intensity of the ion beam of the FAIR accelerators are considerably higher than presently available SIS-18 energy level, the work may serve as pilot study about the profile reproduction behaviour of scintillation screens interacting with very high energetic ion beams.

## 2.2 GSI Accelerators

The GSI Helmholtz Centre for Heavy Ion Research has a unique heavy ion accelerator system established in 1969 in Darmstadt and funded by the Federal Republic of Germany and the state of Hessen. This facility is used by researchers from all over the world for experiments in nuclear, atomic physics, biophysics and material research. The accelerator facility consists of the following three components,

- UNIversal Linear ACcelerator UNILAC
- Heavy ion synchrotron SIS-18 (Schwer Ionen Synchrotron)
- Experimental Storage Ring ESR

The schematic diagram of the complete facility is shown in Figure 2.1.

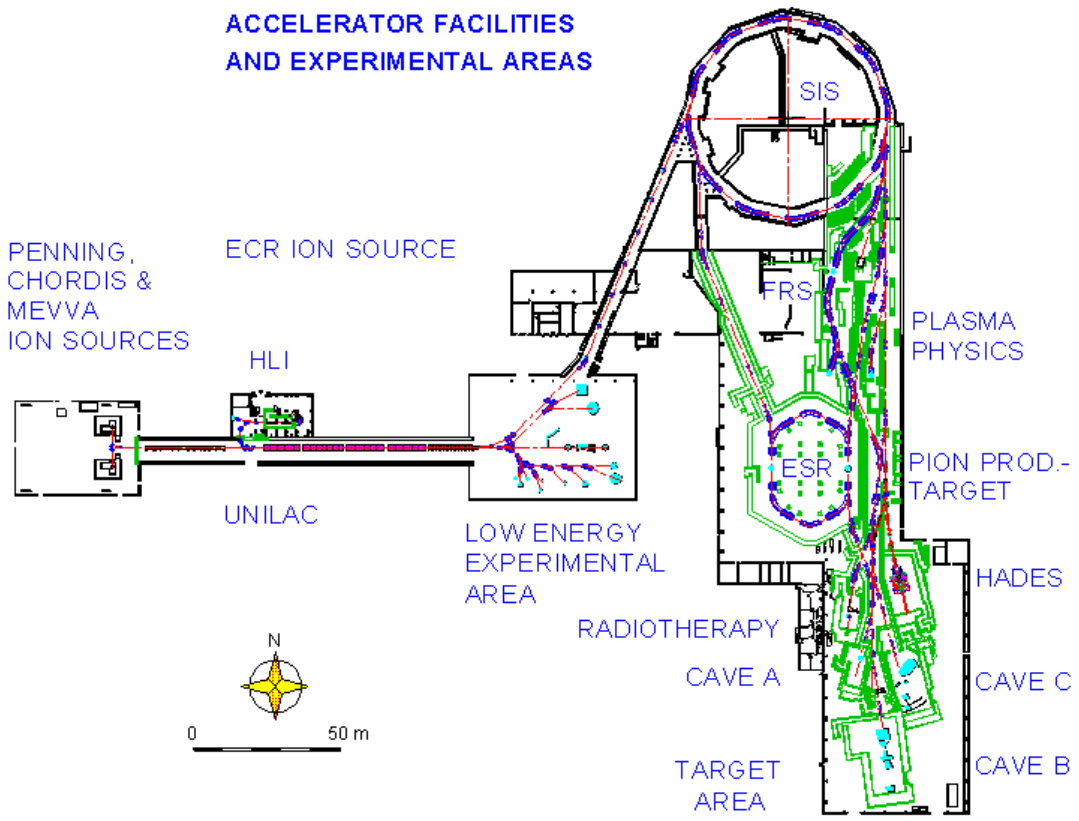


Figure 2.1: The existing accelerator facility in GSI [11]. Starting from left, the ion sources are followed by the UNILAC and experimental areas. The beam is injected into the synchrotron through the transfer channel. The accelerated ion beam from SIS is extracted and transported to different experimental areas (caves) and beam dumps.

The UNILAC is the starting point of ion acceleration. It comprises two injectors, the high current (HSI) and the high charge injector (HLI), an Alvarez drift tube Linac (DTL) and a gas stripper. The low current (Penning) and high current ion sources (MEVVA/MUCIS) deliver ions to HSI where the ions are accelerated by an RFQ system. Then the ions are passed through the drift tubes (DTL) where the ions gain a maximum energy of 11.4 MeV/u which corresponds to 15.5 % speed of light. The UNILAC accelerates all kinds of ion beams from proton to Uranium with a maximum pulse repetition rate of 50 Hz. The UNILAC has two functionalities; it provides ions for experiments at low energies and acts as an injector for the SIS-18. The foil stripper in the transfer channel provides high charge state ion beams for acceleration in the synchrotron [11].

The SIS-18 is designed to accelerate all kinds of ions to a kinetic energy up to 4 GeV/u. It consists of 12 identical sections each with 2 dipole and 3 quadrupole magnets forming a ring of circumference of 216 m. The SIS magnets are designed to have variable magnetic rigidity with maximum of 18 Tm. The acceleration of ions is acquired using two Radio-Frequency (RF) cavities with peak voltage of 16 kV in the frequency region of 0.8-5.6 MHz. An acceleration cycle in SIS consists of injection of the beam from UNILAC, acceleration by increasing the magnetic field and frequency followed by extraction. The ions from the synchrotron are extracted within minimum of $\mu s$ to maximum of some seconds. These high energy beams are delivered either directly to several experiments in the target area or to the ESR through the high energy beam transport line (HEBT). In addition, the slow extracted beams are transferred to the fragment separator (FRS) for the production of secondary ion beams [12].

## 2.3 FAIR facility

Besides the existing accelerator facility at GSI, the new Facility for Antiproton and Ion Research (FAIR) is under construction. It will be a next generation accelerator facility built with the experience gained with the existing facility in GSI. The heart of the new facility is a superconducting synchrotron with a circumference of about 1,100 meters. The SIS 100 will be the main accelerator with a magnetic rigidity of 100 Tm. A system of cooler-storage rings for effective beam cooling at high energies and various experimental halls will be connected to the facility. The synchrotron SIS 100 can accelerate heavy ions to a maximum energy of 20 GeV/u with particle intensities up to $10^{12}$ particles of Uranium. The existing SIS-18 will act as an injector for the FAIR SIS 100/300 accelerators. In addition to this, to accelerate Protons, a separate LINAC (p-linac) is being constructed which will be used for antiproton production. This SIS 100 and p- LINAC will provide high quality beams of antiprotons and radioactive beams for the experimental program [13] [14].

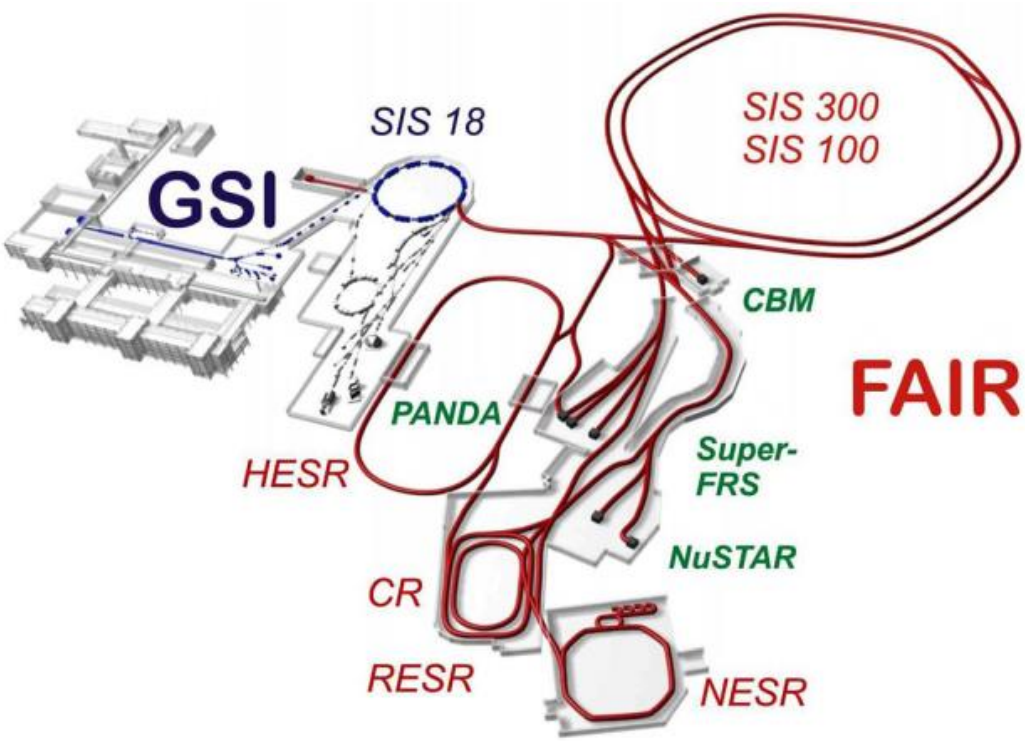


Figure 2.2: The planned FAIR facility [15]. The existing facility is marked in blue, the facilities under construction are marked in red and the experimental areas in grey.

# 3 Theory

In this section, the basics of charged particles interaction with matter, the energy loss in materials [7], [16] and the process of scintillation and its mechanism [17-21] are presented.

## 3.1 Interaction of charged particles with matter

The primary interaction of ions with the materials is through Coulomb forces between their positive charge and the negative charge of the electrons in the absorber medium. The passage of charged particles through matter is characterized by loss of energy and deflection of particle from incident direction. These effects are primarily the results of the following two processes:

- Inelastic collision with the atomic electrons of the material
- Elastic scattering from nuclei

These reactions occur many times per unit length of the material. The other possible reactions as a result of collision are:

- Cherenkov radiation
- Nuclear reactions
- Bremsstrahlung

The charged particle after entering into a medium starts interacting with electrons. The products of these collisions are the formation of excited atom or ions. If the energy of the free electrons formed during the collision is sufficient, delta electrons are formed leading to further encounter. The maximum energy that can be transferred from a charged particle to an electron is $E_{max}=4Em_o/m$, where $E$ is the energy of the particle, $m$ is mass of the particle and $m_0$ represents the mass of the electron.

The primary particle undergoes many of such interactions while passing through the material until it loses its energy completely and thermalizes. The net effect is to decrease the velocity by interacting with electrons until the particle is stopped. Charged ions are characterised by a definite range in the absorbing medium. This range gives the distance beyond which no further penetration of the particle is possible, the so called projected range $R_p$.

### 3.1.1 Electronic and nuclear energy loss

The energy loss in the materials can be explained in detail as the interaction of charged ions with the target nuclei and target electrons. The energy transfer between a stationary object and a moving object strongly depends on the mass and the energy of the moving object and

the direction of motion. The slowing down of ions is traditionally separated into two distinct processes: (a) electronic stopping power and (b) nuclear stopping power. The sum of these two processes is represented as total stopping power [22]. For the kinetic energy lower than 100 keV/u the nuclear energy loss dominates while electronic energy loss is more relevant at higher energies (Figure 3.1).

The elastic interaction of a moving charged projectile with the nuclei of the target material is called the nuclear stopping process. The nuclear energy loss is small at higher energies, because the fast particles have less interaction with the scattering nucleus, but becomes dominant at the end of the range when the ion lost most of its energy. At higher energies significantly a weak interaction takes place between the target nuclei and the projectile. In addition, the momentum transferred to the target nuclei is relatively small compared to the energy of the projectile ion.

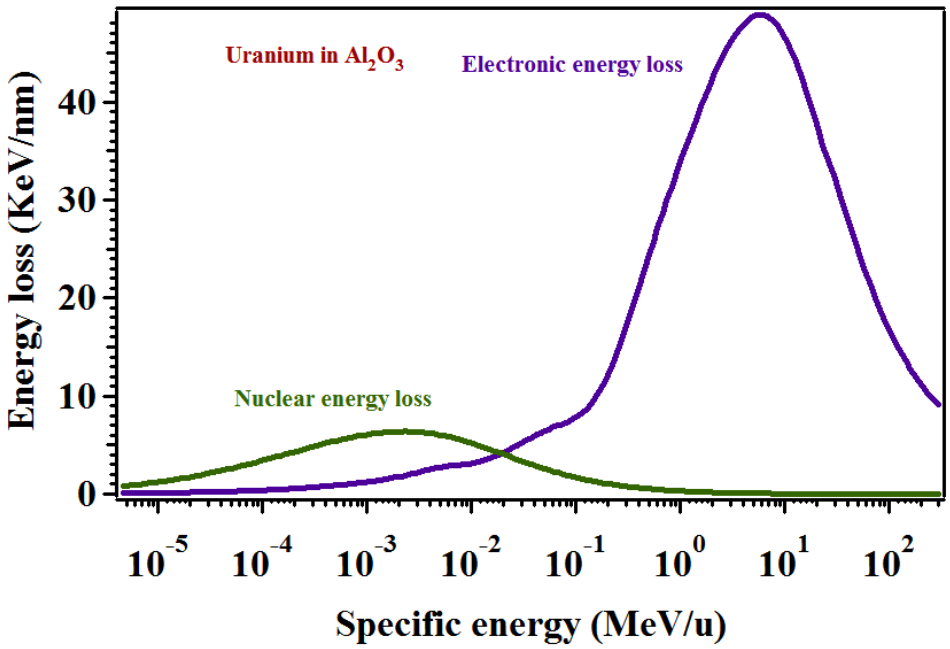


Figure 3.1. Electronic and nuclear energy loss vs. specific energy calculated for Uranium ions in $Al_2O_3$. These energy losses were calculated using the simulation program Stopping and Range of Ions in Matter (SRIM) [23].

The inelastic collision between the electrons of the target material and the moving ion is called electronic stopping. The energy loss of an ion in a medium depends mainly on the velocity and the charge state of the projectile ion. In this study the ion beams are accelerated to higher energies, E> 200 MeV/u and the electronic energy loss lies beyond the maximum region whereas the nuclear energy loss is negligible.

The energy loss in material by electronic stopping is given as the average energy loss per unit length, called stopping power or dE/dx. The value of - dE/dx along the particle track is called *specific energy loss* [16]. The semi-classical calculation for this energy loss was performed by Bethe, Bloch and some others. The specific energy loss, - dE/dx is given as

$$-\frac{dE}{dx} = 2\pi N_a r_e^2 m_e c^2 \rho \frac{Z}{A}\frac{z^2}{\beta^2}\left[\ln\left(\frac{2m_e\gamma^2\upsilon^2 W_{\max}}{I^2}\right) - 2\beta^2 - \delta - 2\frac{C}{Z}\right] \qquad (3.1)$$

with:

$2\pi N_a r_e^2 m_e c^2$ =0.1535 MeV cm$^2$/g

$r_e$ : classical electron radius =2.817 x10$^{-13}$ cm

$m_e$: electron mass

$N_a$: Avogadro's number =6.022x10$^{23}$ mol$^{-1}$

$I$: mean excitation potential

$Z$: atomic number of absorbing material

$A$: atomic weight of absorbing material

$\rho$: density of absorbing material

$z$: charge of incident particle in units of $e$

$\beta$: $\upsilon$/c of the incident particle

$\gamma$: $1/(1-\beta)^{½}$

$\delta$: density correction

$C$: shell correction

$W_{max}$: maximum energy transfer in a single collision

### 3.1.2 Bragg curve

The stopping power and the density of ionization increase while passing through a medium and reach a maximum before the energy falls to zero. The plot of specific energy loss along the penetration depth of the material is known as Bragg curve. At the end, the particles pick up the electrons and the specific energy loss decreases. This behaviour is particularly used in medical applications of radiation where high dose of radiation is delivered in cancer cells with minimum destruction in healthy tissues. The electronic energy loss and Bragg peak obtained for Uranium ions in $Al_2O_3$ samples is shown in Figure 3.2. The penetration depth of Uranium ions of kinetic energy 294 MeV/u in $Al_2O_3$ material is 4.99 mm. Since the thickness of the investigated samples was 0.8 mm thick, the Bragg peak lies outside the sample material.

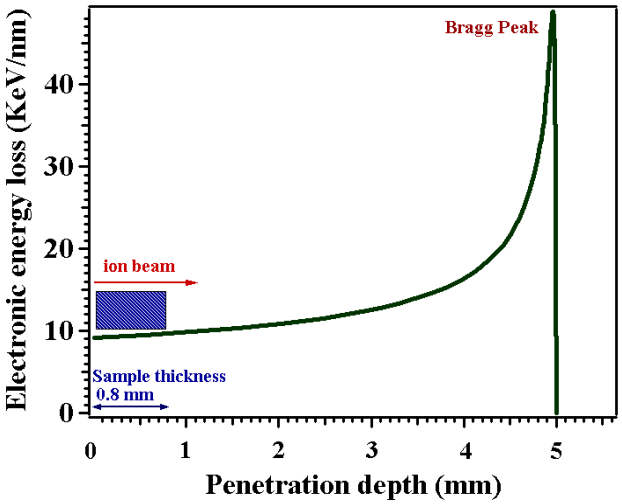


Figure 3.2: The electronic energy loss and Bragg peak obtained for Uranium ion of 300 MeV/u in $Al_2O_3$ screen calculated using SRIM [23]. The penetration range of Uranium of kinetic energy 294 MeV/u in $Al_2O_3$ is 4.99 mm.

## 3.2 Scintillation

A flash of light produced by a material when struck by particles or radiation is called scintillation and the material is called scintillator. The emitted light normally lies in the visible or ultraviolet region. The scintillation process is considered as a conversion of energy of a particle into many low energy photons. The scintillator should be transparent to the wavelength of its own emission. Weber [24] states that scintillation is an example of radio luminescence wherein the absorption of high-energy radiation or particles leads to observable light. Fünfer and Neuert in [19] defined scintillation as "the phenomenon of luminescence in transparent solids, fluids or gases, originating at the propagation of the ionizing radiation through them". The emission occuring immediately after the absorption process is called *fluorescence* while the delayed emission is called *phosphorescence* or *afterglow* [17].

The first scintillation material $CaWO_4$ was used by Röntgen in X-ray screen (1895), a month later after the discovery of X-Rays. The scintillation observed by E. Rutherford (1911) in ZnS due to α particles can be considered as the starting point of modern nuclear physics. Starting from 1930 ZnS:Ag has been used as a scintillation material in nuclear experiments, being an ideal material to detect elementary particles and to measure their parameters [25]. Scintillation effects are observed in various organic and inorganic crystals [26], fluids [27], and also in gases. The application in medical imaging and in high energy physics increases the demand on fast and high density inorganic scintillators. Many new scintillators have been introduced for different applications. Among them Ce –doped and Ce based materials appear to be promising fast scintillators. Presently, inorganic scintillators are used in fields like Positron Emission Tomography (PET), X-ray tomography, space physics and astronomy. In

high energy physics the energies of gamma-quanta and electrons/positrons in the accelerators are measured using scintillators [20].

Scintillators are mostly insulators having a wide band gap between their valence band and conduction band. Within this gap they have the luminescent centers, which play a major role in producing scintillation light. A luminescent center consists of two energy levels whose difference corresponds to the energy of the emitted photon [19].

## 3.3 Types of Scintillators

### 3.3.1 Classification of scintillators

The process of scintillation is observed in various materials like inorganic materials, plastics and noble gases. Based on the scintillation mechanism, scintillators are divided into three types, namely; self-activated scintillators with an anionic complex as radiating centers; activated scintillators which are doped with activator ions, and cross –luminescent materials. Based on composition, inorganic scintillators are classified as oxides, halides and sulphides. The combined classification also includes the compounds containing phosphorus and selenium.

### 3.3.2 Self activated materials

The self-activated scintillators are materials that contain luminescent centers within the forbidden region. The energy levels lying in the forbidden region bring these materials to produce scintillation light yield. Some examples of such scintillating materials are $CeF_3$, $Cs_2LiYCl_6$, $Cs_2NaCeCl_6$, CsI, $CaI_2$, ZnO, BGO, PWO, YAG, BeO and $HgI_2$.

### 3.3.3 Activated materials

The scintillators doped with rare earth ions are called activated scintillators. In general, these materials do not have any luminescent centers within the forbidden region. Addition of a small amount of rare earth materials like Ce, Tl, Pr, Eu, provide luminescent centers within the band gap of these materials. Several self-activated scintillators show better scintillation properties when doped with appropriate ions. In some materials the rate of the scintillation is based on the dopant ion. Doping with suitable rare earth ions transforms the materials into fast scintillators. Cerium is considered to be a favourable dopant atom for many materials because of the fast 4f- 5d transition. Both oxide and halide materials are doped with Cerium atoms. eg: $LuCl_3$:Ce, $LaBr_3$:Ce, $Y_2SiO_5$ :Ce, YAG:Ce and LuAG:Ce [24].

### 3.3.4 Cross luminescent materials

The core-valence band transition is responsible for sub nanosecond fast luminescent in cross luminescent materials. Core valence luminescence (CVL) involves a transition where an electron in the valence band fills a hole in an inner shell with emission of a photon. The core hole is expected to occur in $<1$ ps. This ultra fast luminescence is due to hot carrier intraband radiative transitions and is reported in materials like CsI, and $BaF_2$ [28].

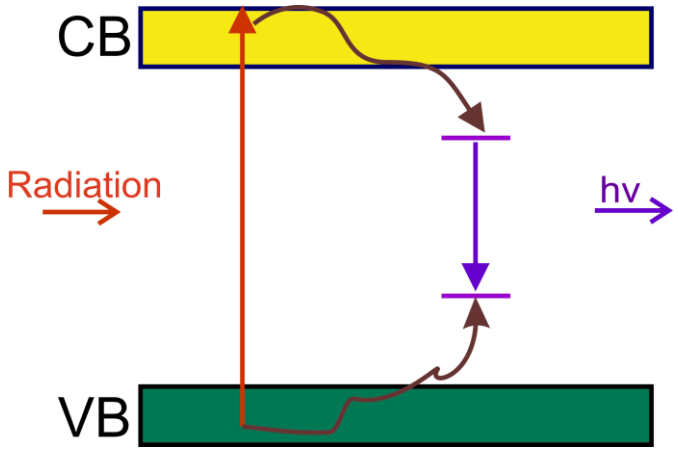


Figure 3.3: Schematic picture of scintillation mechanism in activated materials. The doping of wide band gap materials with rare earth ion creates luminescent centers in the forbidden region. VB: valence band, CB: conduction band.

## 3.4 Scintillation mechanism

### 3.4.1 Energy bands in materials

In general, the atoms are packed very closely in elements and there is a strong electrical influence between each other. The energy levels of these atoms combine to form different energy zones. In these energy zones, the electrons are allowed to occupy only certain energy states. In the available energy levels the electrons tend to occupy the lowest energy levels and no two electrons can occupy the same energy level in the same quantum state. The inner orbitals combine to form inner zones completely filled with electrons. The final zone filled with electrons is called valence band since valence electrons occupy these energy levels. The higher energy zones do not contain any electrons and the lowest high energy state is called conduction band. The energy difference between the valence band and the conduction band is called band gap which is a forbidden region where the probability of finding the electron is zero [21]. Figure 3.4 shows the formation of the energy zones in materials.

### 3.4.2 Scintillation light yield

For the scintillation process, the material has to first absorb the high energy particle to transform it into a light pulse. The scintillation light yield 'Y' is defined as the amount of light produced per unit energy deposited in the scintillator by ionization radiation as given in [29-30].

$$Y = N_{eh}.\ S.\ Q \qquad (3.2)$$

$Y$ : scintillation light yield
$N_{eh}$ : the number of electron-hole pairs.
$S$ : the probability of transfer to emitting centers

$Q$ : the luminescence quantum yield

$$N_{eh} = E_{inc} / E_{e\text{-}h} \tag{3.3}$$

$E_{inc}$ : the energy deposited by ionization radiation
$E_{e\text{-}h}$ : the energy required to create an electron-hole pair.

The energy required to create an electron-hole (e-h) pair is around 2-3 times the band gap $E_g$. When the band gap increases the number of e-h pair decreases.

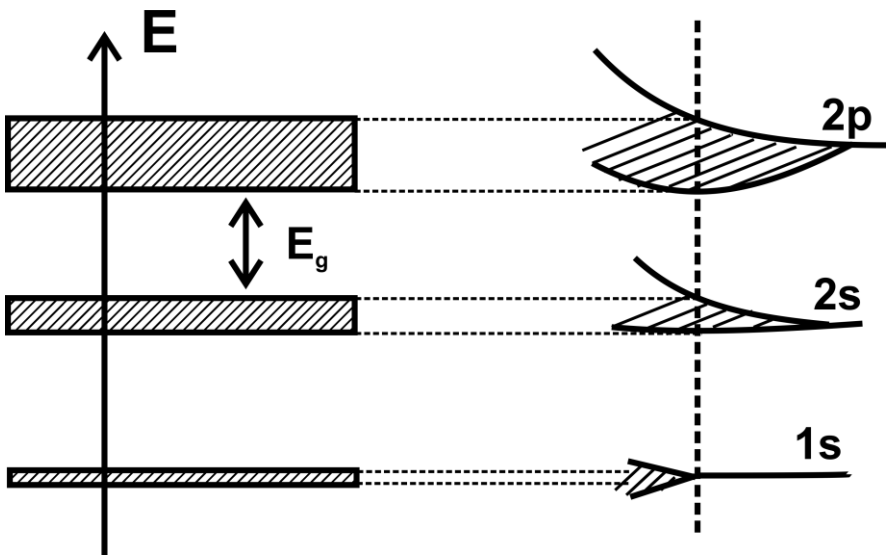


Figure 3.4: The energy zones formation in semiconductors and insulators [21].

.

### 3.4.3 Mechanism of scintillation

The process of scintillation (Figure 3.5) consists of a chain of reactions, taking place in different time periods. The four essential reactions involved in the process of scintillation are listed as follows:

1. Energy conversion: The initial energy is converted into hot electrons and holes ($10^{-18}$ to $10^{-9}$ s).
2. Thermalization: Inelastic scattering and interaction of hot electrons and holes ($10^{-16}$ - $10^{-12}$ s).
3. Migration: Formation of excitonic states and excited luminescent centers ($10^{-12}$-$10^{-8}$ s).
4. Emission: Relaxation of excited luminescent centers with scintillation light emission (>$10^{-10}$ s).

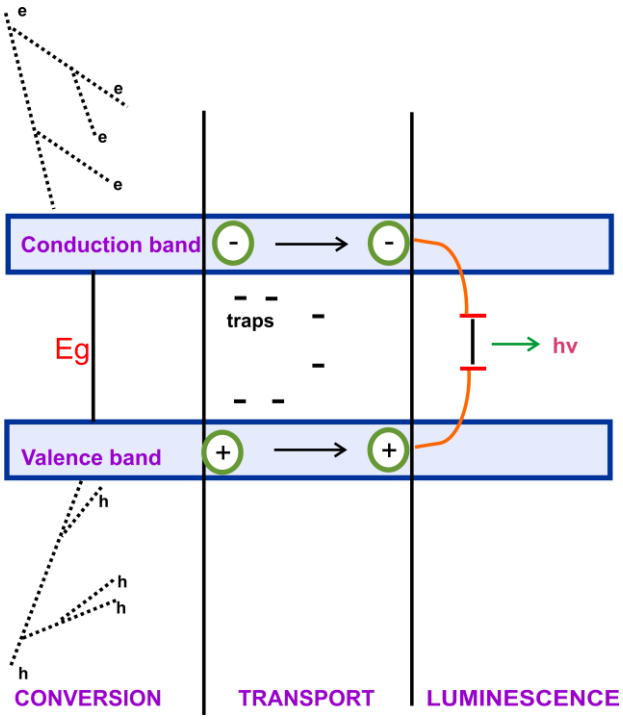


Figure 3.5: Schematic representation of scintillation mechanism.

The mechanism of excitation of the luminescent centers is greatly influenced by the medium. The influence is much more pronounced in the case of a regularly arranged crystal structure. The condition of localisation and delocalisation of excitations are strongly affected by the position of the luminescent centers energy level.

The production and recombination of electronic excitations are explained in detail using the band structure of the material by Vasil'ev [18].

A general scheme of the band diagram of an ionic crystal is shown in Figure 3.6. For a simple demonstration, one core band is shown with top energy as $E_c$ and band width as $\Delta E_c$. The valence band $E_v$ with band energy $\Delta E_v$ is separated from the conduction band by a band gap of $E_g$. There are six different stages considered to explain the mechanism of scintillation.

The first stage of the scintillation is the formation of primary excitations. When the ionizing radiation hits the target the energy of the incident particle is transferred to the scintillation material. For a very high energy of the incident radiation, deep holes are formed in the bottom of the core band and hot electrons are formed in the top of the conduction band. The electron and the holes produced are called primary excitations.

In the second stage, within a short time scale of $10^{-16}$ to $10^{-14}$ seconds numerous secondary excitations are formed in the core valence band and in the conduction band. Since the high energy electrons transfer their energy to the other electrons through inelastic scattering this process is called electron-electron relaxation. Finally, the multiplication is continued until the threshold is reached. In this stage all the electrons in the conduction band have energy smaller than $2E_g$ (electron-electron scattering threshold) and all holes occupy the valence band if there is no core band lying above the Auger process threshold.

The third stage is the thermalization of the excitations. As soon as reaching the inelastic scattering threshold, the electrons start interacting with the vibrations of the environment known as electron-phonon interaction. The result of this process is the formation of low kinetic energy electrons in the bottom of the conduction band and holes in the top of the valence band. The population of excitations remains constant during the electron-phonon interaction. The electron-electron interaction and the electron-phonon interactions are the consecutive steps in the scintillation process.

The next stage is the localisation of the excitation in which the electrons and holes interact with the traps and impurities in the crystal lattice. For example, electrons and holes can be captured in different traps or self-trapped in the crystal lattice. Excitons, self-trapped holes ($V_K$ centers), and self-trapped excitons are formed with the emission of phonons. Sometimes the localisation of excitations is accompanied by defect creation and photo stimulated desorption.

The last two steps are related to the migration of the excitation to the luminescent centers and recombination. During the migration of the excitation two types of energy transfer are possible.

a) e-h recombination
b) excitonic recombination

In e-h recombination, the luminescent centers are excited either by an electron or a hole followed by recombination. If the electron combines with the luminescent center excited by the hole then it is called electron recombination and vice versa.

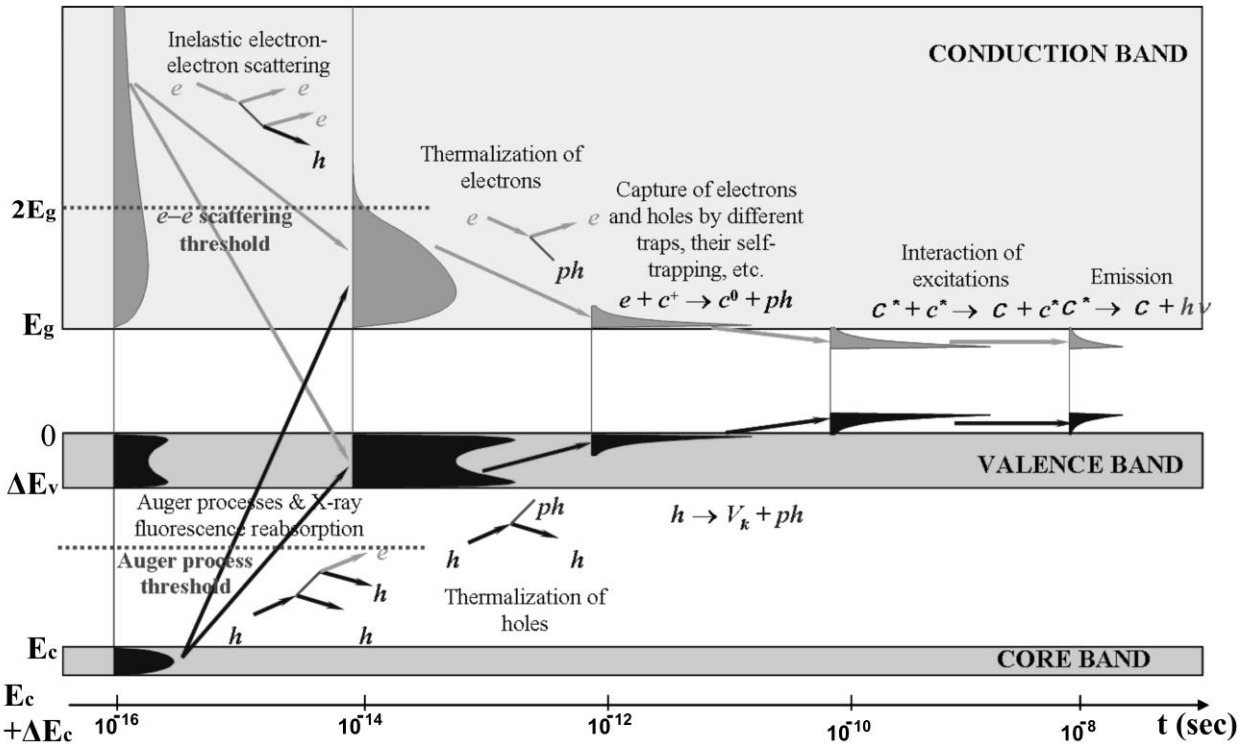


Figure 3.6: General representation of relaxation of electronic excitations [18]. The chain reactions of the process of scintillation taking place at different time scales are pictorially represented.

The process of excitonic recombination is very rare to occur in inorganic scintillators since the population of excitons is significantly less compared to e-h pair. The process of effective recombination depends on the location and distribution of the e-h pair in the system. The availability of the e-h pairs around the luminescent centers makes the recombination more efficient unless the excitation may get trapped in the defects present in the system during long migration. The scintillation materials containing rare earth ions exhibit more complex band structures. An example is the Cerium doped materials where the *4f* and *5d* levels of Cerium lay in the forbidden region. These levels play an important role in the scintillation processes and they are involved in the scheme of relaxation of electronic excitations, shown in Figure 3.6.

### 3.4.4 Harmonic oscillator model

The optical properties of a material can be explained in detail by using the configurational coordination diagram on the basis of the potential energy curves (see Figure 3.8). The curves represent the total energy of the ground and excited states as a function of configuration coordinate. It describes one of the vibrational modes in the system in which the central atom is considered to be at rest while the ligands are moving to and fro (Figure 3.7). This is called symmetrical stretching. In the plot of energy vs. inter nuclear distance, the ground (G) and excited states (E) are represented as parabolas, since vibrational modes are assumed to be harmonic, i.e. the restoring force F is proportional to the displacement $F = -k(R-R_0)$.

A force of this form corresponds to a potential energy whose dependence on R is parabolic: $E=\frac{1}{2}(R-R_0)^2$. The energy levels of the oscillators are given as $E_v = (v+\frac{1}{2})\ h\nu$, where $\nu=0, 1, 2...$ and $\nu$ is the frequency of the oscillator. In Figure 3.8, the equilibrium position of the ground and the excited states are represented as $Q_0$ and $Q_1$ respectively. Since the spatial distributions of orbitals are different in ground state and excited state, there exists a difference in wave function overlapping with neighbouring ions. This induces a shift in the equilibrium position of the excited state and separated by a distance, named as $\Delta Q$ ($\Delta Q$= distance between $Q_0$ and $Q_1$). The value of $\Delta Q$ depends on the electron-phonon interaction of the crystals. Due to $\Delta Q$ the absorption and emission takes place at different wavelengths and the energy difference is called Stokes shift (Figure 3.9) [17].

In the oscillator model (Figure 3.8), the optical absorption (A) starts from $Q_0$ and the transition ends at the edge of the excited state parabola. Then the system undergoes relaxation to an equilibrium state (B). During the process of relaxation no emission takes place since the time scale for emission is $10^{-8}$ s while the transition between the vibrational levels takes place within $10^{-13}$ s. In the next stage the system returns from the lower energy level of the excited state to the higher energy level of the ground state with a spontaneous emission (C) of a photon. Further, the system undergoes relaxation to the ground state (D) [21]. The shape of the absorption and emission bands is decided by the population of electrons in the vibrational level at thermal equilibrium.

In the process of scintillation, the occurrence of any of the following internal processes reduces the efficiency of the material. The scintillation decay time is divided into true decay time and actual decay time. The true decay time is without any non-radiative process while the actual decay time is temperature dependent and with some non-radiative process.

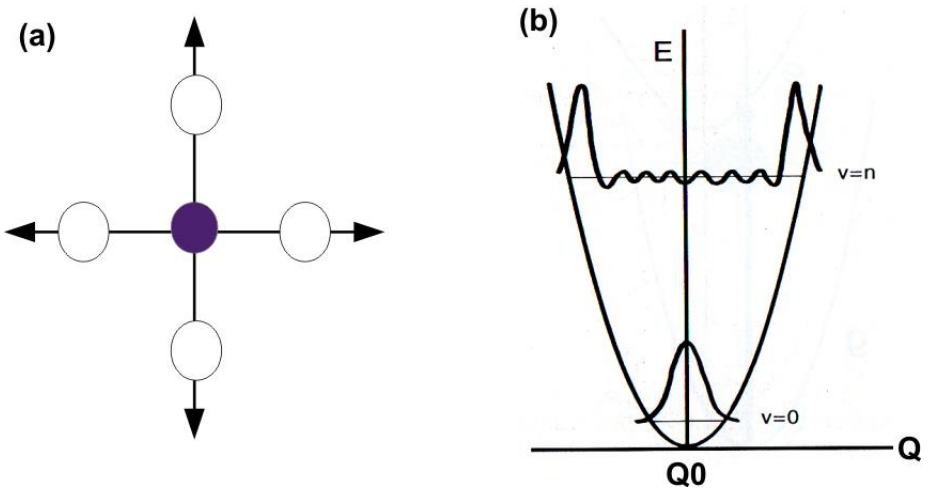


Figure 3.7: a) Symmetrical stretching vibration of a square planar complex. (b) The vibrational wave function for 'n' vibrational level [17].

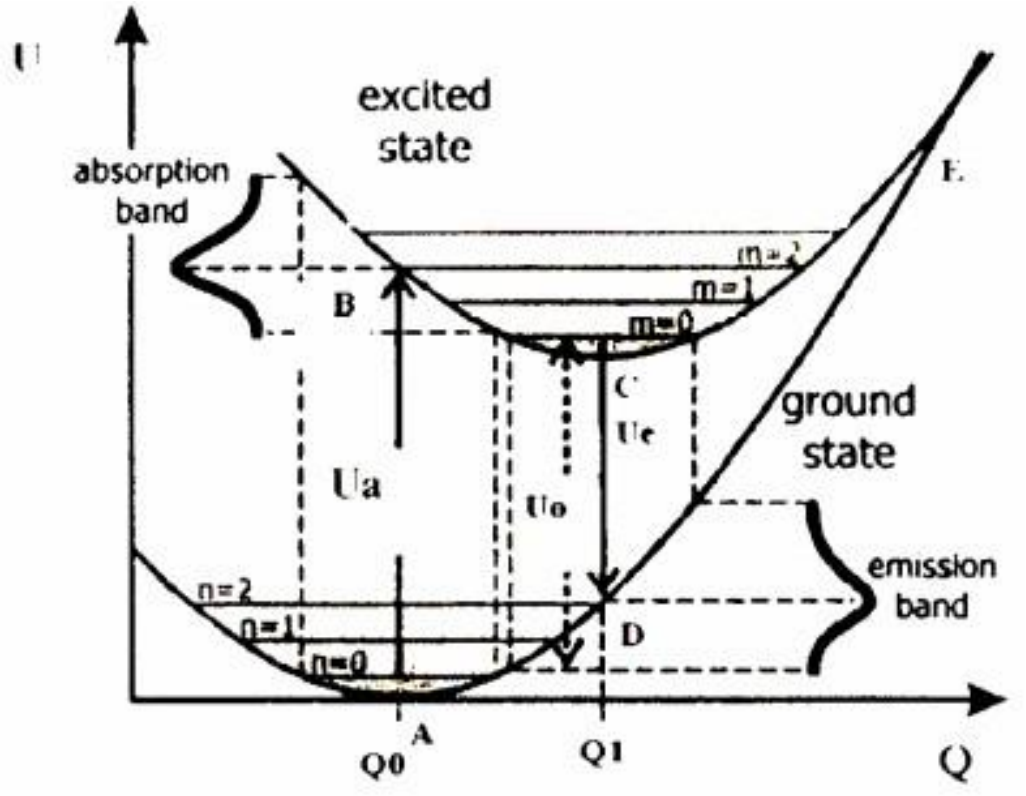


Figure 3.8: Scheme of luminescence transition in configurational coordinate diagram [21]. The *X* and *Y* axis represents the inter-nuclear distance and energy respectively.

### 3.4.5 Scintillation decay and non-radiative decays

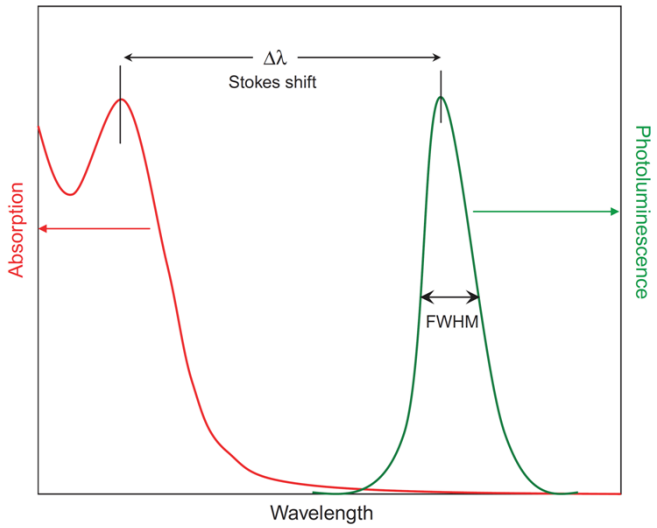


Figure 3.9: Spectral absorption and luminescence depicting Stokes shift [31].

The quantum yield of the material is near to unity when the non-radiative decay is smaller than the radiative decay. However the transfer from the excited state to the ground state is always occupied by some non-radiative decay. The interaction of host lattice with the lattice vibration induces a non-radiative transition in scintillators. This process can be explained using the configurational coordinate diagram (see Figure 3.10).

In the coordinate diagram (Figure 3.10), $Q_0$ and $Q_1$ represent equilibrium positions of the ground state and excited state. When the distance between these positions ($\Delta Q$) is large, then the excited state parabola crosses (cross point represented as *****) the ground state at lower energy level than excitation level 'B' (The position of the ***** is lower than B). In such case, the system returns to the ground state non-radiatively. The excitation energy is given as heat to the lattice. For a radiative return to the ground state, the equilibrium position $Q_1$ should lie close to $Q_0$, i.e. the offset $\Delta Q$ should be as low as possible. The parabola offset $\Delta Q$ of the system increases with increase in ionic radii of the host cation due to the expansion upon excitation, thus resulting in radiationless processes. In such materials, the quenching of luminescence takes place even at low temperatures due to the large parabola offset. In addition, the high values of vibrational frequency '$h\nu$' also raise the radiationless decay through tunnelling effect (Figure 3.11) from excited state to ground state [32].

In some systems, the non-radiative transition takes place at high temperature which makes the excited state parabola reach the crossing point. This is an example of thermal quenching of luminescence. In a system with weak phonon coupling, non-radiative transition takes place when the energy difference between the ground and excited state ($\Delta E$) $\leq 5$ times the higher vibrational frequency of the surroundings. This non-radiative process is called multi-phonon emission [33-34]. The higher values of the parabola offset ($\Delta Q$), vibrational frequency ($h\nu$) and low energy difference ($\Delta E$) shift the luminescence quenching to lower temperature resulting in radiationless transition.

## 3.4.6 Defects and trappings

The interactions between the excitations play a major role in the process of scintillation. Such interactions will decrease the population of excitation resulting in quenching of the light yield and non-proportional behaviour of the scintillator. The intrinsic defects produced during irradiation play a major role in the process of scintillation. The total light output decreases due to the color center induced absorption bands. The electrons captured by the shallow traps are released slowly by a thermal process. This result in long luminescence emission time called afterglow. The electrons captured by the deep traps are unavailable for recombination. This reduces the population of excitation. The increase in the concentration of dopants produces deep traps in some systems [19]. In case of 'Ce' doped samples, the holes get captured by the *4f* levels. These 4*f* lies very close to the valence band in oxides and halides which leads to an efficient e-h recombination process. In case of fluorides, the 4*f* of 'Ce' lays 3-4 eV above the valence band which makes the recombination inefficient.

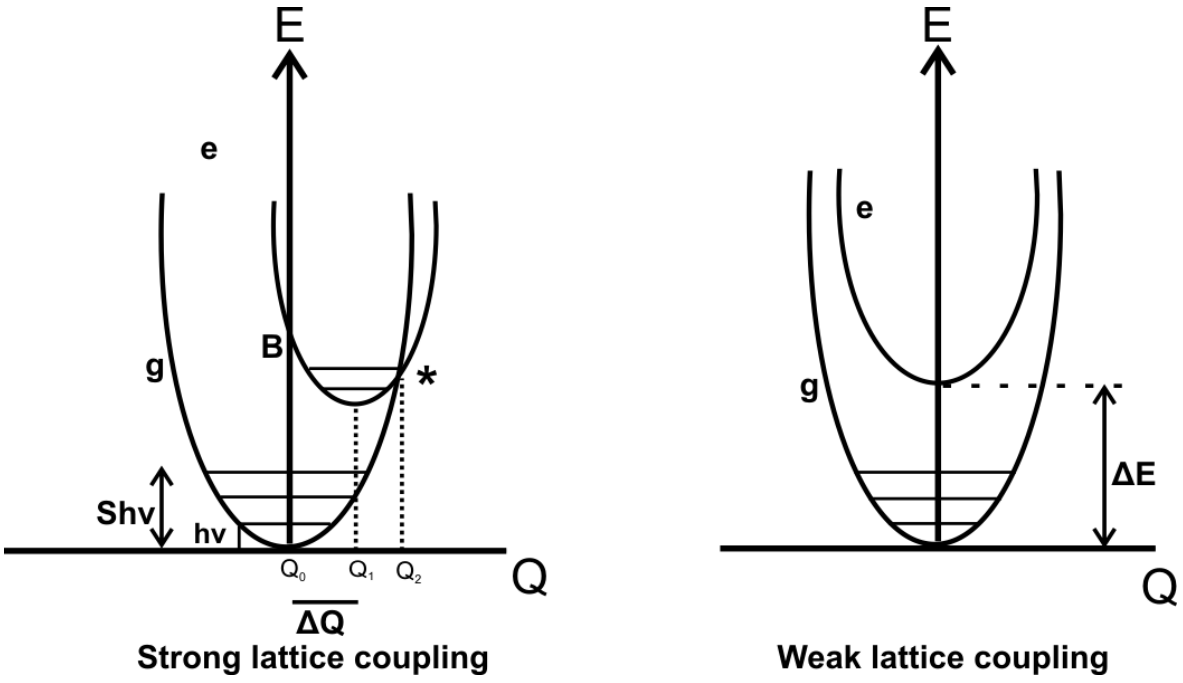


Figure 3.10: The configurational coordinate diagram of the system with strong and weak lattice coupling [17].

## 3.4.7 Presence of destructive ions

The presence of certain ions with the active luminescent centers is unfavourable for efficient scintillation. These ions capture the excitations and cause scintillation inefficiency in the system. For example, in case of 'Ce' doped samples the presence of $Ce^{3+}$ and $Ce^{4+}$ results in exchange of electrons through metal-metal charge transfer thus quenching the transfer process.

The presence of two different doping ions leads to fluorescence quenching, thereby capturing the excitations. An example is the simultaneous presence of Yb and Ce in a system where the '$Ce^{3+}$' is an efficient hole trap and $Yb^{3+}$ is an electron trap. The initial state of $Ce^{3+}$and $Yb^{3+}$ after capturing the electron and hole converts into $Ce^{4+}$ and $Yb^{2+}$ intermediate excited states and return non-radiatively [19].

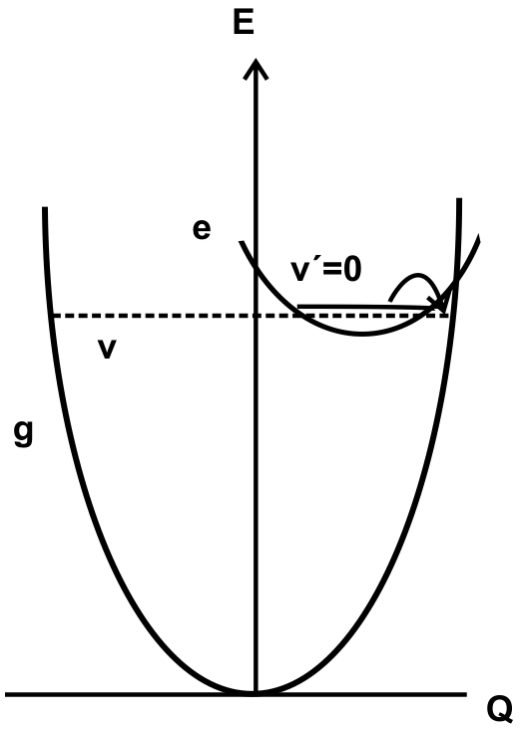


Figure 3.11: Tunnelling effect from the lowest vibrational level of the excited state to the highest vibrational level of the ground state. The effect is maximum when the excited state parabola reaches the turning point where the wave function has maximum amplitude [17].

## 3.4.8 Self-trapping of excitations

The localisation of excitations in the crystal lattice is called self-trapping. It is a very frequent and intrinsic property of inorganic scintillators. The self-trapping holes can lead to the decorrelation of electrons and holes.
For instance, in alkali halides the halogen $X^-$ becomes neutralized by interacting with the hole (h).

$$X^- + h \rightarrow X^0 \qquad (3.4)$$

The polarisation of the environment takes place due to the $X^0$ state. The system exhibits an axial relaxation resulting in sharing of the hole between two anions. This state is known as $X_2^-$ molecule or $V_k$ center and the hole is called Self Trapped Hole (STH). The time required for the formation of STH is less than the time required for the formation of free hole. Therefore in many systems, the holes are converted into STH. At low temperatures, these $V_k$ centers are static. At room temperature they migrate through the crystals by jumping between the neighbouring sites. If the time required for jumping between the sites is less than the time required for capturing an electron, the $V_k$ centers will take part in the recombination process.

The self-trapped excitation (STE) is formed by the interaction of mobile $V_K$ centers with electrons or with electron-hole pairs. Then these excited molecules emit photons by excitonic luminescence [20].

$$V_k + e \rightarrow e^0(V_k e) \rightarrow h\nu \tag{3.5}$$

### 3.4.9 Interaction between the adjacent excitations

In the relaxation process, the formation of a nanometric scale region containing several excitations separated by short distances leads to the interaction of excitation within them. This interaction between the closely spaced electronic excitations leads to a decrease in the number of excitations and the light yield. This process is called local-density induced quenching [35-36]. During the interaction between two excitations, one may disappear and the other one gains the energy and is excited to a higher energy state. In general, the probability of creation of such short distance primary excitations is very low. But the secondary excitations formed by inelastic electron-electron scattering and Auger process can be closely spaced.

## 3.5 Raman spectroscopy

The process of inelastic scattering of light was discovered by Sir C.V. Raman in 1928 [37]. He detected that the light scattered in a medium is observed not only with same frequency as the incident light but also with some additional components, whose energies are different from the incident energy. These lines are called Raman lines used for analysis. This non-destructive method provides information on chemical structures and physical forms of solids, liquids and gases with a spatial resolution of $\sim 1\ \mu$m.

### 3.5.1 Basic principle

The basics of Raman spectroscopy are explained in detail by E. Smith and G. Dent [38]. When a monochromatic light falls on a medium, the photons are absorbed or scattered. If the energy of the incident light is equal to the band gap between the ground and excited state, electronic transition takes place. This process takes place in Infra-Red spectroscopy. If there is no absorption, the incident photons produce distortions to the electron clouds and rise them to a temporary excited state known as 'virtual state'. If the photons produce distortion only to the electron cloud, then the relaxations of the system takes place with the emission of light of the incident energy. This process of elastic scattering happens in most cases, called Rayleigh scattering [39]. But in some cases, the photons (one out of every $10^6$-$10^8$) also induce the nuclear motion in which the process of energy transfer takes place. This leads to inelastic scattering and shift in the energy of the emitted photons. This process is called Raman scattering [37]. For a vibration to be Raman active, the polarizability of the molecule must change with vibrational motion. The amount of polarizability change will determine the intensity of the Raman scattering.

In Raman spectrometry, a laser of constant wavelength is used for excitation. At room temperature all the molecules are considered to be in the lower vibrational state (ground

state). The laser excites the electrons to the 'virtual state' whose energy depends on the frequency of the light source. The excitation takes place from vibrational level *m* to the virtual state. The deexcitation of electrons to higher vibrational level *n* is called Stokes scattering. The thermally excited electron in the higher energy state returning to lower energy levels is known as anti-Stokes scattering. The schematic representation of excitations is shown in Figure 3.12.

In general, the intensity of Rayleigh lines is stronger when compared to Stokes and anti-Stokes lines since most of the photons undergo elastic scattering. These lines are removed using filters in the spectrometer. The intensity of the anti-Stokes lines is less compared to Stokes lines at room temperature due to decreased population of molecules in thermally excited state. Hence, in Raman spectroscopy relatively intense Stokes lines are measured. The population of the molecules in these states can be calculated using Boltzmann equation.

$$\frac{N_n}{N_m} = \frac{g_n}{g_m} \exp\left[\frac{-(E_n - E_m)}{kT}\right] \tag{3.6}$$

Where $N_n$ = the population of molecules in excited state

$N_m$ = The population of molecules in ground state

$g$ = The degeneracy of the levels

$E_n$-$E_m$ = The energy difference between the levels

$k$ = Boltzmann's constant

$T$ =Temperature

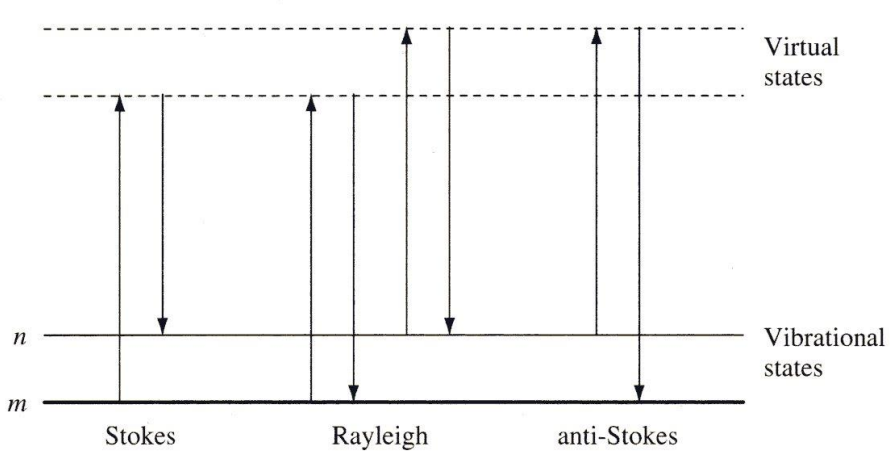


Figure 3.12: The schematic representation of excitation and relaxation of Raman scattering [38]. *m* and *n* are the lower and higher vibrational states. The relaxations of excitations from virtual state to the different ground levels produce Raman lines.

## 3.6 X-ray diffraction

A material is defined as a crystal or crystalline when the atoms are arranged in a regular pattern [40]. The group of atoms in a crystal forms unit cells and these are assembled in a certain pattern in three principal axes exhibiting certain symmetry [41]. A powerful characterization technique that helps to analyse the crystalline nature and the arrangement of atoms in the material is X-ray diffraction.

The bombardment of a material (metal target) with electrons result in the production of X-rays with wavelength in the range of 0.005- 10 nm. When a beam of X-ray is focussed on a material absorption, transmission, scattering or diffraction of X-rays takes place. X-ray diffraction is described in terms of an electro-magnetic wave scattered by the regularly ordered atoms within the material under investigation. The relationship between the wavelengths of the X-ray diffraction and the angle of the coherent interference maximum was discovered by Sir William H. Bragg and Sir W. Lawrence Bragg and is known as Bragg's Law [42-44].

$$2.d_{hkl}.\ \sin\theta_{hkl} = n\lambda \qquad (3.7)$$

with:
$\lambda$: The wavelength of the X-ray
*hkl* : Miller indices indicating the ordering of atoms on the crystallographic plane
$\theta_{hkl}$ : The scattering angle
$d_{hkl}$ : The distance between adjacent planes
n : An integer

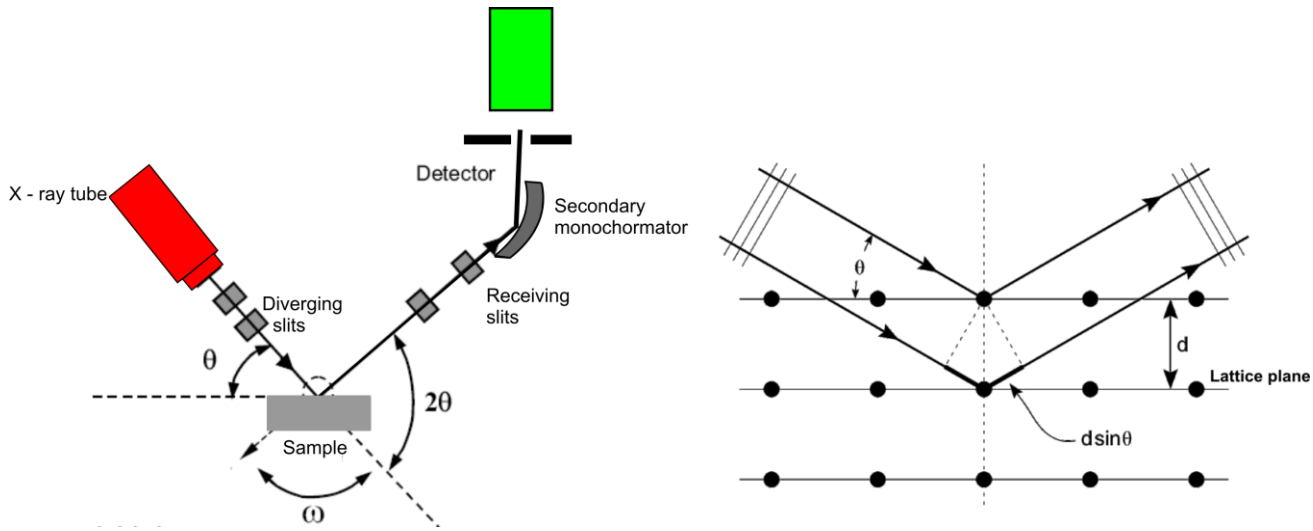


Figure 3.13: (Left) Schematic diagram of X-ray diffractometer. (Right) The principle of diffraction of X-rays from the crystal plane [44].

The Bragg's equation was derived with an assumption that the planes of atoms producing the diffraction pattern behave in such a way that the angle of incidence is equal to angle of reflection. For a known crystal system, the lattice constants of a unit cell can be derived as

$$d_{hkl} = \frac{1}{\sqrt{\left(\frac{h}{a}\right)^2 + \left(\frac{k}{b}\right)^2 + \left(\frac{l}{c}\right)^2}} \tag{3.8}$$

Where *a, b*, and *c* corresponds to the lattice constants. (E.g. for a cubic system $a=b=c$) [45]. From the FWHM of the peaks obtained, the grain size ($\tau$) of the sample can be determined by Scherrer equation [46]

$$\tau = \frac{K\lambda}{\sqrt{FWHM\, Cos\theta}} \tag{3.9}$$

where $\lambda$ is the wavelength of the X-ray, *K* is the shape factor (0.9 for cubic structures), and $\theta$ is the angle of incidence.

In this present study, Raman spectroscopy and X-ray diffraction were used to study ion beam induced modifications in structure or phase of the irradiated scintillator materials.

# 4 Experiments

## 4.1 Diagnostic devices

### 4.1.1 High Energy Beam Transport line (HEBT)

The ion beams accelerated in the heavy ion synchrotron can be delivered to 10 different experimental areas located in the high energy beam transport line (HEBT). In HEBT beam dumps are located at two experimental locations, namely HHD and HTP. The experimental study was carried out at HTP beam line which is located between HTA and HTC experimental areas. After the extraction point, the beam is guided to the target location using dipoles (bending magnets), quadrupoles (focussing magnets) and various beam diagnostics devices [3, 47-48]. At the end of each sections and in front of the destination beam diagnostics devices are installed to monitor beam current, profile and position.

Each device in the HEBT is identified by their unique name designed by using alphanumerical ASCII characters (Figure 4.1). The scintillation screen is one of the major and direct diagnostic device which helps to locate the beam. In the HEBT line, from extraction point to HTP beam dump, seven $Al_2O_3$:Cr scintillation screens were installed at various locations for beam alignment. The final screen is located at 1 m upstream of the target screens. These scintillation screens are viewed through standard video cameras in the main control room.

### 4.1.2 HTP beam line

The beam transport line HTP is used for transporting the ion beam to the beam dump. The beam line is located between the three major experimental areas namely HTA, HTB and HTC. The location of the experimental area is shown in Figure 4.1. The experimental setup was installed in front of the beam dump. A stainless steel window of 100 $\mu$m thickness is used to seal the vacuum in the beam line. The ion beam delivered in HTP beam line has a typical size around 5-8 cm in diameter.

The pressure inside the beam line is maintained in the range of $10^{-6}$ -$10^{-8}$ Pa. The maximum intensity of the beam pulse available in this area is around $10^9$ particles per pulse of Uranium ions. Higher particle intensity can be achieved with other lighter ions. The experimental area HTP is inaccessible during the beam time in adjacent caves HTA, HTB and HTC due to high radiation level. The major devices installed in HTP beam line are tabulated below (Table 4:1). These detectors were located around 1.5 meters upstream of the target screens (Figure 4.12).

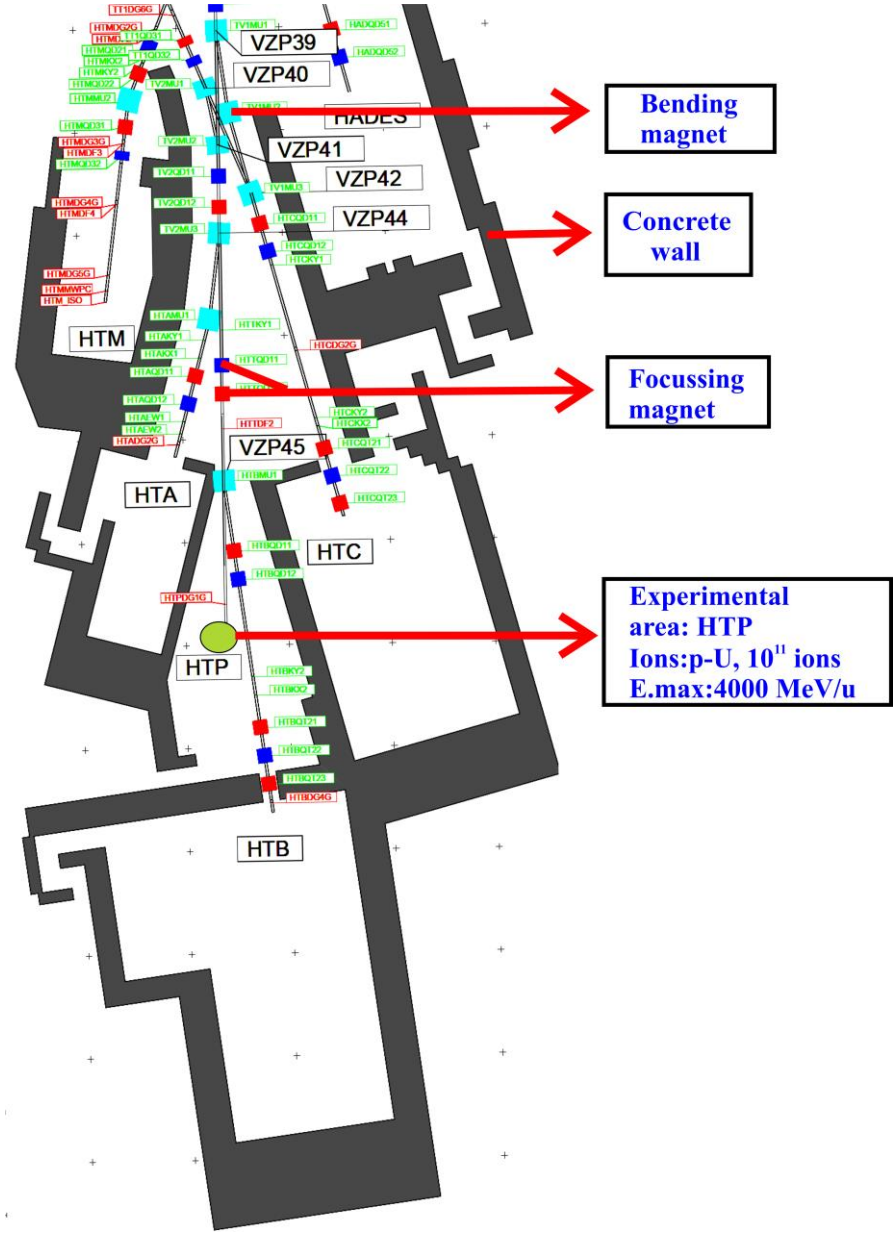


Figure 4.1: The sketch of HEBT of SIS-18. The experimental area HTP is located between cave A and Cave C. The Cave B is located down stream of HTP.

Table 4:1: The list of beam diagnostics devices installed in HTP beam line

| Measurements | Diagnostics devices | Extraction mode |
|---|---|---|
| Current | FCT | Fast |
| | IC, SEM | Slow |
| Profile | SEM grid | Fast |
| | MWPC | Slow |
| | Scintillation screens | Fast and Slow |

### 4.1.3 Beam intensity measurement

The most important parameter that should be measured in an accelerator is the total beam current. The detectors deployed for the current measurement varies according to the beam parameters. In general, a non-destructive method is preferred for the beam current measurement. In most facilities the current measurements were carried out with transformers which detect the magnetic field carried by the beam [49]. These transformers are used only for the high current measurements since they produce too much noise to measure at low intensities.

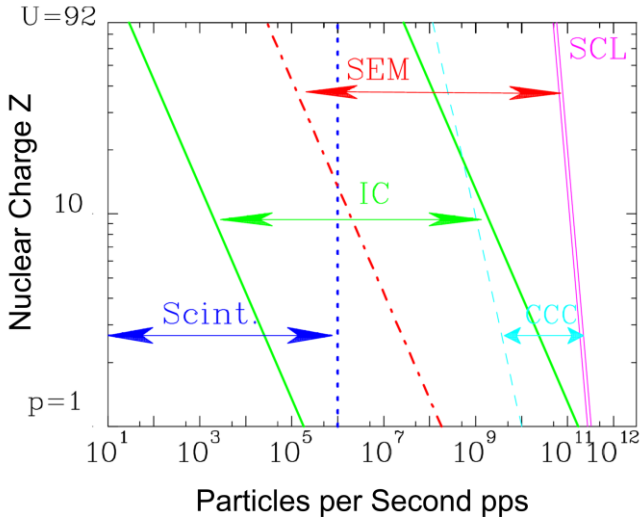


Figure 4.2: Scheme of various detector systems deployed for beam current measurement for slow extracted beam (1 s) of energy 1 GeV/u and 1 $cm^2$ cross section from SIS-18. Scint: Scintillation screen; IC: Ionization chamber; SEM: Secondary electron monitor; CCC: cryogenic current comparator and SCL: Space-charge limit of the synchrotron [3].

At GSI synchrotron, for the slow extracted beam (1 s duration), the beam current will be in the range of 100 pA which is below the resolution of a transformer [4]. In such cases, particle detectors were deployed for the current measurements. In these detectors the particles were counted directly or the particle flux was calculated against calibration. Figure 4.2 depicts the measurement range of the detectors installed for current measurements. The scintillators can be used only for low intensity beams while Ionization Chamber (IC) and Secondary Electron Monitor (SEM) detectors cover a wide range from $10^4$ to $10^9$ pps for Uranium ions [50]. At very high particle intensity, the cryogenic detectors are used to measure the current which is in the range of nA [51].

### 4.1.4 Ionization Chamber (IC)

The ionization chamber is a gas filled device used for the intensity measurement of ionizing radiation. The schematic diagram and the actual device are shown in Figure 4.3. The chamber is filled with mixture of gases (80 % Ar and 20 % $CO_2$) with thickness 5 mm in the direction of the beam at a pressure of 1 bar. Three Mylar foils of thickness 1.5 $\mu$m coated with 100 $\mu g/cm^2$ silver, separated by a distance of 2 mm act as the electrodes. Two electrodes are biased with 1 kV for the separation of charges. The gas chamber is separated from the vacuum using a 100 $\mu$m thick metal foil to reduce the energy loss of the beam.

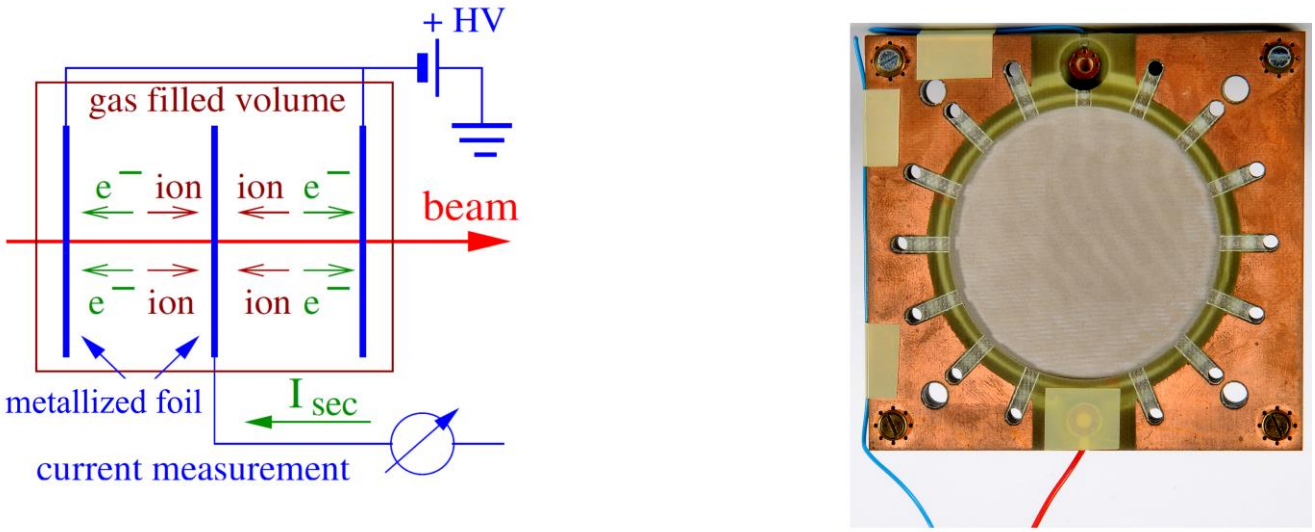


Figure 4.3: The ionization chamber, schematic diagram (left) and the actual device (right) installed in HEBT of GSI [3].

When the ion beam passes through the gas chamber, charge carrier pairs are produced and are attracted by the electrodes. This results in the formation of ionization current inside the system which is measured using a current-to-voltage converter. The energy required for producing one ion pair (W-values) [7] is known for many gasses (Ar-23.6 eV, $CO_2$- 33.0 eV ). The beam current $I_{beam}$ is calculated from the energy loss $dE/dx$, secondary current $I_{sec,}$ $W$ values and the active layer $\Delta x$.

$$I_{\sec} = \frac{1}{W} * \frac{dE}{dx} * \Delta x * I_{beam} \qquad (4.1)$$

For energies less than 1 GeV/u the calibration of the IC is performed against the scintillators [52]. The conversion factor is calculated from the measured number of particles from the scintillators and the secondary current measured from IC. The working region of the ionization chamber is between 1 pA and 1 $\mu$A. At higher beam current, saturation of the detector takes place due to the recombination of electrons with the gas ions [50].

### 4.1.5 Secondary Electron Monitor (SEM)

For the slow extracted beams where the current is in the range of 100 nA to some 0.01 pA, the measurement of particle intensity was carried out using the SEM detector. These detectors work under the basic principle of collecting the secondary electrons emitted from the metal surface. The schematic representation of SEM is shown in Figure 4.4.

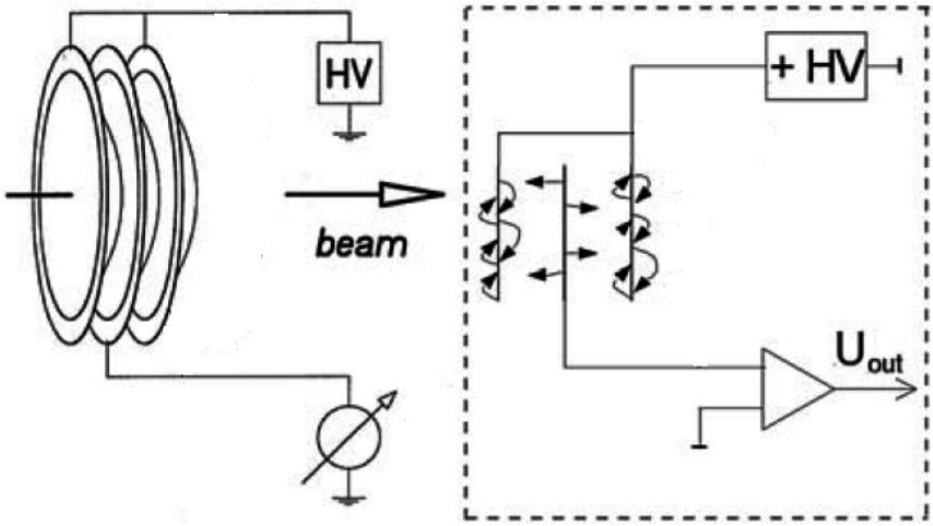


Figure 4.4: The schematic representation of the SEM detector. The left part of the diagram depicts the arrangement of the foils and the right side pictures the electrical circuit [4].

The detector consists of parallel sheets of thin metal foils separated by a distance of 5 mm. The metal foils located in the first and third positions were biased to +100 V to swear the electrons and the other was connected to the sensitive current amplifier. The surface of the metal foils are curved to increase the mechanical strength and to reduce the noise signals. Typically the metal foils are made of Aluminium due to its good mechanical properties. The detectors installed in HEBT have 3 aluminium foils which have active surface of 80×80 mm$^2$. The typical SEM detector installed in GSI -HEBT line is shown in Figure 4.5.

When the ionizing radiation passes through these foils, it interacts with the free electrons and the surface electrons of the foil. The emission of electrons from the foils takes place when $E_i > E_r + W$, where $E_i$ is the transferred energy, $W$ is the work function of the foil and $E_r$ is the energy required for an electron to escape from the foil. If the electrons are produced at a distance $\Delta x$ below the surface, then $E_r$ should be sufficient to travel the distance $\Delta x$. Experimental results show that the energy of the escaping electrons is in order of 5-10 eV and $\Delta x$ is around 10 nm. This is considered as a surface phenomenon independent of the foil bulk. With a good approximation [53] the secondary current is calculated as:

$$I_{\sec} = Y * \frac{dE}{\rho dX} * I_{beam} \tag{4.2}$$

Where '*Y*' is the conversion factor which gives the amount of secondary electrons produced per unit energy loss at the foil surface as determined by experiments. The value of *Y* is influenced by the amount of radiation which may produce surface modification. Therefore calibration of SEM detectors at suitable time intervals helps to have accurate information from the detectors [3-4].

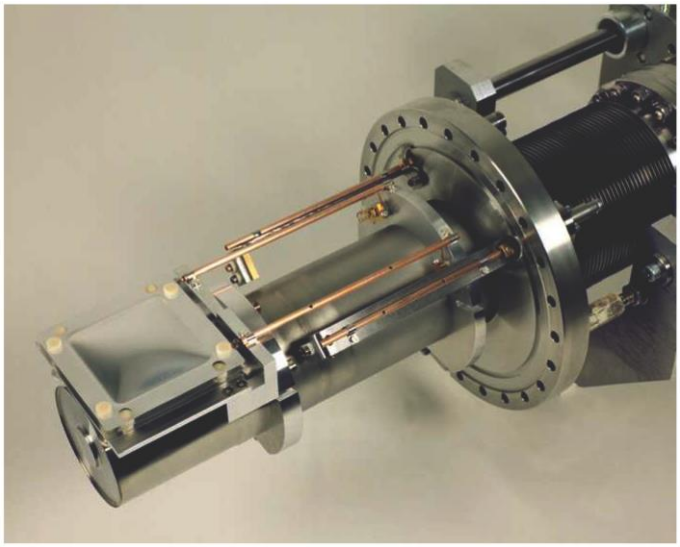

Figure 4.5: The SEM detector installed in GSI HEBT line. The system consists of three aluminium foils separated by a distance of 5 mm. The curvature of the foils gives high mechanical stability. During the measurement the foils are moved inside the beam line using a remote controlled drive [3].

### 4.1.6 Multi Wire Proportional Chamber (MWPC)

The transverse distribution of the slow extracted beam from SIS-18 was measured using a gas amplification chamber, proposed by Breskin [54]. The system consists of 3 planes of wires of diameter 25 $\mu$m, parallel to each other. The plane in the middle acts as anode while the planes in the corners act as cathodes. In the cathodes, the wires are arranged orthogonally for measuring vertical and horizontal profile whereas they are diagonally arranged in the anode. The spacing between the anode and cathode is 1 cm and the spacing between the wires is 1.5 mm. The system consists of 61 wires in each plane connected to the electronics.

To reduce the number of channels, the adjacent wires were binned and the arrangements of the wires can be given as 5×3, 5×2, 11×1, 5×2 and 5×3. The grids of the anodes are kept at high potential typically around 1 kV. The planes are sealed inside a chamber whose walls are made of 25 $\mu$m thin foils. The chamber is filled with gas mixture containing 90 % Ar and 10 % $CO_2$. The schematic diagram of a MWPC and the device used in GSI are shown in Figure 4.6 and Figure 4.7.

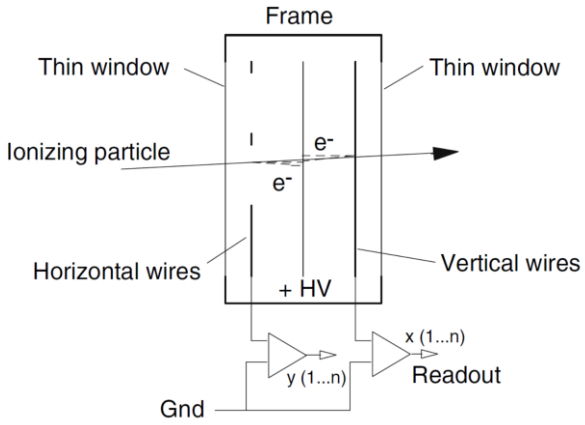


Figure 4.6: The schematic diagram of a MWPC detector. The closed chamber is filled with Argon and $CO_2$. The chamber consists of wires arranged in vertical, horizontal and orthogonal directions for producing image profiles [4].

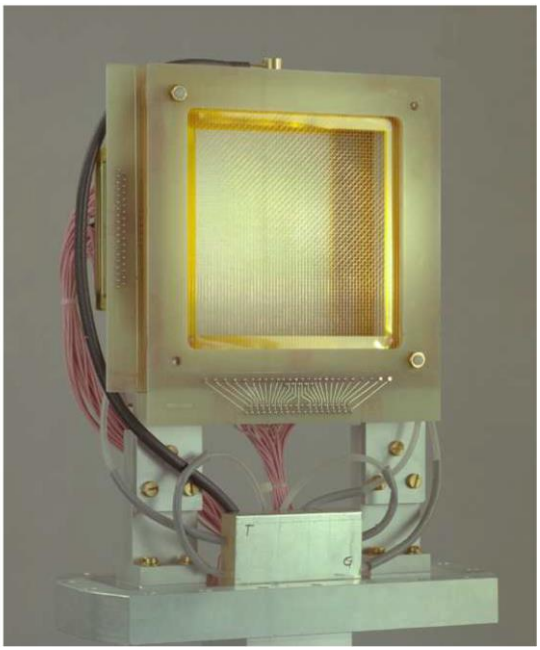

Figure 4.7: The actual MWPC device used for transverse profile measurement in HEBT line of GSI [3]. The arrangements of wires in three directions can be seen by a close look.

When the ionizing radiation passes through the gas chamber electrons are produced on the path of the radiation. These electrons are attracted by the anode at high potential leading to an avalanche, resulting in the amplification of electrons. This amplification can be increased or decreased by changing the grid potential. In the read out, the cathodes are virtually grounded using an operational amplifier which works as current to voltage converter. The spatial distribution of the particles was determined using the current read out mode stated in [55]. The device installed in HEBT line is sown in Figure 4.7.

## 4.2 Scintillation screens

### 4.2.1 Standard device

The most easy and direct way to determine the beam profile is to use scintillation screens. The scintillation light observed using a CCD sensor gives the direct 2-dimensional distribution of the beam, whereas the other measurement techniques need complex electronic signal processing. The schematic diagram and the device used in the beam line are shown in Figure 4.8. The device consists of a target holder where the scintillation screen was mounted. The CCD camera with remote controlled lens was used to monitor the screens through a glass window. During the measurement the screen was driven inside the beam and the light emitted was captured in the CCD. The profile measurement using the scintillation screen is a destructive method in the low energy region since the beam is stopped completely by the screens. For high beam energies the ions are not stopped but typically a significant energy loss occurs within the sample materials. The ion beam was acquired completely in the lateral direction by installing larger targets, typically around 5 to 10 cm in diameter.

### 4.2.2 Choice of the materials

Scintillation screens are materials used for medical imaging, electron microscope, PET, SPECT, security check and so on. There are large numbers of scintillation screens available for these applications and their behaviour was established [56-64]. The important properties that scintillation screens should possess for their application in beam diagnostics are listed.

- The maximum emission wavelength, $\lambda_{max}$ of the sample should lie in the spectral sensitive region of the CCD sensors, between 300-700 nm.
- High and linear light output over a large dynamic range of particle flux is desired. Saturation of the light output and absorption of the emitted light will lead to image deformation and wrong measurement.
- The screens should have small decay time and no afterglow for the measurement of transformation in beam profiles of consecutive pulses.
- The screens should be radiation stable and free from damage for some years.
- Good mechanical stability and availability in large size at reasonable price is also a major criterion.

### 4.2.3 Materials investigated

Based on the conditions mentioned in chapter 4.2.2 and previous experimental experience [65-67], 11 different materials were chosen for the investigation with high energetic ion beams. The materials and their properties are listed in Table 4:2.

YAG:Ce, CsI:Tl , P43 and P46 are well known scintillators. They are used in medical imaging, electron microscope, security imaging and high energy calorimeters. The total light output from the single crystal YAG:Ce is around 20 % of light output of the commonly used NaI:Tl [68] scintillation screens [17]. The major disadvantage of CsI:Tl crystal is its slightly hygroscopic nature. A long exposure time in air turns the screen milky and flexible. Therefore during the experiments the screen was installed few hours before the measurement. The

major advantage of these purpose built materials is that they have their emission in the green spectral region where the CCD has maximum sensitivity.

Table 4:2: List of scintillation screen materials investigated for profile measurements, thickness and their maximum emission lines.

| Type | Material | Thickness (mm) | λmax (nm) | Suppliers |
|---|---|---|---|---|
| **Single crystals** | CsI:Tl | 0.80 | 560 [69] | Saint-Gobain |
| | YAG:Ce ($Y_3Al_5O_{12}$:Ce) | 1.08 | 550 [70] | Crystals |
| | YAG:Ce | 0.25 | 550 [68] | Crytur Ltd |
| **Glass** | Quartz:Ce(M382) | 1.00 | 400 [71] | Heraeus Quarz |
| | Quartz (Herasil 102) | 1.00 | 400 [72] | Glas |
| **Ceramics** | $Al_2O_3$ | 0.80 | 350 [73] | BCE Special Ceramics |
| | $Al_2O_3$:Cr | 0.80 | 694 [74] | |
| | $ZrO_2$:Mg (Z507) | 1.00 | 500 [73] | |
| | $ZrO_2$:Y (Z700) | 1.00 | 440 [75] | |
| **Powder screens** | P43($Gd_2O_2S$:Tb) | 0.05 | 544 [76] | Proxitronic |
| | P46 ($Y_3Al_5O_{12}$:Ce) | 0.10 | 530 [70] | Crytur Ltd |

As mentioned in Table 4:2, two YAG:Ce samples with different thickness were investigated. The samples were obtained from different companies and have different Cerium concentrations. The powder screen P46 and single crystal YAG:Ce (0.25 mm) were supplied by Crytur Ltd. and prepared from same source material containing 0.2 % of cerium concentration. The single crystal YAG:Ce grown by Czochralski method [77] was powdered and deposited in a glass substrate with a typical grain size of about 30 $\mu$m to prepare P46 screens. The other powder screen $Gd_2O_2S$:Tb (P43) has a grain size of 15 $\mu$m, deposited on a stainless steel substrate.

Apart from these well-known scintillators, oxide ceramic materials were also investigated. Zirconium oxide is known for its toughness and heat resistance. It exists in three different crystallographic forms namely monoclinic at ambient temperature, and tetragonal and cubic at high temperature [78]. The $ZrO_2$:Y (Z700) has tetragonal structure while $ZrO_2$:Mg is a mixture of both monoclinic and tetragonal phase. $Al_2O_3$:Cr known as chromox is used in many accelerator facilities for beam alignment [9, 79]. In addition to chromox, 99.9% pure $Al_2O_3$ was also investigated to compare the effect of chromium doping in light output.

In addition to these materials, the amorphous doped and undoped quartz glass materials were also investigated. The materials investigated had the typical size of 80 mm in diameter except YAG:Ce (0.25), P46 and Quartz:Ce which had an active layer of 50 mm in diameter.

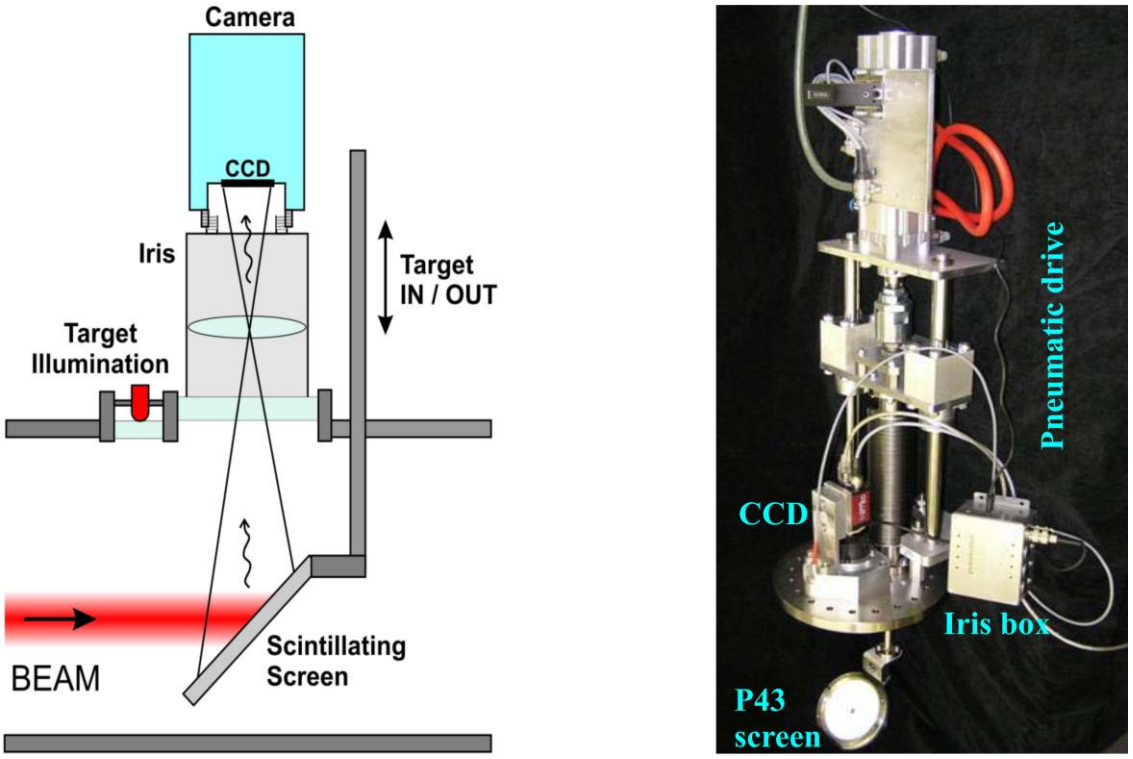


Figure 4.8: Schematic representation (left) and the corresponding scintillation screen device (right) installed in the beam line. The powder screen P43 of 70 mm diameter is mounted in the target holder and monitored through the CCD camera. The pneumatic drive moves the target inside the beam during the measurement.

### 4.2.4 Beam parameters

The heavy ion synchrotron SIS-18 is capable of accelerating all kinds of ion species from Proton to Uranium, hence the scintillation detector has to cover a very large working region. In this case, it is necessary to investigate the properties of screens with different ion species. The ion beams used for irradiation were selected in such a way that it represents different kinds of elements in the periodic table. Carbon ($_{6}$C), Neon ($_{10}$Ne), Argon ($_{18}$Ar), Tantalum ($_{73}$Ta) and Uranium ($_{92}$U) ion beams are used for the investigation. Carbon and Neon are the representatives of light weight ions. Argon represents medium weight ions while Tantalum and Uranium represent heavy ions. For a systematic investigation, all ions were accelerated to an energy of 300 MeV/u which corresponds to 65 % of the speed of light. The ion beam accelerated in the SIS-18 can be extracted in two different modes: fast extraction which lasts up to some $\mu$s pulse duration and slow extraction up to some seconds. In this study, the pulses were extracted within 300 ms with a maximum repetition rate of 0.33 Hz.

To investigate the power threshold of the screens, the particle intensities were varied in the range from $10^4$ to $10^9$ particles per pulse (ppp). Each screen was irradiated with 40 beam pulses for each intensity region and the scintillation light was recorded. The calculated light output was plotted as function of particle intensity to examine the behaviour of the screen at varying intensities. In daily operation, the radiation dose received by the screens used for beam alignment is comparatively higher than the dose deposited during the linearity measurement of this study.

In order to understand the response of the screens at heavy radiation environment, the radiation hardness of the scintillators was investigated by irradiating with heavy ion Uranium. The Uranium ion beam was accelerated to 200 and 300 MeV/u of kinetic energy and applied to selected scintillators for stability measurements. The low energy ion beam was applied in order to deposit more energy in the scintillation screens. The targets were irradiated with 400 beam pulses at 200 MeV/u and more than 1000 pulses at 300 MeV/u with particle intensity of $6\times10^8$ ppp in two different beam times.

### 4.2.5 Energy loss in the beam line

The ion beam hitting the scintillation targets is in highly ionized state since it loses almost all the electrons while passing through the stainless steel and aluminium foils in the beam line. Two 50 $\mu$m thick stainless steel vacuum windows are used to separate the beam line maintained at different pressures levels. A 150 $\mu$m aluminium foil is the component of SEM; it produces the secondary electrons for intensity measurements. 100 $\mu$m stainless steel windows are used to separate the vacuum and gas chamber of IC which is in atmospheric pressure. These metal foils introduce a stripping effect on the ion beam and also reduce the kinetic energy of the ions beam. In addition, the beam passes through 30 cm of air after leaving the beam line, where it loses some more kinetic energy.

The list of the metal foils, their thickness and the energy loss in these foils for 300 MeV/u of Uranium is tabulated in Table 4:3. The final energy of the ion beam reaching the targets was $\sim$269 MeV/u which corresponds to total energy of 64 GeV. The energy loss calculations for other ion beams were performed in a similar manner.

Table 4:3: The energy loss in the vacuum windows and foils located in the beam line calculated using SRIM program [23] for 300 MeV/u Uranium ions.

| **Foils** | **Thickness ($\mu$m)** | **Energy in (GeV)** | **Energy out (GeV)** |
|---|---|---|---|
| Stainless steel | 50 | 71.4 | 70.6 |
| Aluminium | 150 | 70.6 | 69.7 |
| Stainless steel | 100 | 69.7 | 68.1 |
| Argon gas | 100000 | 68.1 | 67.7 |
| Stainless steel | 100 | 67.7 | 66.0 |
| Stainless steel | 50 | 66.0 | 65.1 |
| Air | 300000 | 65.1 | 64 |

## 4.3 Experimental setup

### 4.3.1 Hardware

A dedicated experimental setup was installed in HTP beam line for the systematic investigation. The schematic diagram of the experimental set up is shown in Figure 4.9. The scintillation screens were installed in front of the beam dump in air. The scintillation light produced was captured using the CCD camera mounted above the beam line at 45° to the beam axis.

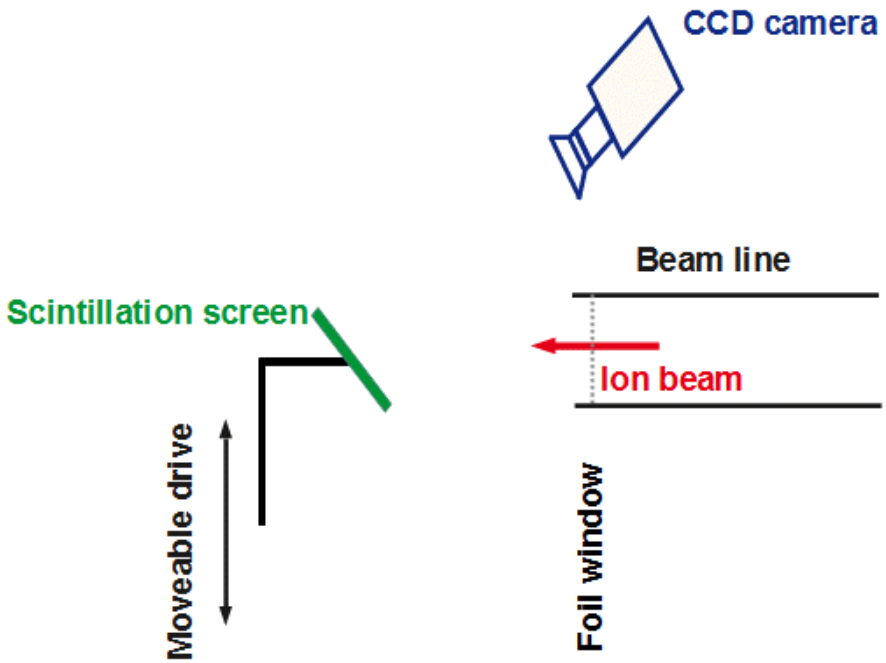


Figure 4.9 : Schematic representation of the experimental setup installed in the beam line. The linear drive helps to move the target ladder. The position of each sample was pre-calibrated.

Figure 4.10: The aluminium target holder with different scintillation screens. The targets are 80 mm in diameter; the last position (10) is occupied by a resolution target used for calibration.

Table 4:4: The list of ion beams and their parameters in chronological order.

| Ion species | Initial kinetic energy (MeV/u) | Final energy on targets (MeV/u) | Beam intensity (PPP) | Date of Experiment |
|---|---|---|---|---|
| U | 300 | 269 | $10^4$ to $10^9$ | 01.11.2010 |
| U | 300 | 269 | $10^4$ to $10^9$ | 22.11.2010 |
| Ar | 300 | 292 | $4\times10^4$ to$10^9$ | 09.04.2011 |
| C | 300 | 296 | $10^6$ to $10^9$ | 10.04.2011 |
| Ne | 300 | 295 | $10^6$ to $10^9$ | 23.05.2011 |
| Ta | 300 | 275 | $10^4$ to $10^9$ | 05.07.2011 |
| U | 200 | 162 | $4\times10^8$ | 29.10.2011 |
| U | 300 | 269 | $6\times10^8$ | 30.03.2012 |
| U | 300 | 269 | $4\times10^8$ | 01.04.2012 |

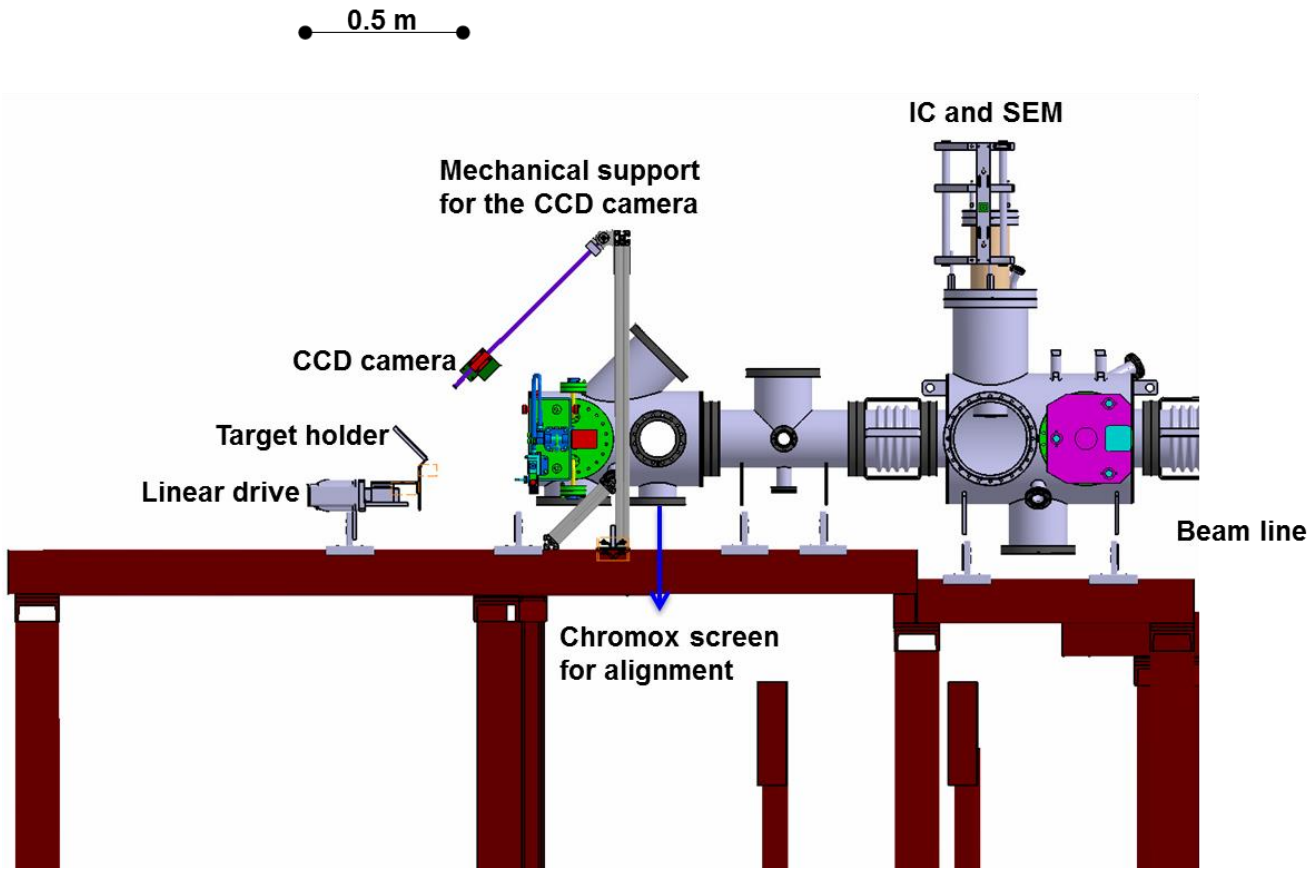


Figure 4.11: Auto CAD picture of the HTP beam line. The beam intensity detectors IC and SEM are located around 1.5 m upstream of the targets and the chromox screen for beam alignment before the end of the beam line.

The selected scintillators were fixed on an aluminium target holder of a length of 110 cm. The target holder (Figure 4.10) with 9 scintillation screens was mounted on a remote controlled linear drive. The ends of the linear drive were fixed with two end switches to prevent overrun. The position of each target was calibrated to the center of the beam line and the camera focus. During beam time the targets were moved to the calibrated positions and the irradiation was carried out in air. The ion beam leaves the beam line by passing through a stainless steel vacuum window of 100 $\mu$m thickness and travels 30 cm in air before hitting the target.

During irradiation, the ion beam was not completely stopped in the material because of the high stopping range of the energetic ion beam. Since the maximum thickness of the target was only 1 mm, a part of the energy was deposited in the materials. The energy loss in materials, foil windows, current measuring detectors in the beam line and air were calculated using the *Stopping and Range of Ions in Matter* (SRIM) program [23]. The high energetic ion beam travels through the target depositing partial energy and enters the beam dump. The 2D view and the original picture of HTP line with detectors are shown in Figure 4.11 and Figure 4.12. The detailed view of the experimental setup is shown in Figure 4.13.

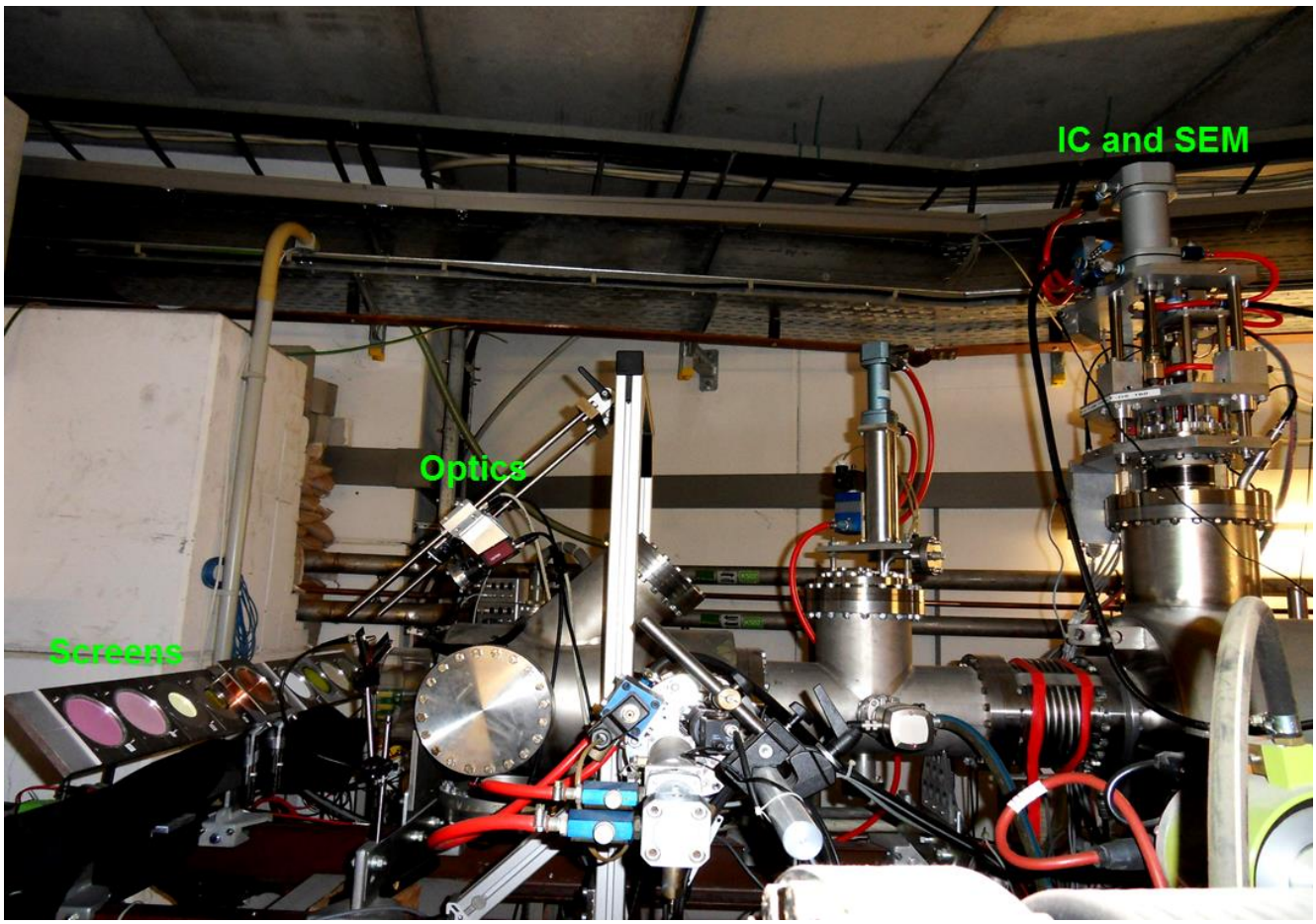


Figure 4.12: The HTP beam line with beam diagnostics detectors and experimental setup installed for the present study.

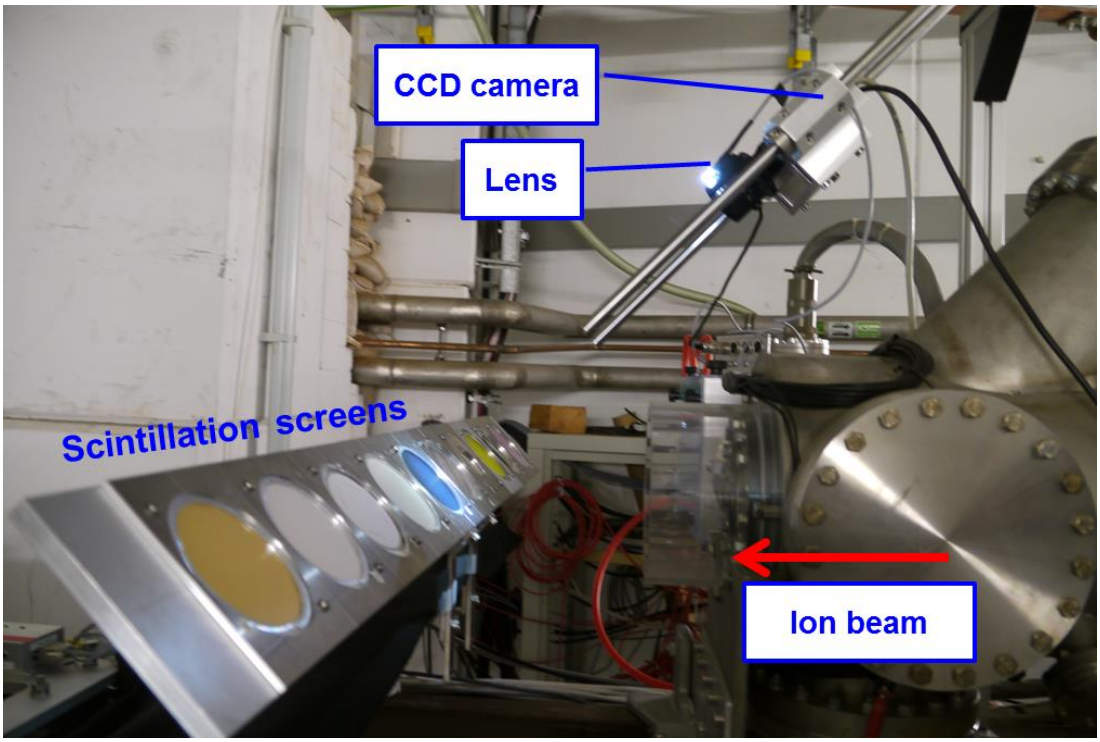


Figure 4.13: The experimental setup used for ion beam profile measurements. The moveable target ladder is equipped with nine scintillation screens (pink: $Al_2O_3$:Cr, green: YAG:Ce) and is tilted by 45° with respect to the beam. The CCD camera is placed perpendicular to the screens.

### 4.3.2 Camera and optics

The scintillation light produced by the target was captured using a standard Charge –Coupled Device (CCD) camera AVT Marlin F033B (8 bit ADC) with a monochrome chip ICX414 of VGA resolution [80]. A Pentax lens C1614ER with 16 mm focal length, equipped with remote controlled iris was used to compensate the different light output from distinct materials and to acquire a large dynamic range of particle number. The voltage corresponding to different iris openings was calculated using the 'hysteresis' curve which was measured before the experiments shown in Figure 4.15. These measured voltages were sent to the Pentax lens using an iris box. The distance between the CCD sensor and the target was 42 cm. The optical reproduction scale achieved with this setup was 4.0 pixels/mm (Figure 4.14). The spectral sensitivity of the CCD sensor is shown in Figure 4.15. In order to record the emitted light color, a color CCD camera (AVT Marlin F033C) was installed in addition to the existing set up and the measurement was carried using a Uranium beam.

Test bench experiments show that the vignetting effect of the optics has no significant influence on the measurements since the size of the beam spot was typically around 40 mm in diameter. The beam was aligned always to the center of the camera focus. In addition, the influence of different iris openings on the image width was analysed. An artificial beam spot was created using a light emitting foil and pictured with different iris openings and the spot width was calculated (Figure 4.16). The maximum difference obtained from the spot width calculation was around 2.3 % (0.17 mm). This value was negligible when compared to the recorded image width.

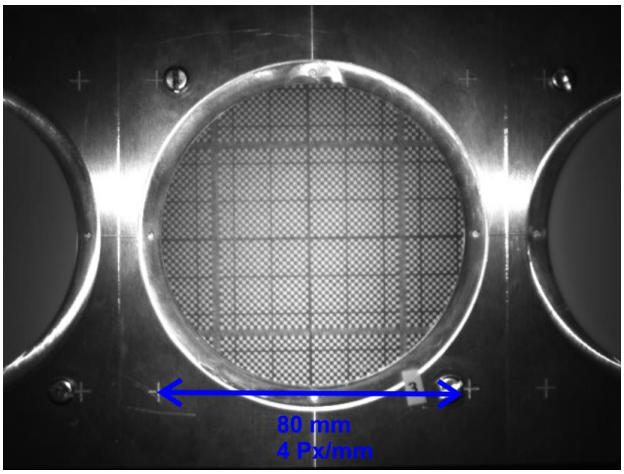


Figure 4.14: The resolution target used for calibration of the camera and optics.

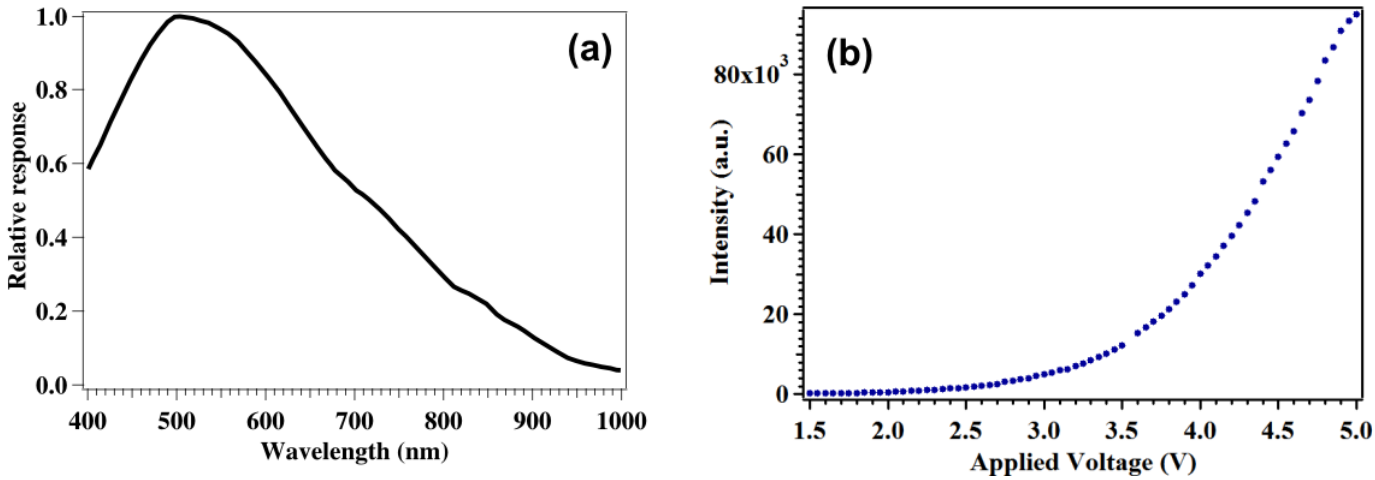


Figure 4.15: (a) The spectral sensitivity of the CCD sensor [80]. (b) The hysteresis curve measured for the Pentax lens system C1614ER

### 4.3.3 Camera trigger

The CCD camera used for the experiment can be operated in two modes, namely free run which is a standard video mode and triggered mode where the pictures are taken at particular timing signals sent to the camera. In this study, the pictures were recorded in the trigger mode. During the measurement two images were recorded for each beam pulse. First the background image (image of the scintillation screen recorded before irradiating with beam pulse) was captured few 100 ms before the beam delivery and then the beam image was taken.

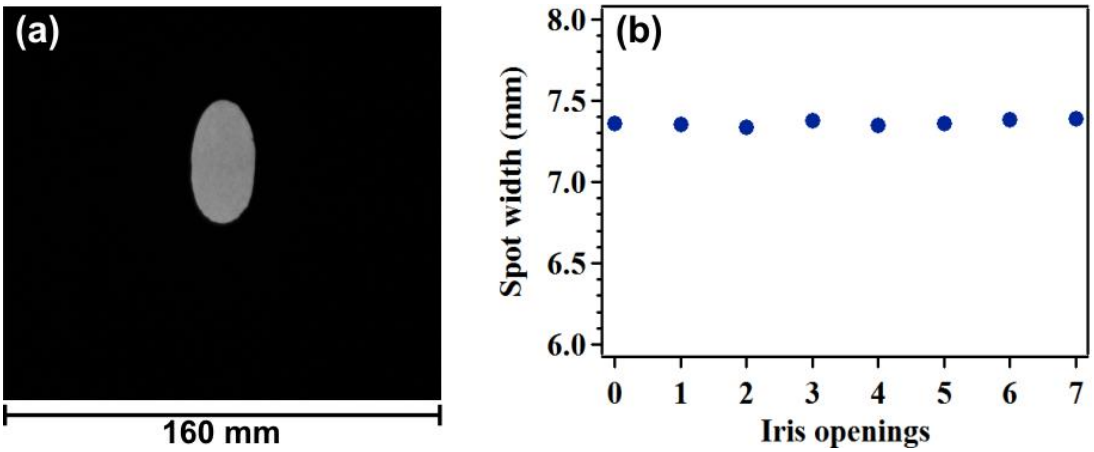


Figure 4.16: (a) Beam spot generated for measuring the vignetting and the effect of different iris openings on the recorded width. (b) Spot width 'σ' recorded for different iris openings. The value 0 and 7 corresponds to maximum and minimum iris openings respectively.

For the camera trigger, two different signals were chosen from SIS-18 timings: pulse injection in the synchrotron for background picture and pulse extraction for beam delivery. These two 5 V TTL signals were converted into NIM signals and fed to the 'OR' gate for summation of the signal. The signal from the 'OR' gate was reconverted into TTL signal and sent to trigger the camera. The trigger signals, the integration enabled signal from the camera and the beam current in the SIS were monitored using an oscilloscope (Figure 4.17).

Each division in the oscilloscope scales 200 ms. The channel 1 shows the two trigger signals summed using the 'OR' gate. The channels 2 and 3 correspond to the trigger and integration enabled signal from the camera. The two integration enabled signals correspond to background picture and beam delivery. From the synchrotron the beam was extracted within 300 ms. The integration time of the camera was fixed as 400 ms to cover the whole beam delivered. The integration time of the background picture was also fixed as 400 ms to have the same optical condition.

The channel 4 represents the beam current in SIS which ramps up during acceleration and decreases when the beam was extracted. From the transformer signal the exact beam delivery time was obtained. These signals were monitored for every beam pulse. All the electronics required for the measurement were assembled in the measurement station located 60 m above the beam line. The camera was connected to the computer in the measurement station via 60 m long FireWire interface. The trigger signal to the camera and the integration enabled signal transfer were performed through BNC cables.

### 4.3.4 Data acquisition

The data transfer process from the camera was performed using a FireWire interface (IEEE 1394a) to the acquisition system called BeamView [81]. The screen shot of the program BeamView is shown in Figure 4.19. This system helped to view and save images in both free run and triggered mode with precise triggering on GSI machine events. The integration time, iris and the gain settings of the camera were also controlled using this system.

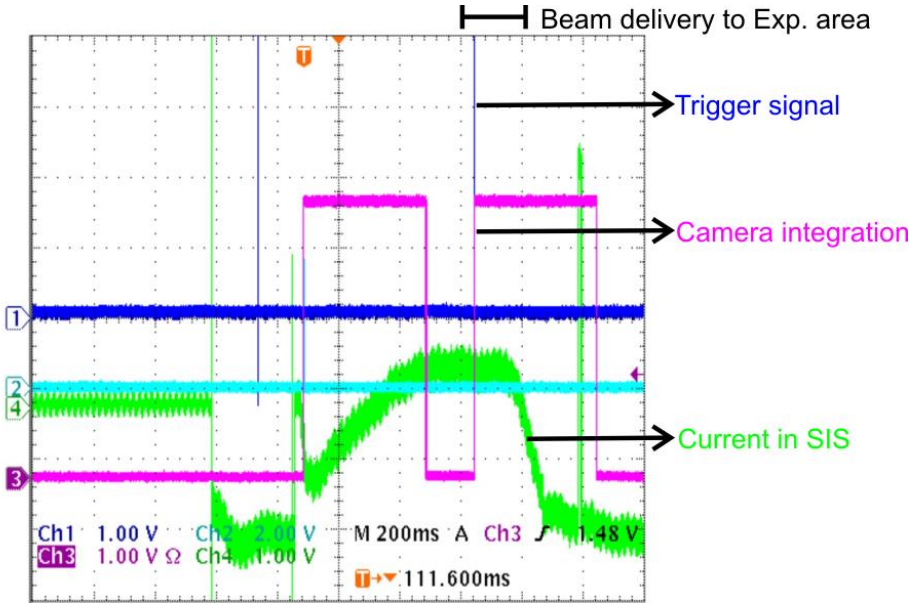


Figure 4.17: Screen shot of oscilloscope taken during experiments. Each division scales 200 ms. The integration time for the background picture and the beam image was around 400 ms.

It also helped to perform online analysis like projections, histogram and false color mode to examine the CCD saturation. Other features like rotation, mirror image and grid line were used for the calibration of the targets before experiments.

The components of the BeamView window are explained as follows:

a) The projection of current beam image in horizontal and vertical direction.
b) The controls for iris opening, LED, grid, image saving, false color mode and file extension.
c) The log window displays the experimental logs such as integration time, gain setting, image rotation, frame count and frame rate.
d) The beam image captures in the CCD sensor.
e) The histogram displays light intensity for each beam pulse.
f) Expert mode tab under which the gain settings, integration time, time base and other camera attributes are available.

The images were stored as jpg files. A false color mode of the beam image was enabled to identify the saturation of the CCD sensor.

During the beam time, the data acquisition was started with the minimum detectable signal for a completely open iris at maximum camera gain. The iris opening and the camera gain were reduced as the light output increased at high particle intensities and the measurement was stopped when the minimum iris opening was reached. The program BeamView supports 8 levels of iris opening. In the offline experiments a constant light emitting foil was used for iris and gain normalisation.

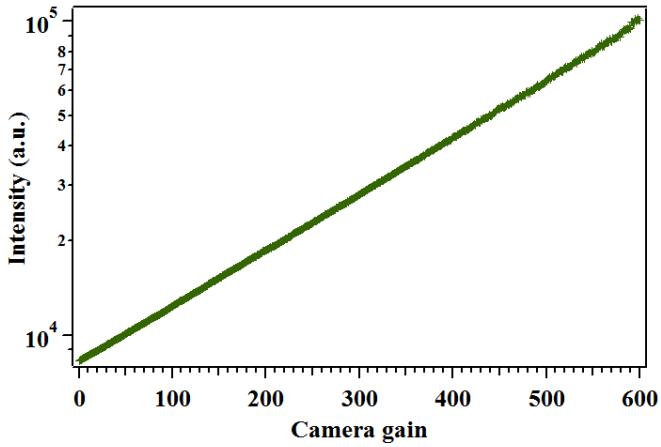


Figure 4.18: Gain curve obtained for camera 1. The light output from the foil increased linearly with the camera.

The screen in the target ladder was replaced with the light emitting foil. The light from the foil was pictured at different iris opening and constant camera gain. The iris normalisation factor was calculated from the total light output. To calculate the gain normalisation factor, the measurement was performed at different camera gain with constant iris opening (completely opened iris). In both measurements, the integration time was adjusted to avoid the saturation of the CCD sensor. The measured light output from the foil shows a linear increase with increased camera gain, as shown in Figure 4.18.

The read out from the IC and SEM detectors was carried out using the system called ABLASS [82]. This system was assembled to count particle numbers and signal from the detectors installed in HEBT for the slow extracted beam. From the read out the spill structure (Figure 4.20) and the trend values of IC and SEM detectors were obtained from which the particle intensity was calculated.

### 4.3.5 Extended measurement

In case of sensitive materials, during the irradiation with heavy ions (Ta and U) the measurements at higher particle intensities were restricted due to the saturation of the CCD sensors. In order to measure the upper threshold of the scintillators a second camera (AVT Marlin) equipped with a grey filter ITOS NG4 [83] with~5 % transmission in the yellow–green region (Figure 4.21) was installed along with the existing camera. The second camera was fixed below the first camera in the same holder as shown in Figure 4.22. Thus the measurement at higher particle intensities was carried out with camera 2 equipped with the grey filter. The resolution obtained for the second camera was 3.9 px /mm. With the second camera, the measurements were extended for some more orders of magnitude particle intensity.

The grey filter which was used for the extended measurement has different transmission rates between 400 and 700 nm. Since the emission lines of the investigated scintillation screens lay in this region it is essential to normalise the results obtained from camera 2 to camera 1 for each investigated screen. During the investigation, the measurement at low particle intensity was carried out with camera 1 and high intensity was done with camera 2. In the medium intensity range, the images were captured with both cameras. Thus, for the same beam pulse two images were recorded, with and without grey filter. The camera normalisation factor was calculated by normalising the intensity calculated from these two beam images. This method was followed for every sample to calculate the normalising factor. Even though the samples have a broad emission line and the grey filter has different transmissions, this method helped to make a precise calculation of the conversion factor.

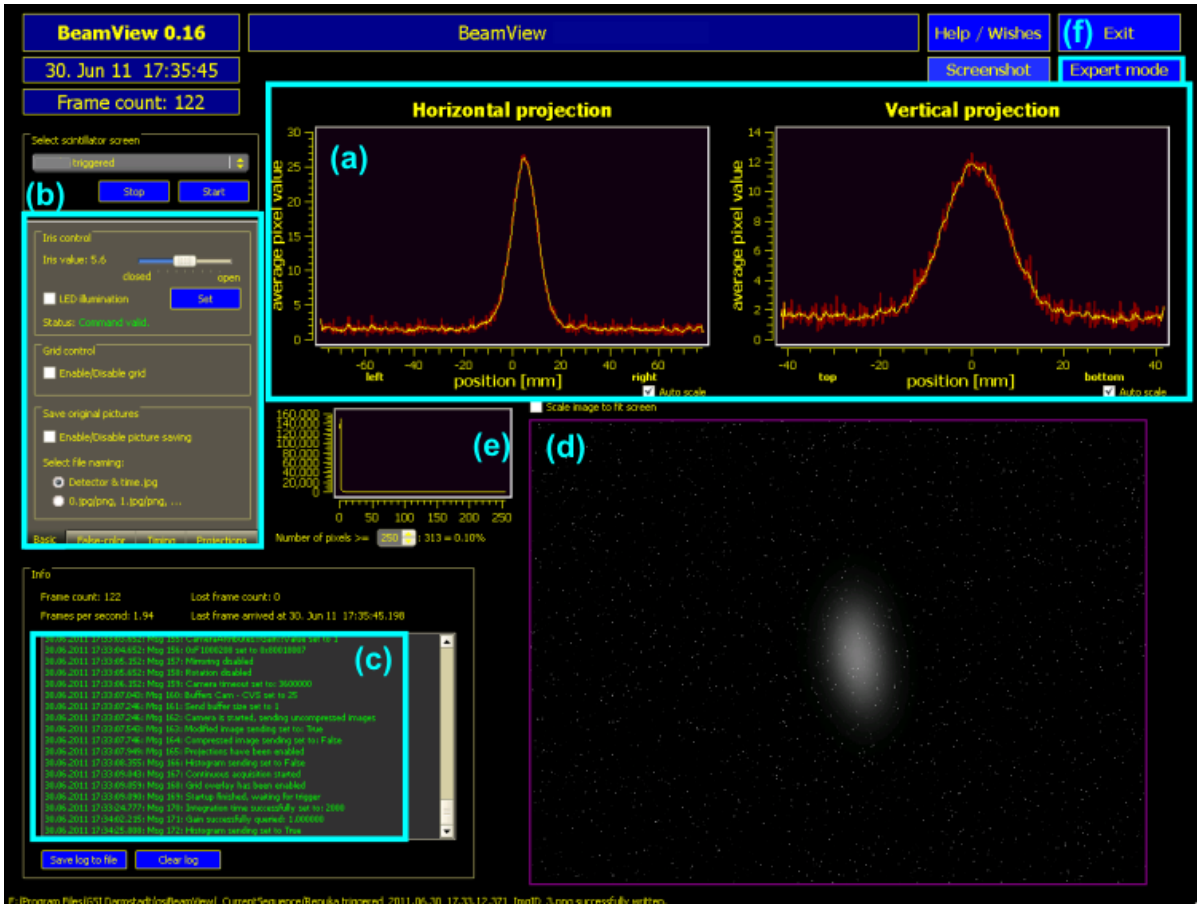


Figure 4.19: Screen shot of the data acquisition system BeamView taken during beam time.

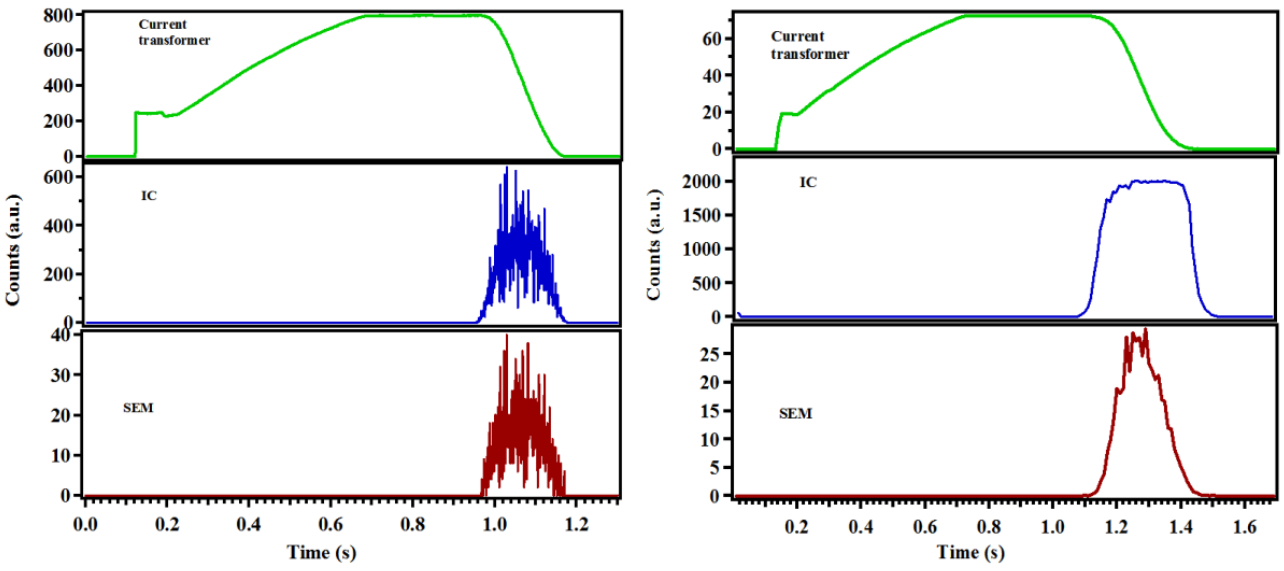


Figure 4.20: Spill structure obtained from ABLASS [82] for Ta (left) and U (right) at 300 MeV/u. At high intensity of Uranium, the IC gets saturated and the measurement is continued with SEM detector

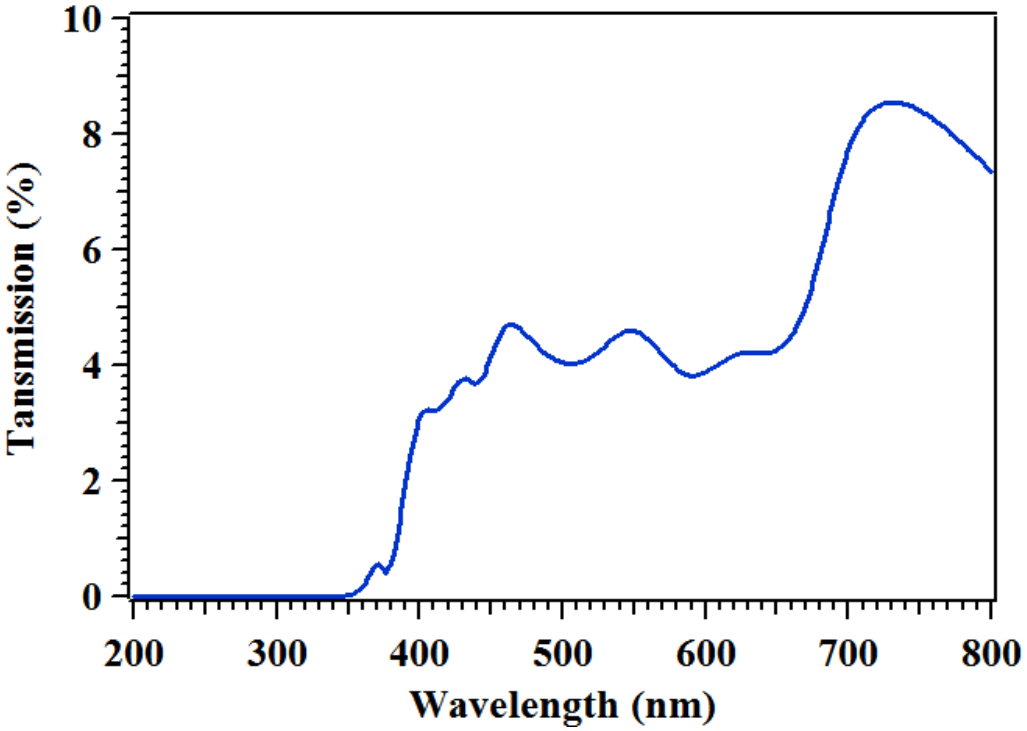


Figure 4.21: Transmission gradient measured for ITOS NG4 grey filter.

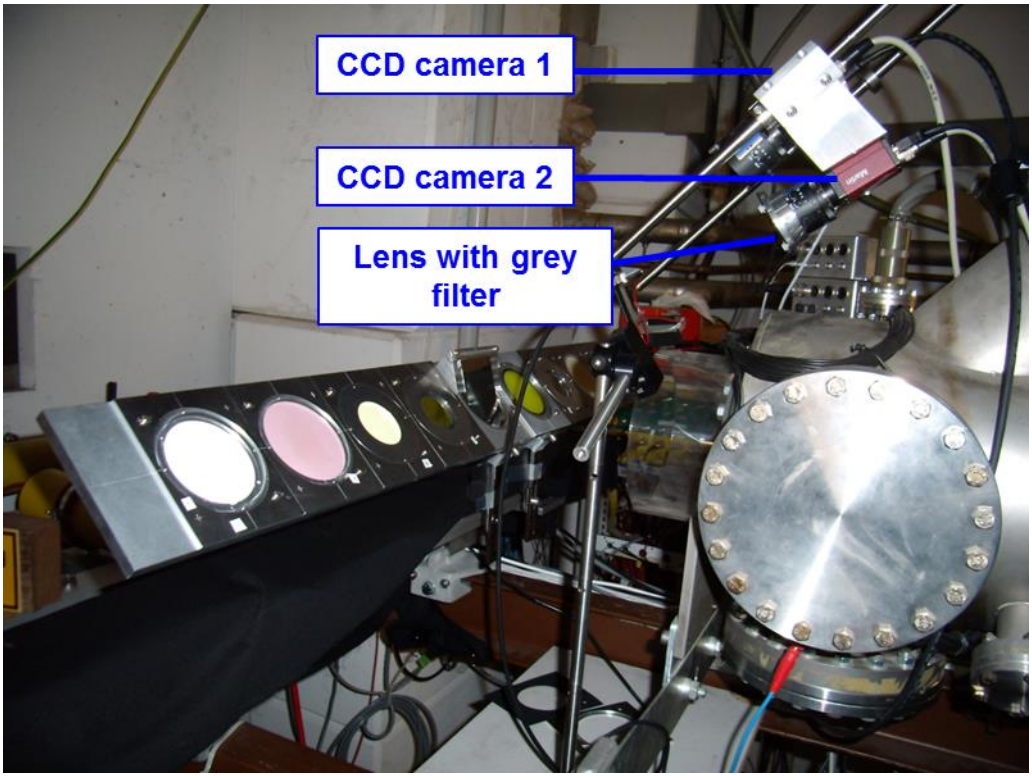


Figure 4.22: Modified experimental setup. The second camera with a grey filter was installed below the first camera for measurement of sensitive materials at high particle intensities.

## 4.4 Data analysis

### 4.4.1 Quantitative characterization

The examination and investigation of a huge set of numbers to obtain valuable, summarized information are called quantitative data analysis [84] [85]. To compare the luminosity distribution of different materials, the beam spot captured was projected in horizontal (*x),* and vertical direction *(y),* followed by characterization of the distribution. The useful quantities which characterize a distribution (mean, variance, skewness and kurtosis) were obtained from the probability density function of the distribution.

The expectation value is not a function of X but is a number dependent on the probability density function *g(x)*. The expectation value *E[X]* of the variable *X* is defined as:

for a continuous distribution:

$$E[X] = \frac{\int x f(x) dx}{\int f(x) dx} \tag{4.3}$$

where *f(x) is the probability function.*

and for a discrete distribution:

$$E[X] \equiv \mu \equiv \frac{\sum_i x_i w_i}{W} \quad ; \quad W = \sum_i w_i \tag{4.4}$$

where $w_i$ is the weight function. The mean value $\mu$ is the first moment which describes the center of the distribution. The variance 'σ' is the second moment which explains about the spread of the bulk density distribution.

$$V(X) \equiv \sigma^2 \equiv \frac{\sum_i w_i (x_i - \mu)^2}{W} \tag{4.5}$$

In general, the higher order central moments characterize mainly the shape of the distribution. The degree of asymmetry of the distribution is given by skewness while kurtosis gives the degree of flattening. The mean and the variance measured as first and second moment of the distribution are dimensional quantities while skewness and kurtosis are non-dimensional quantities [86]. The coefficient of skewness γ and kurtosis κ are defined as shown below.

The coefficient of skewness is positive when the distribution has a major tail on the right, while dominant over left leads to negative skewness. For a discrete distribution the skewness and kurtosis are given as [87]:

$$\mu_3 = \gamma = \frac{\sum_i w_i \left[\frac{x_i - \mu}{\sigma}\right]^3}{W} \tag{4.6}$$

$$\mu_4 = \kappa = \frac{\sum_i w_i \left[\frac{x_i - \mu}{\sigma}\right]^4}{W} - 3 \tag{4.7}$$

The value **3** makes the kurtosis 0 for a normal distribution.

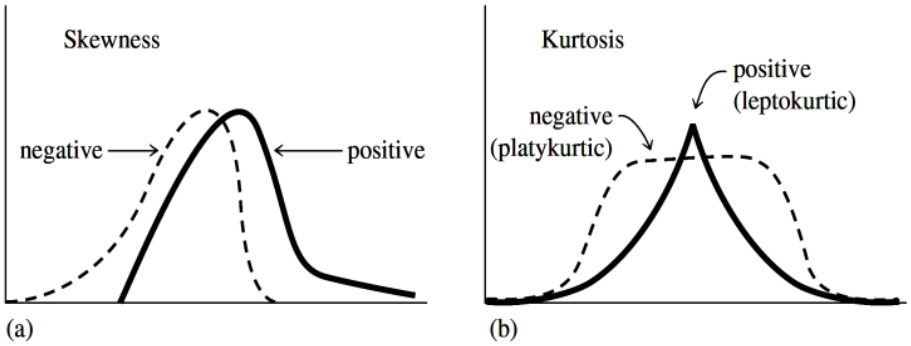


Figure 4.23: Examples for higher statistical moments Skewness and Kurtosis [86].

The kurtosis defines the peakedness of the distribution relative to the normal distribution. For a normal (Gaussian) distribution the kurtosis is 0. A positive value of kurtosis means the distribution is *leptokurtic* (more peaked) while negative is *platykurtic (flat top)* (see Figure 4.23). In addition the kurtosis values help to understand the process taking place in the material during irradiation. The propagation of kurtosis towards more positive values indicates the process of absorption while the more negative values indicate saturation. In this study the horizontal and the vertical distribution of luminescence intensity of different materials were characterised by calculating these important statistical moments $\mu$, σ, γ and κ.

## 4.4.2 Projections and background subtraction

The beam spot and the background image captured in the CCD sensor were projected in *x* and *y* plane using the software called '*Image J*' [88], as shown in Figure 4.24. For making the projections a specific area was selected for all recorded images. This area is defined as region of interest (ROI). Due to a high radiation background in the experimental area hot pixels were generated in the CCD sensor. These hot pixels have much influence on the light output and beam profile. In order to eliminate the influence of these hot pixels, the projection of the beam spot was subtracted from the background projection.

The background picture was also projected in both axes with the same ROI as the beam image and the intensity in each position was subtracted. This background subtraction was performed for both the horizontal and vertical projections. The profiles of the background

picture and beam spot in horizontal direction before and after subtraction are shown in Figure 4.25. The smooth image profile obtained after background subtraction was used for further analysis. From these profiles the integral light output was calculated for each beam pulse. Since the measurements were performed with different iris openings at different intensities, the light output was normalised to the completely open iris. The light output from different materials was plotted as a function of particle intensity and was then compared.

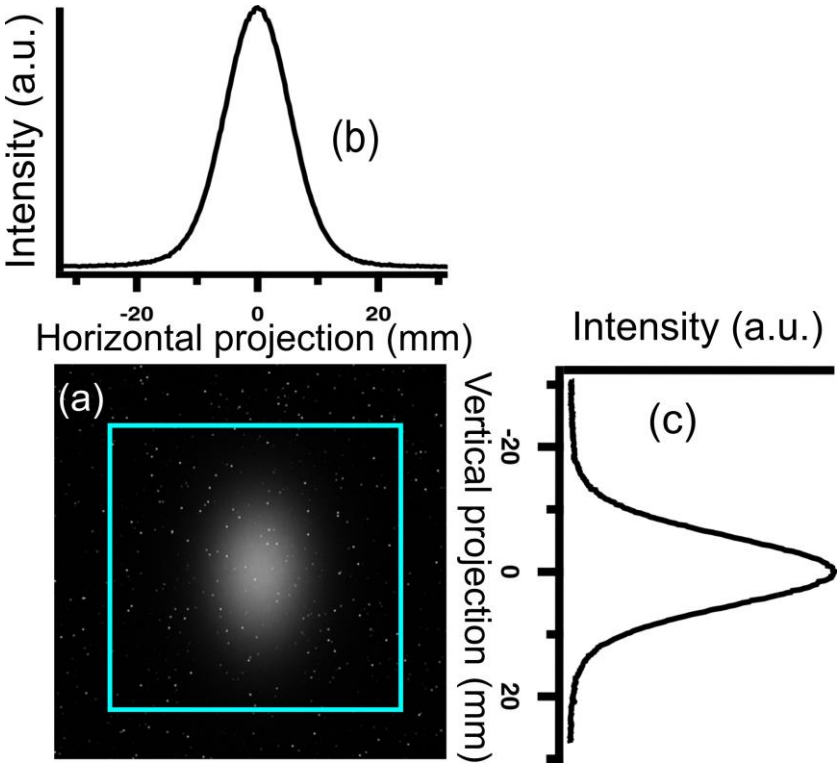


Figure 4.24: (a) The beam spot obtained from P43 scintillation screen recorded with standard CCD camera, irradiated with $5\times10^6$ particles of Neon ions. The beam spot is projected in horizontal (b) and vertical plane (c). The area inside the blue square was the selected region of interest (ROI).

### 4.4.3 Relative and absolute light yield

The light output from the scintillation screens depends on various parameters. The most important factors are the energy loss and ion species. Even the standard scintillators show non-proportional behaviour at high energy loss [89-90]. In order to perform a comparative study, the light outputs from the investigated materials were related to results from YAG:Ce (1 mm). The standard scintillator YAG:Ce (1 mm) was defined as completely efficient material producing 100 % light output. The efficiency of other materials with respect to YAG:Ce (1 mm) was calculated for the investigated ion beams.

For the absolute light yield calculation, the light outputs from various scintillation screens were normalised to the energy deposited in the material. Initially the light output obtained was normalised to a single particle and then normalised to energy loss. The light yield/MeV

was calculated for different materials for the entire set of investigated ions. From the results the behaviour of the screens with respect to ion species and energy loss was analysed.

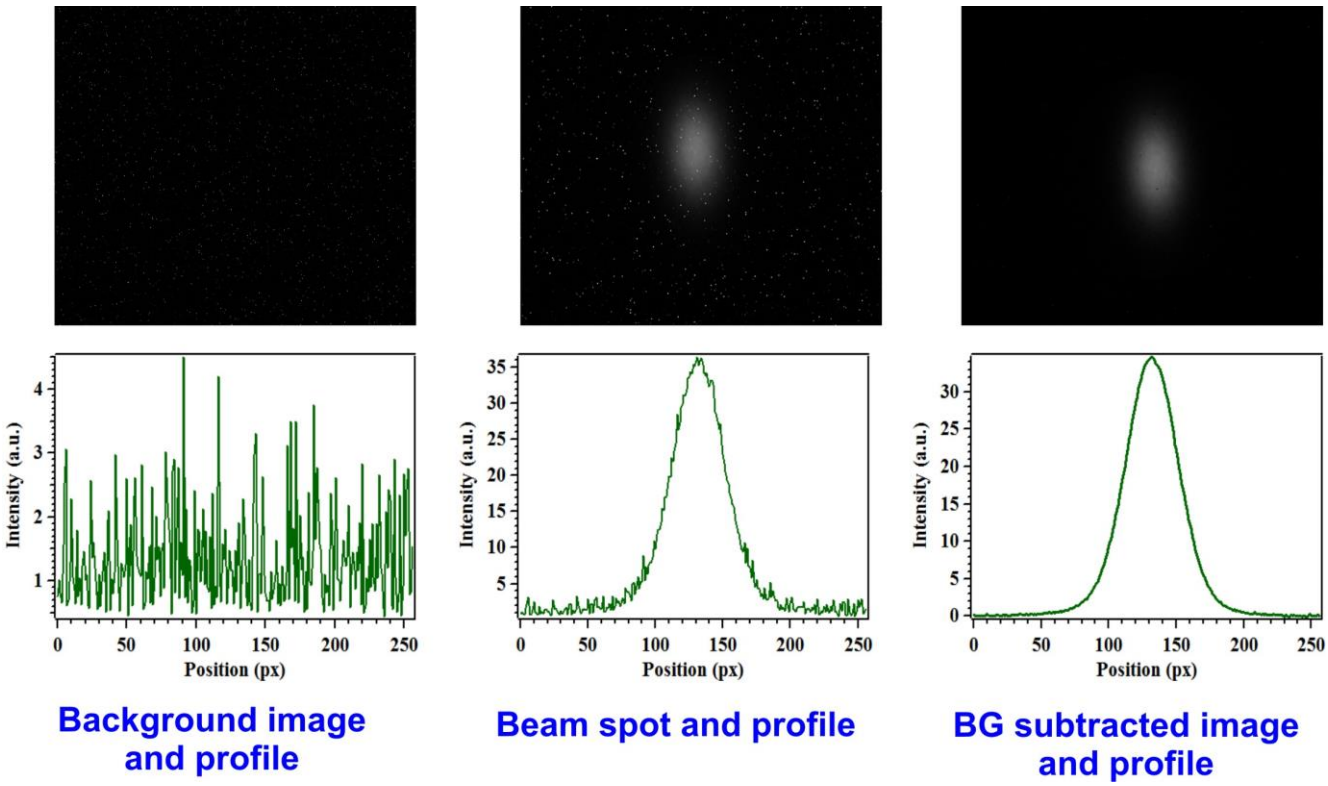


Figure 4.25: The background image recorded before beam delivery (left), beam exposure (middle) and the background subtracted images (right) for the horizontal direction for P46 screens irradiated with $10^6$ ppp of Tantalum ions.

### 4.4.4 Performed algorithms

The statistical moments were calculated from the image profile using four different algorithms to eliminate the contribution of the residual background to the profiles which remains even after background image subtraction. The four different algorithms are:

1. The raw data obtained after background subtraction
2. Reducing 10 % of the maximum intensity to eliminate the fluctuation in the tails
3. Changing the negative values to 0
4. Performing a Gaussian fit

The image width $\sigma$, skewness $\gamma$ and kurtosis $\kappa$ are calculated based on first three algorithms. From Gaussian fit only the width is calculated since the skewness and kurtosis were 0 for a normal distribution. In all these algorithms the image profile obtained from the same ROI was used.

The background subtraction shown in Figure 4.25 was carried out before performing the algorithms. The data obtained after background subtraction were considered as raw data. In

the first algorithm raw data were used directly for calculating the statistical moments. The X-axis of the profile was converted from pixel to mm scale using the resolution factor followed by the calculation of moments using the formulas (4.4), (4.5), (4.6) and (4.7).

In the second method, the intensity of the raw data was reduced by 10 %. Each data point in Y-axis was subtracted by a constant value which corresponds to 10 % of the maximum intensity. The negative values in the tails were set to 0 to compensate the over subtraction. This method is similar to selecting a small area (only the beam spot) as ROI, removing the tail part of the distribution. The image profile of the raw data and the intensity reduced are shown in Figure 4.26. From these data the image width, skewness and kurtosis were calculated.

Due to experimental uncertainties, a change in the measured background was noticed even within some ms time scale. The intensity of the hot pixels varies while making background picture and beam delivery. This leads to negative intensity values which are practically inapplicable. In this case, the data were modified by setting the negative values to 0 followed by the calculation of other statistical moments. An example of this method is shown in Figure 4.27.

Apart from these methods, the image width was calculated by performing curve fitting. Since the shape of the image profile resembles a normal distribution, a Gaussian curve fitting was performed and the width was calculated using the formula (4.8) [91].

$$Y = Y_0 + A\exp\left[-\left(\frac{x - x_0}{width}\right)^2\right] \tag{4.8}$$

The standard deviation $\sigma$ = width/$\sqrt{2}$.

The curve fitting was performed using the software IGOR PRO, which uses Levenberg-Marquardt algorithm [92-93] to search for coefficients in order to minimize the Chi-square through an iterative fit. An example of the fitted curve is shown in Figure 4.28.

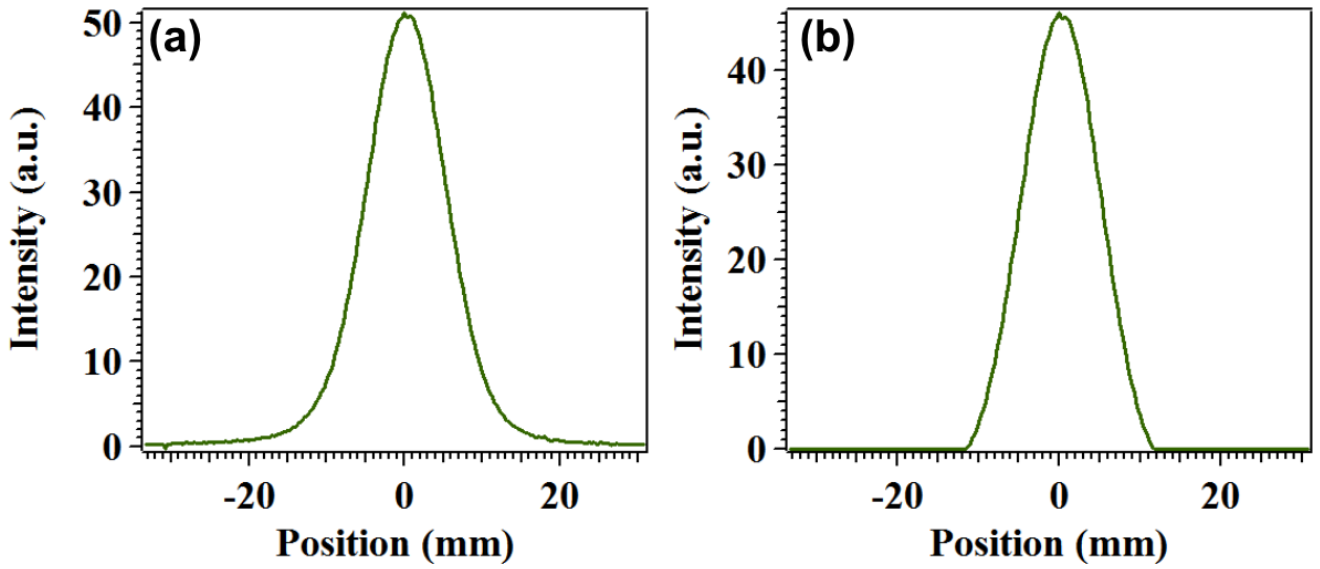


Figure 4.26: (a) Image profile in horizontal direction after background subtraction. This profile was used directly for image width calculation by the first algorithm. (b) Profile obtained after reducing the intensity. In this profile each data point in y axis was subtracted by ~5.1 arbitrary units (a.u.) which corresponds to 10 % of the maximum intensity. Both profiles were obtained from P43 screen for the same pulse number of Tantalum ions at $10^7$ ppp.

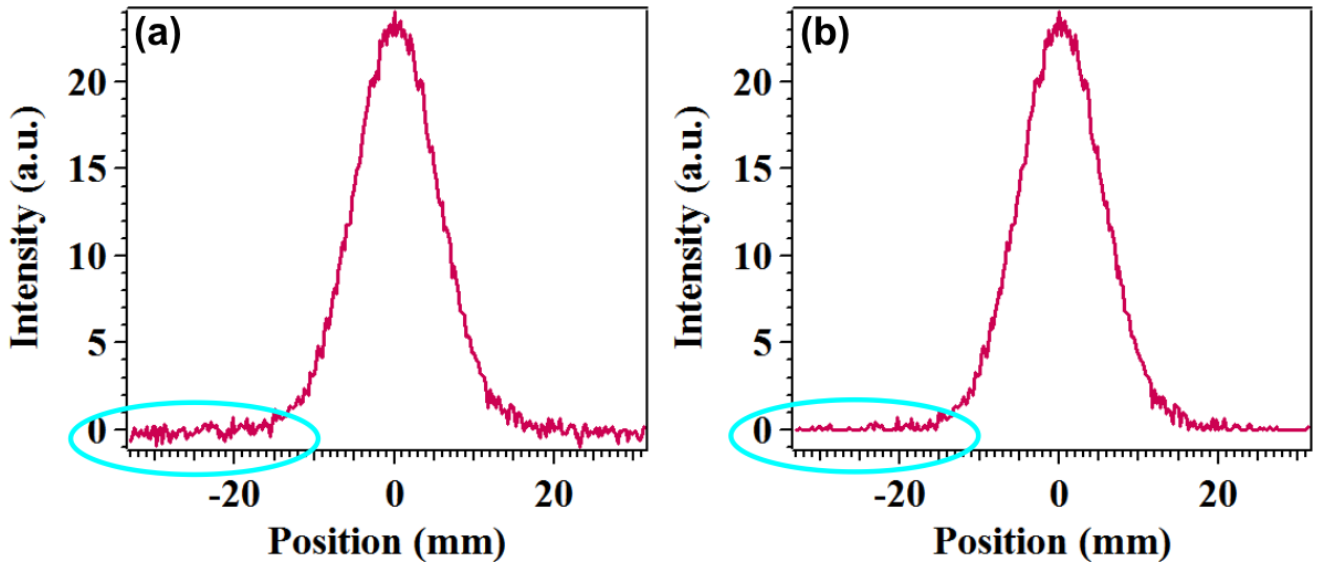


Figure 4.27: Image profiles obtained from $Al_2O_3$:Cr irradiated with $5\times10^5$ ppp of Neon ions. (a) Image profile obtained after background subtraction and (b) setting the negative values equal to 0.

## 4.5 Comparison of algorithms

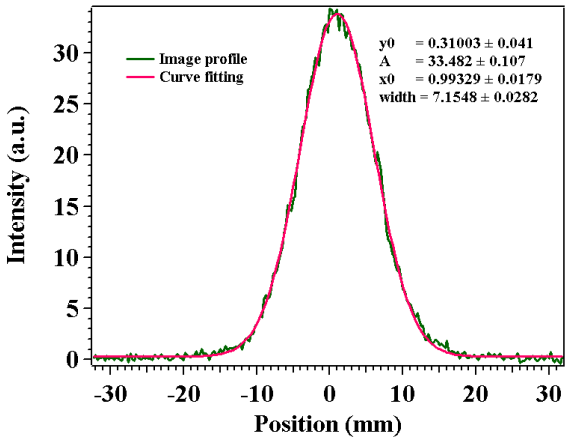


Figure 4.28: An example for curve fitting to measure the standard deviation. The green curve is the profile obtained after background subtraction and pink is the curve fit. Parameters: P43 screen irradiated with Tantalum at 275 MeV/u, $10^4$ ppp, 300 ms pulse length.

The statistical moments were calculated using various algorithms (Chapter 4.4.4) to understand their influence on the obtained results. The analysis is important for performing a relative comparison of imaging properties of the materials. The image widths 'σ' calculated from different scintillation screens exhibit the same tendency; however there are differences in the absolute numbers. Comparable results were obtained in both horizontal and vertical direction; the moments calculated in horizontal direction are presented.

The image reproduction behaviour recorded from different scintillation screens is discussed in detail in Chapter 5.1.5. In this section the results obtained by using different algorithms are briefly mentioned.

In the image width calculation, large statistical numbers were obtained from first algorithm described as in chapter 4.4.4 (Figure 4.29). Among the investigated materials, CsI:Tl shows the largest image width, with σ about 9.8 mm, whereas Herasil recorded 50 % less image width. $Al_2O_3$:Cr, $Al_2O_3$ and P43 have similar image reproduction behaviour, with σ within a deviation of ±4 %. The Y and Mg doped $ZrO_2$ samples did not show constant image reproduction behaviour. The image width increases with increasing particle intensity. This is due to the absorption of light produced in the material. The detailed description is given in chapter 5.1.5. The other algorithms also show similar results. The standard deviation obtained from the third algorithm (Figure 4.31) coincides with the results obtained from the first algorithm (Figure 4.29). The population of negative data was very much decreased due to low fluctuation of the intensity in the tail part of the beam distribution thus leading to similar results as obtained from first algorithm.

The image widths obtained from the other two algorithms are shown in Figure 4.30 and Figure 4.32. The relative reproduction behaviour of the materials remains constant in the performed algorithm and no significant difference was noticed. The 'σ' values obtained by reducing the intensity were small compared to other algorithms due to the small active area (ROI) selected for the calculation. The results obtained from different algorithms clearly state that the tendency reported by the materials is independent on the algorithm.

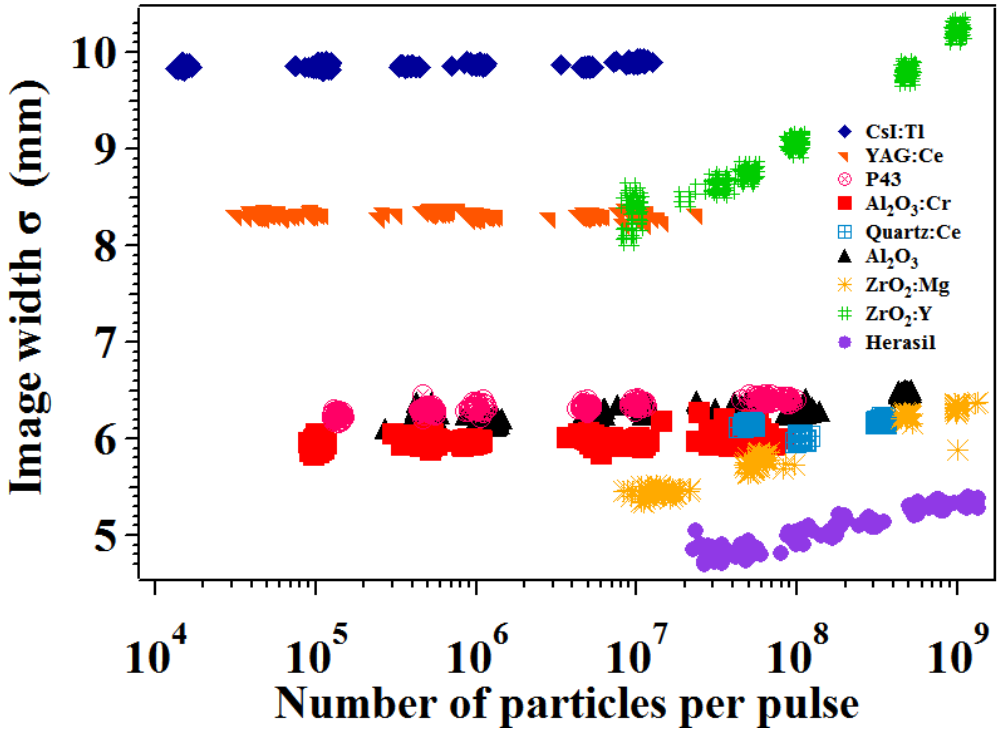


Figure 4.29: Image widths obtained from the data obtained after background subtraction (first algorithm). Beam parameters: Uranium at 269 MeV/u, $10^4$ to $10^9$ ppp, 300 ms pulse length, 0.25 Hz repetition rate.

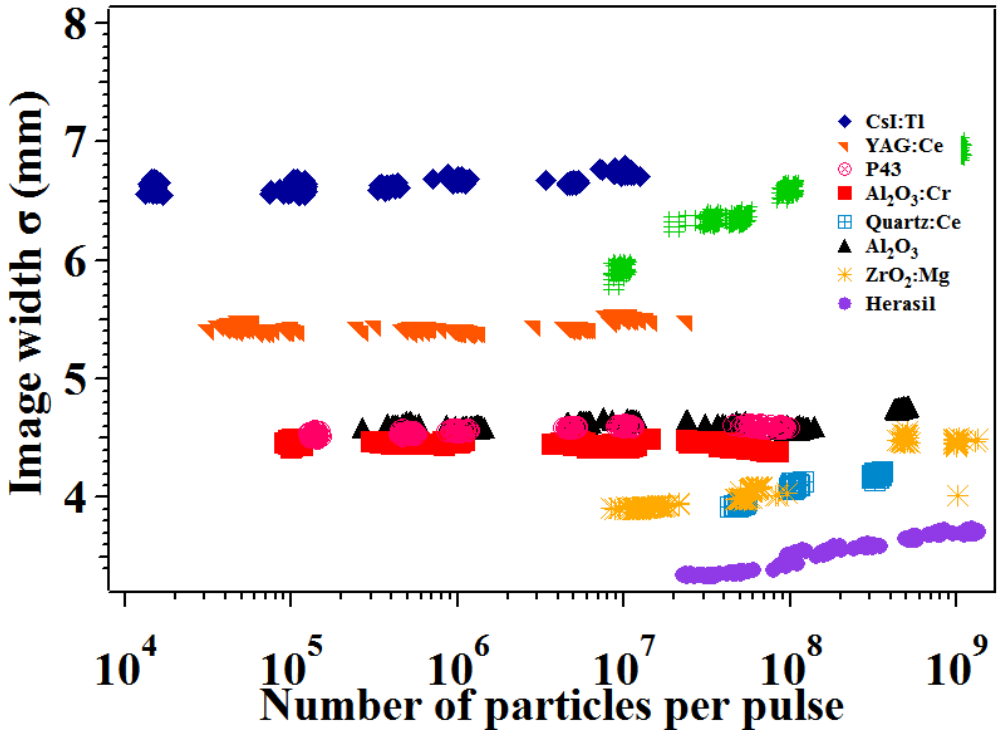


Figure 4.30: Image widths calculated by reducing the light intensity (second algorithm). Beam parameters: Uranium at 269 MeV/u, $10^4$ to $10^9$ ppp, 300 ms pulse length, 0.25 Hz repetition rate.

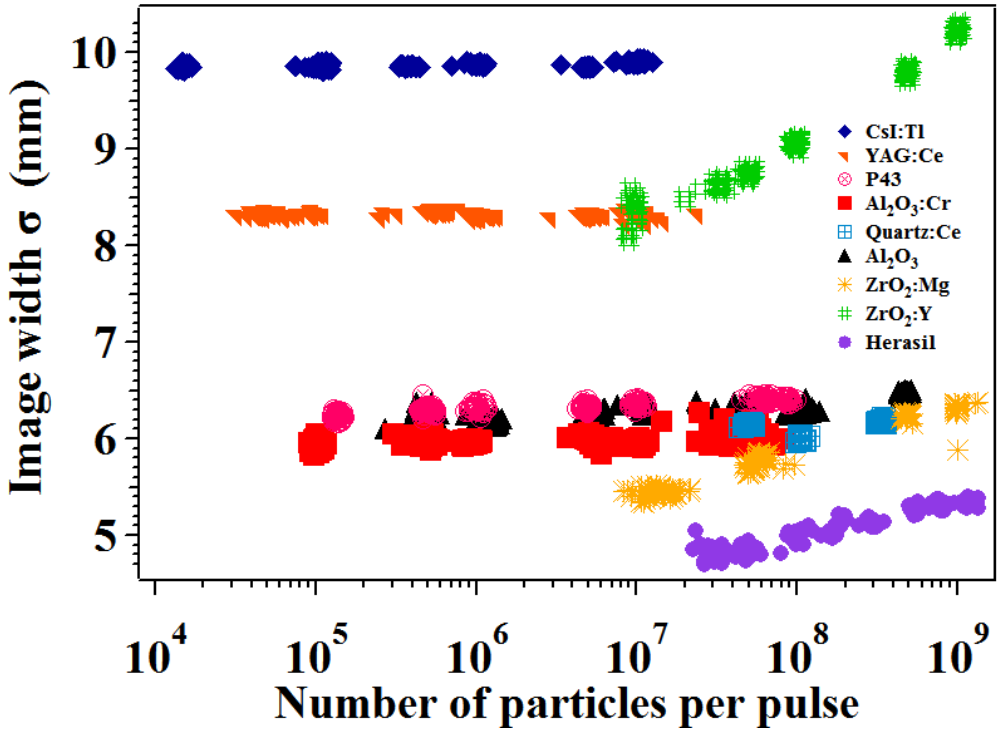


Figure 4.31: Image widths calculated by the third algorithm, normalising the negative values. The results obtained are similar to first algorithm.

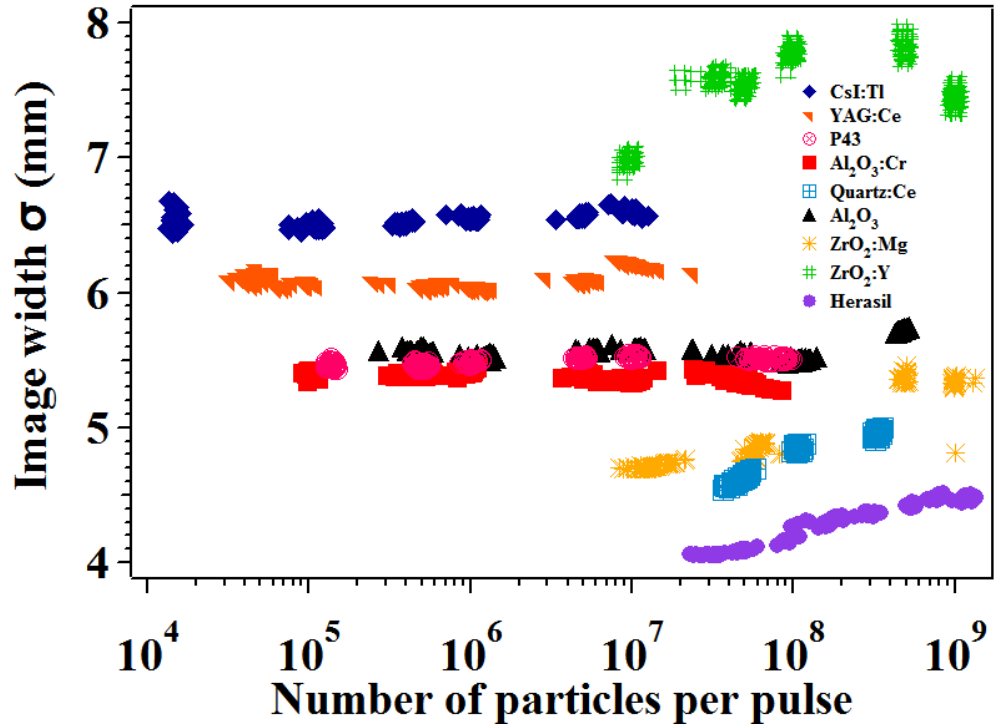


Figure 4.32: Image width obtained by performing Gaussian curve fits (fourth algorithm). Beam parameters: Uranium at 269 MeV/u, $10^4$ to $10^9$ ppp, 300 ms pulse length, 0.25 Hz repetition rate.

## 4.6 Raman spectroscopy

The radiation damage of the scintillation screen materials was analysed using Raman spectroscopy. The commercial Raman spectrometer HORIBA Jobin Yvon$^{TM}$ (HR800) with excitation wavelengths 632.8 and 473.5 nm was used. The system consists of a microscope confocally coupled with an 800 mm focal length spectrograph. The spectrograph is equipped with two switchable gratings, see Figure 4.33. The backscattered light enters the spectrometer through the same path of the incoming beam (180° system). After passing through the filter, the backscattered light is focussed into the monochromator with grating 1800 lines/mm through the confocal hole and a slit. The monochromator separates the Raman light into its spectral contribution before hitting the CCD detector. The CCD detector forwards the signal to the computer [94]. This setup allows to perform the measurements with a resolution of 0.3 $cm^{-1}$.

The spectra were recorded directly from the sample in both irradiated and unirradiated spots (area without any ion impact). The radiation induced damage in the materials were analysed from the spectra obtained.

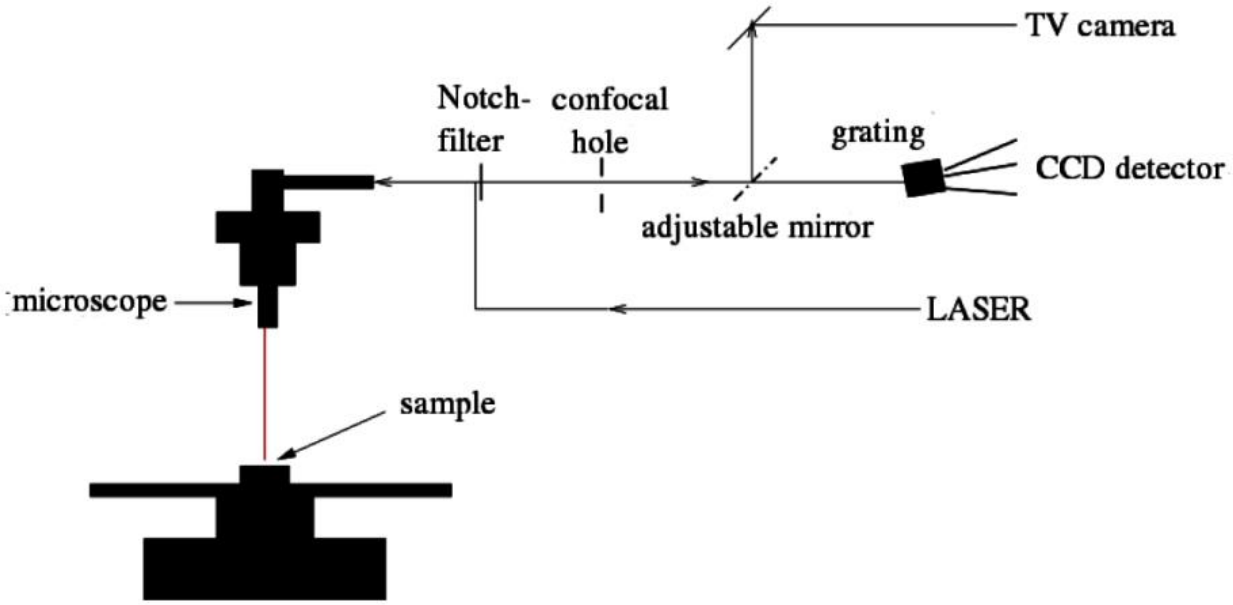


Figure 4.33: Schematic representation of Raman spectrometer [38].

## 4.7 X-ray diffraction

For X-ray diffraction, a Bruker D8 Advance X-ray diffractometer in a standard powder diffractometric set-up was used. It was operated at 40kV and 40mA with Cu $K_\alpha$ (8047 eV) radiation without a monochromator. The slits were set as follows: primary slit 0.5 mm, secondary slit 0.5 mm, and detector slit 0.1 mm. The measurements were performed in Bragg-

Brentano geometry where the X-ray source and the detector are kept in symmetric position, with the incident angle θ being between the X-ray source and the sample and the diffraction angle 2θ being between the incident beam and the X-ray detector. Thus, the diffraction vector is always normal to the surface of the sample. For powders as well as for polycrystalline materials with a large number of crystallites, there are always ones aligned in such a way that they diffract. Thus, all plane orientations will be given, leading to all possible reflexes. This geometry was chosen because of the mostly polycrystalline character of the ceramic scintillator materials.

## 4.8 UV-Vis Absorption spectroscopy

UV-Vis absorption spectra were taken with a Lambda 900 UV/Vis/Nir spectrometer of Perkin Elmer. It is capable of measuring in a wide wavelength region from 185 – 3300 nm with a wavelength accuracy of 0.08 nm in UV/Vis and 0.32 nm in NIR. It is equipped with an integration (Ulbricht) sphere for quantification.
The spectra were de-convoluted to identify the individual color centers formed by radiation damage.

# 5 Results and Discussion

## 5.1 Linearity measurements

The scintillation screen to be installed as beam diagnostic device in the FAIR accelerator should have a large working region coinciding with particle intensity range of the double ring accelerator. A stable performance of the scintillation screen is mandatory from low to high particle intensity. Irradiating the screens with varying particle intensity is referred to as linearity measurements. Linearity measurements were carried out to explore the working region of each screen. The data acquisition was started when the first light was observed from the screens for the completely open iris setting. The iris opening was reduced with increase in beam intensity in order to avoid saturation of the CCD sensors. The maximum threshold of the measurement was given by minimal iris opening settings and the maximum intensity available in the experimental area. In general the maximum beam intensity was around $10^9$ ppp.

### 5.1.1 Preliminary experiment

A preliminary measurement was carried out using the Uranium ions accelerated to maximum kinetic energy of 300 MeV/u, to have an overview on the behaviour of the screens on irradiation. The scintillation screens except P46 and YAG:Ce (0.25 mm) were irradiated with $10^4$ to $10^9$ ppp. Each screen was irradiated with 25 beam pulses and the scintillation light was recorded. The measurements were performed with maximum camera gain to estimate the maximum light produced by the screens (Figure A 1 and Figure A 2 in the Appendix). This preliminary experiment helped to identify radiation sensitive samples and to estimate the working region of some ceramic scintillators such as Y- and Mg- doped $ZrO_2$.

### 5.1.2 Results from Carbon ions

The investigation with light weight ions was carried out with Carbon ($^{12}_{6}C$). These ions were accelerated to the maximum available energy of 300 MeV/u. These light ions deposit only few MeV of kinetic energy in the beam line foils. The energy of the ions while reaching the target was 296 MeV/u. The energy deposited in the samples was a factor 100 less when compared to the energy deposited by Uranium ions. The total energy deposited in YAG:Ce (1 mm) sample by Carbon ion beam was 0.04 GeV corresponding to 1.5 % of total kinetic energy whereas the energy deposited by Uranium was 10.5 GeV corresponding to 16 % of the total kinetic energy.

In the preliminary measurements, the Y- and Mg- doped $ZrO_2$ and Herasil showed an unstable behaviour during irradiation. Therefore YAG:Ce (1 mm), P43, $Al_2O_3$ and $Al_2O_3$:Cr were investigated. Each target was irradiated with 30 ion beam pulses. The measured light output and statistical moments in horizontal plane were plotted versus particle intensity (Figure 5.1 to Figure 5.4). The statistical moments calculated for the vertical plane are

presented in Figure A 3 to Figure A 6. Each data point in the graph represents one beam pulse. The largest light output was detected from YAG:Ce (1 mm) screen at $10^6$ particles with maximum camera gain.

- A remarkable linear light output over 3 orders of magnitude of particle intensity was obtained from the scintillation screens (Figure 5.1).
- The highest light output was recorded for the YAG:Ce (1 mm) single crystal.
- The powder screen P43 produced almost 40 % of light output in comparison to YAG:Ce (1 mm).
- The light output from $Al_2O_3$:Cr was well below P43, but a factor 10 more than $Al_2O_3$.
- In the profile reproduction, the scintillation screens P43, $Al_2O_3$ and $Al_2O_3$:Cr reproduce the image width within a difference of ±4 % whereas YAG:Ce (1 mm) produced larger σ values (Figure 5.2).
- The image width obtained from YAG:Ce (1 mm) was 12 % larger in comparison to the other screen materials.
- The calculated skewness (Figure 5.3) shows that the peak of the distribution obtained from the screens was symmetrically distributed over the center.

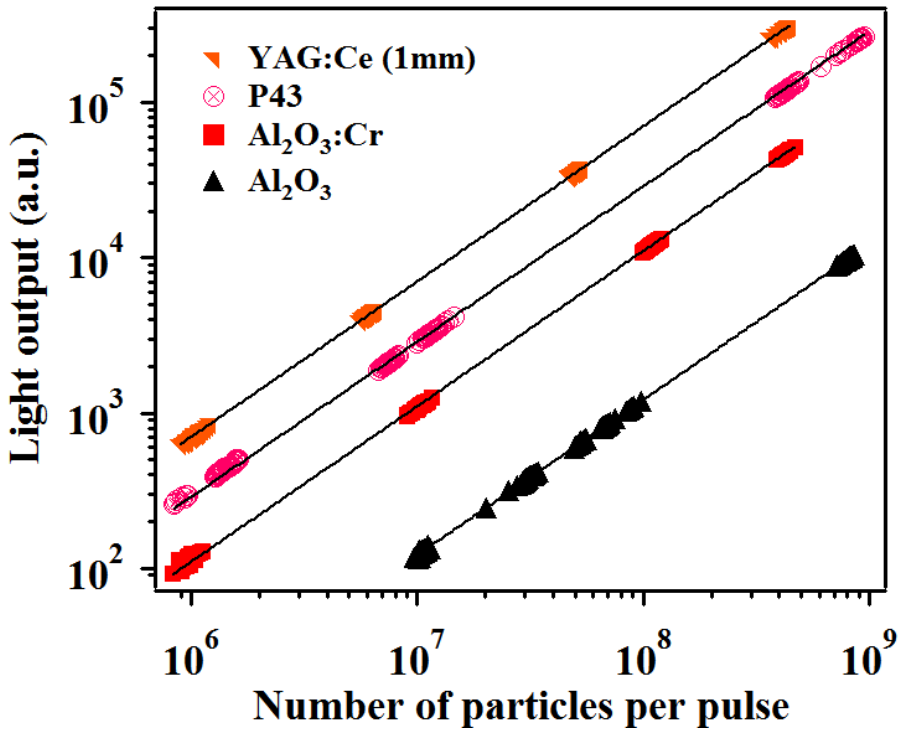


Figure 5.1: Light output from various scintillation screens vs. particle intensity. Beam parameters: Carbon at 296 MeV/u, 0.3 s pulse length and 0.25 Hz repetition rate.

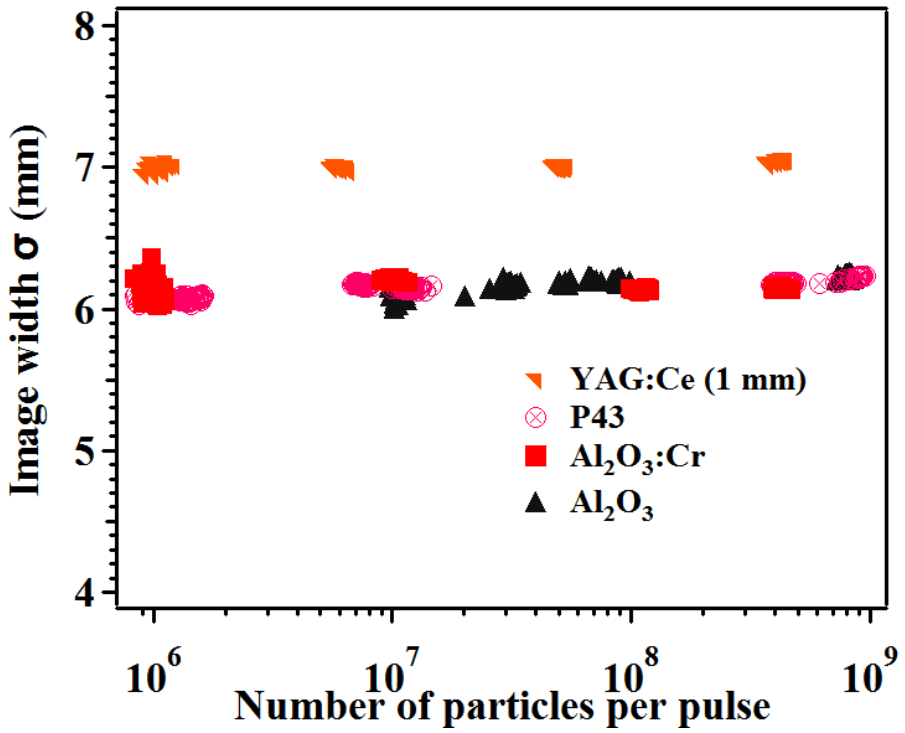


Figure 5.2: Image width σ calculated using Gaussian fit (algorithm 4, Chapter 4.5) for different scintillation screens. The beam parameters are the same as Figure 5.1.

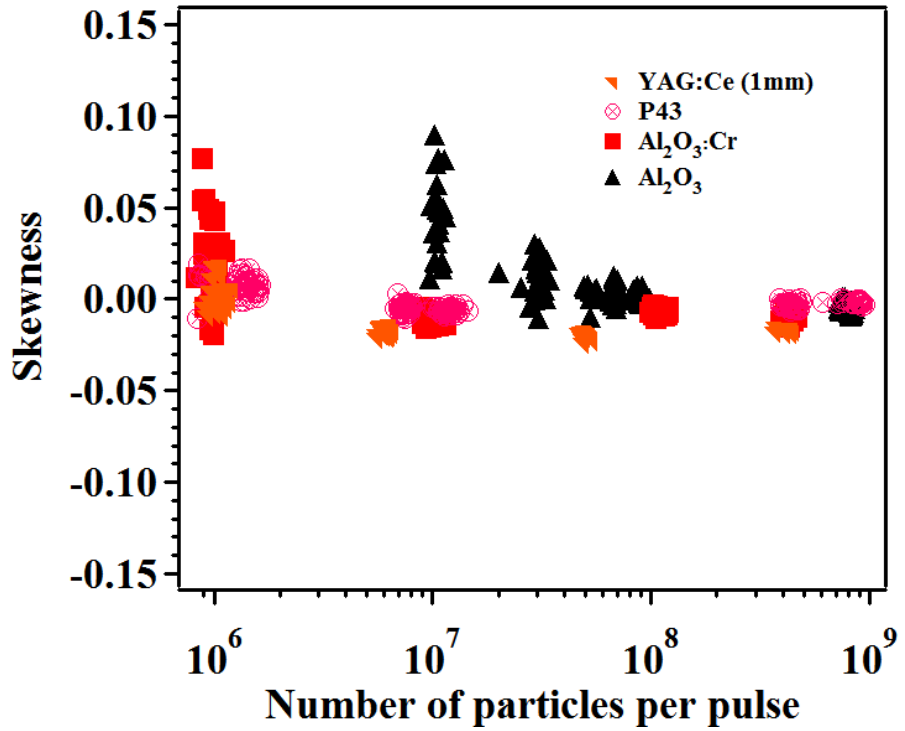


Figure 5.3: Skewness calculated from the profiles acquired for the Carbon ion beam. The beam parameters are the same as Figure 5.1. The values around zero indicate that the peak was symmetrically distributed over the center. $Al_2O_3$ with its low light output shows a large scatter at $10^7$ ppp.

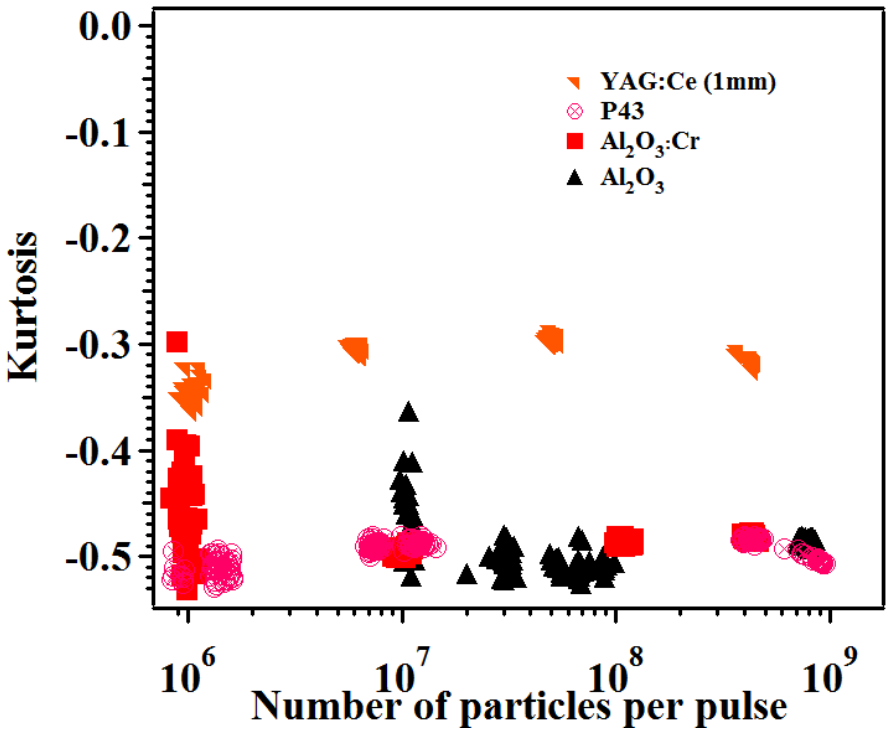


Figure 5.4: Kurtosis calculated for Carbon ion beam image profiles. The image profile obtained from P43, $Al_2O_3$:Cr and $Al_2O_3$ exhibit similar peakedness. The fluctuation in the lower intensity range is due to the low signal - to - noise ratio. The beam parameters are same as Figure 5.1.

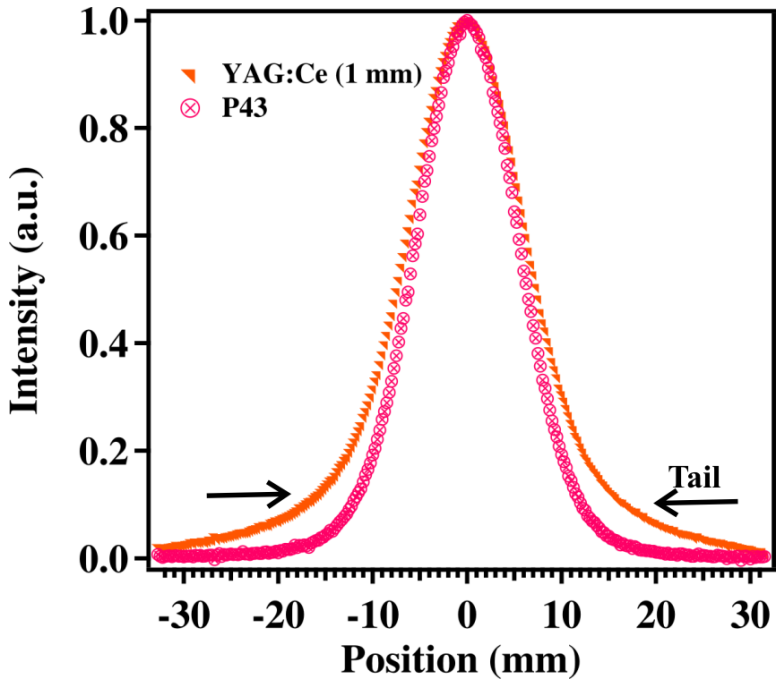


Figure 5.5: Normalized horizontal projection of the beam spot obtained from P43 and YAG:Ce (1 mm) screens for Carbon ion beams. A significant tail was noticed in YAG:Ce (1 mm) crystal. The $\sigma$ calculated from these profiles shows a difference up to 12 %.

The significant tail structure noticed from YAG:Ce (1 mm) samples compared to P43 screens shown in Figure 5.5 contributed to the larger σ values. In addition, the image profile from YAG:Ce (1 mm) shows more peakedness (larger kurtosis) compared to other three screens shown in Figure 5.4.

### 5.1.3 Results from Neon ions

In addition to Carbon ions, the scintillation screens were investigated also with Neon ions, another representative of light weight ions. The kinetic energy of the ions while reaching the targets was 295 MeV/u. The same samples irradiated with Carbon ions were also used for the Neon ion experiment. CsI:Tl was included in order to have a comparative study of the light output. In addition to these samples, two new samples, namely YAG:Ce (0.25 mm) and P46 powder screen obtained from Crytur Ltd [95], were also included. The single crystal YAG:Ce (Czochralski method) was grounded and deposited on a glass substrate to form a P46-type screen. The data acquisition was started from $4\times10^5$ particles and further progressively extended up to $10^9$ particles.

The results obtained from Neon ion irradiation are listed below.

- The light output from the screens shows a very linear behaviour over 3 orders of particle intensity (Figure 5.6).
- Among the investigated materials, CsI:Tl shows the highest light output.
- The results obtained from samples YAG:Ce (1 mm), P43, $Al_2O_3$:Cr and $Al_2O_3$ were similar to those from the previous Carbon ion investigation (Figure 5.6).
- Among the two new YAG:Ce screens prepared from the same source material, a higher sensitivity was recorded by the P46 powder screen than the YAG:Ce (0.25 mm) single crystals.
- A factor of two more light output was registered from P46 screen irrespective of the thickness of the materials. This indicates that the powder screen P46 is more sensitive to ionizing radiation than YAG:Ce (0.25 mm) crystals.
- To authenticate the linear behaviour, the relative error between the measured data and the fitted curve was calculated, which lies within the acceptable region of ±15 % (Figure 5.7).

In image reproduction, the new materials included exhibits comparable results with the other powder screen P43 and aluminium oxide ceramics. The statistical moment σ calculated coincides within ±4 % error (Figure 5.8) and it remains constant over the measured particle dynamic range. Similar behaviour was noticed also from the vertical projection (Figure A 7 and Figure A 8). The higher statistical moments calculated in horizontal plane (Figure 5.9 and Figure 5.10) and in vertical plane (Figure A 9 and Figure A 10) showed that the shape of the image profiles remains constant over the measurement. In Figure 5.11 the comparison of

profiles obtained from $Al_2O_3$, $Al_2O_3$:Cr, P43, YAG:Ce (0.25 mm) and P46 shows the same behaviour, with σ within a difference of 4 %. The image profiles of the standard scintillators were compared to the P43 profile in Figure 5.12. The broad profiles recorded from YAG:Ce (1 mm) and CsI:Tl resulted in larger image widths.

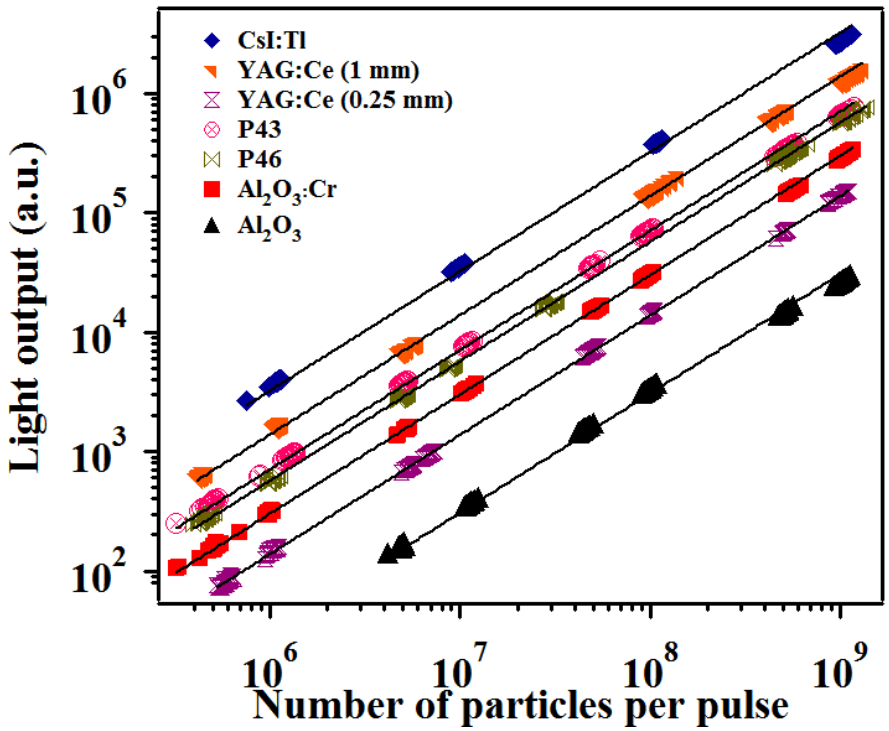


Figure 5.6: Light output from various scintillation screens vs. particle intensity. Beam parameters: Neon at 295 MeV/u, 0.3 s pulse length and 0.25 Hz repetition rate.

### 5.1.4 Results from Argon ions

Argon was chosen as an example of a medium heavy ion. The final kinetic energy of the ion was 292 MeV/u. Particle intensities ranging from $5\times10^4$ to $10^9$ particles were applied to some selected scintillators such as YAG:Ce (1 mm), P43, $Al_2O_3$:Cr and $Al_2O_3$.

- The observed light output confirms once again the linear behaviour of screen over 4 orders of magnitude see Figure 5.13.
- A factor of 10 difference in light output between $Al_2O_3$:Cr and $Al_2O_3$ was recorded.
- Unstable image reproduction behaviour was recorded from the scintillation materials in horizontal (Figure 5.14) and vertical plane (Figure A 12).
- The σ values obtained from YAG:Ce (1 mm) and $Al_2O_3$:Cr show small variations whereas a sudden increase in the width was recorded from P43 screen at $4\times10^6$ particles.

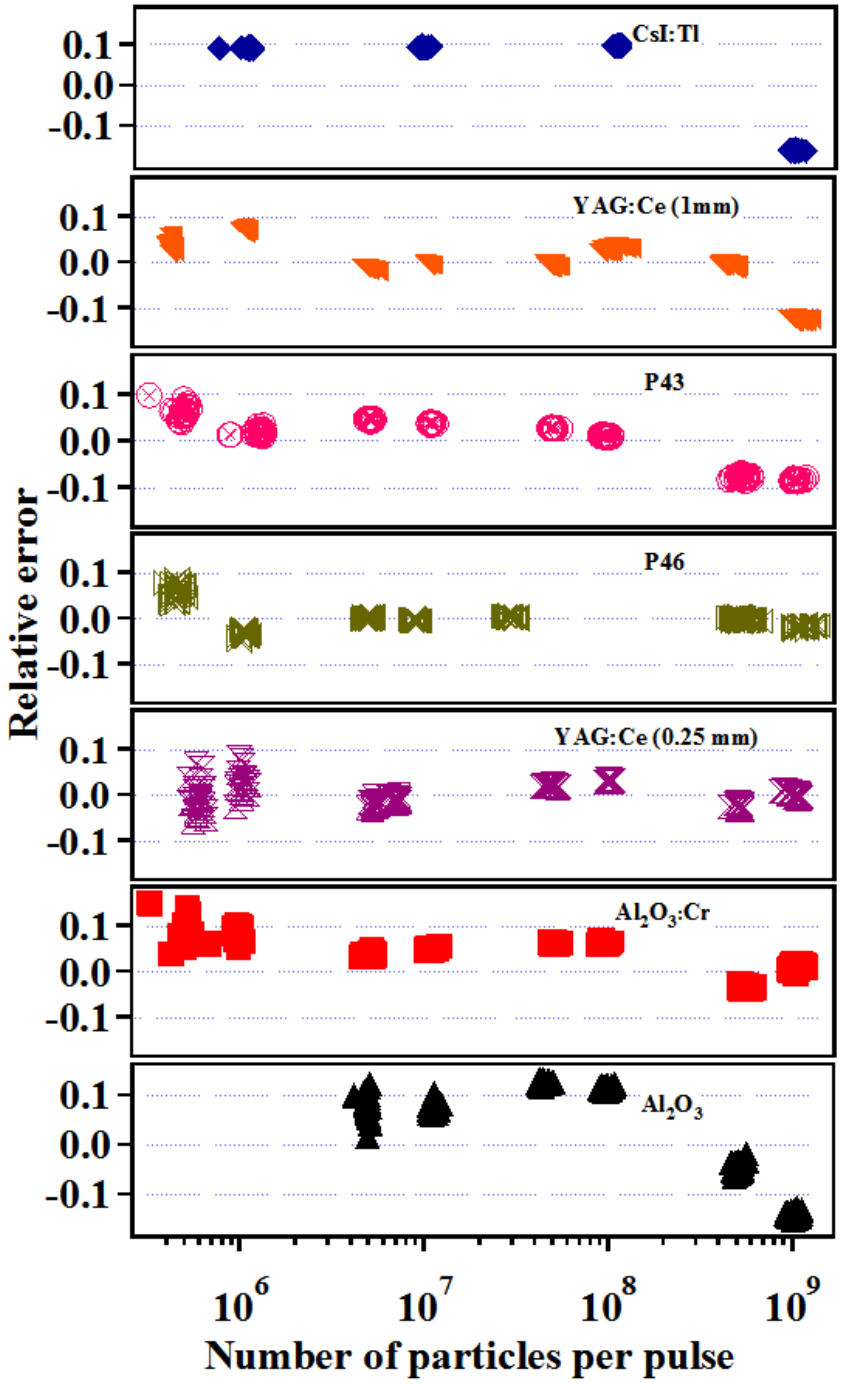


Figure 5.7: The plot shows the relative error calculated between the light output and the linear fit data for Neon ion beams. The light output obtained from the samples mostly shows a linear behaviour with an error around ± 15 % over the dynamic range.

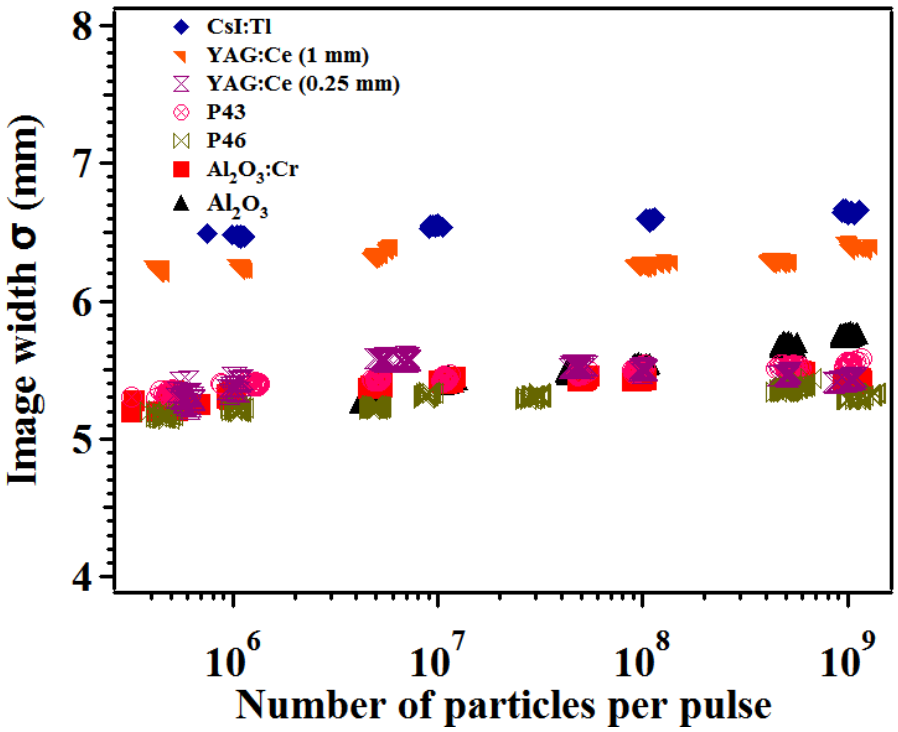


Figure 5.8: Image width σ calculated using Gaussian fit (algorithm 4, Chapter 4.5) for different scintillation screens. Beam parameters are same as Figure 5.6.

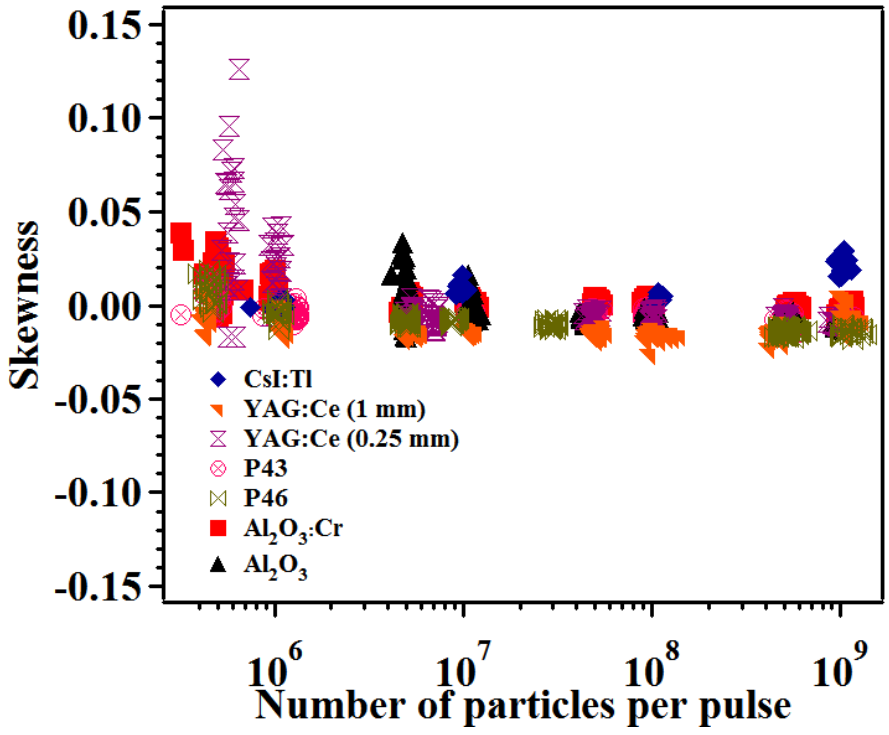


Figure 5.9: The skewness calculated from the profiles for Neon ion beam. The dispersal of the values around zero indicates the symmetrical distribution of the data.

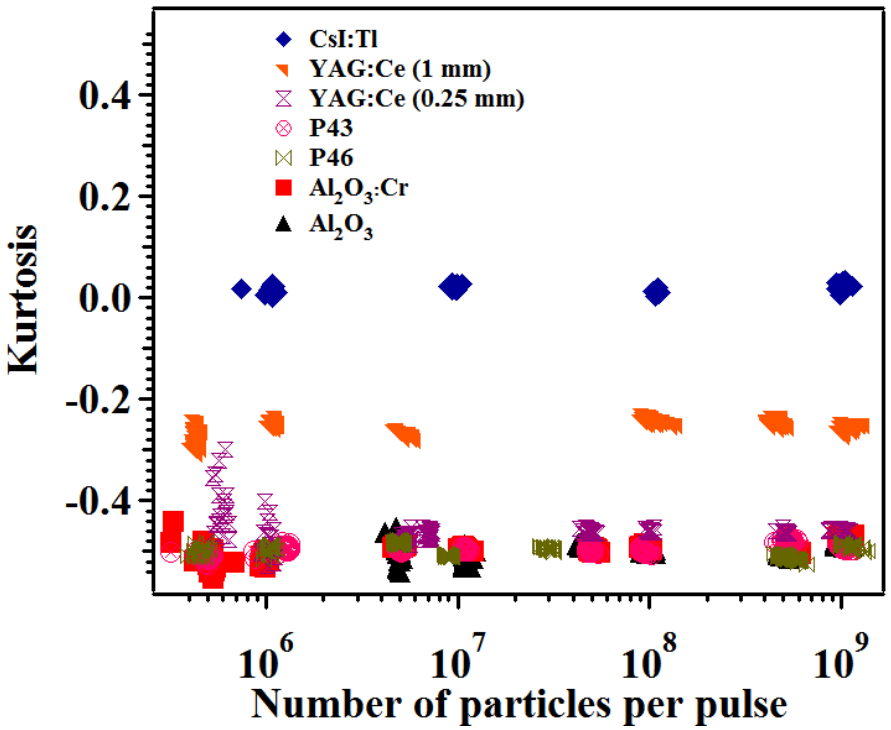


Figure 5.10: The statistical moment kurtosis obtained for Neon ion beams of 295 MeV/u. The kurtosis was stable over particle intensity indicating that the image profile remains constant over the measurement. The fluctuation at lower intensity was due to low signal-to-noise ratio.

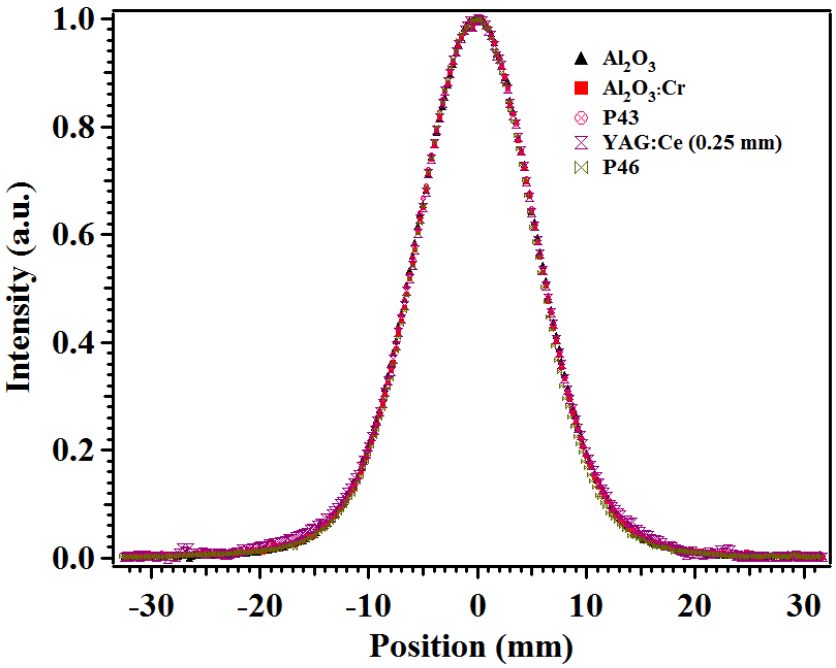


Figure 5.11: Beam image profiles obtained from the scintillation screens in horizontal direction. The image widths obtained from these profiles show a relative difference of ±4 %.

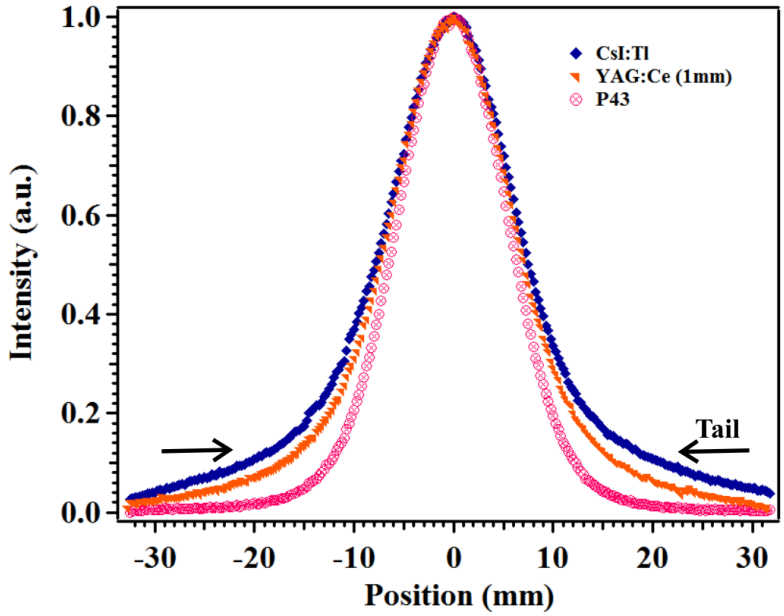


Figure 5.12: Normalised beam image profiles obtained from the standard scintillation screens in horizontal direction. A significant tail structure was registered from CsI:Tl and YAG:Ce (1 mm) in comparison to P43 screen profiles. Beam parameters are the same as in Figure 5.6.

The image width from pure $Al_2O_3$ screen increased gradually with particle intensity. This phenomenon raised the question on the stability of the screens. Two factors can influence the obtained image width: (a) the intrinsic property of the screen, (b) the experimental beam conditions. When the scintillation screens have poor radiation stability and less sensitivity, the light output from the screens decreases upon continuous irradiation.

The scintillation light was absorbed by the defects in the materials produced during irradiation, resulting in image broadening. At higher intensities the number of excitations available for the recombination process decreases due to quenching effects as mentioned in chapter 3. This saturation phenomenon also has a possibility to induce image broadening. These two effects can be differentiated using the fourth statistical moment kurtosis. The propagation of kurtosis towards positive values indicates absorption and towards negative values indicates saturation.

The kurtosis calculated for P43, $Al_2O_3$:Cr and $Al_2O_3$ remains constant over the measurement range in both horizontal plane (Figure 5.15) and in vertical plane (Figure A 14). This states that the image broadening was not due to absorption or saturation in the scintillation screen. Besides the light output obtained remains linear over the dynamic range. Thus the variation in the $\sigma$ values occurred due to unstable beam condition and not because of the intrinsic property of the screen.

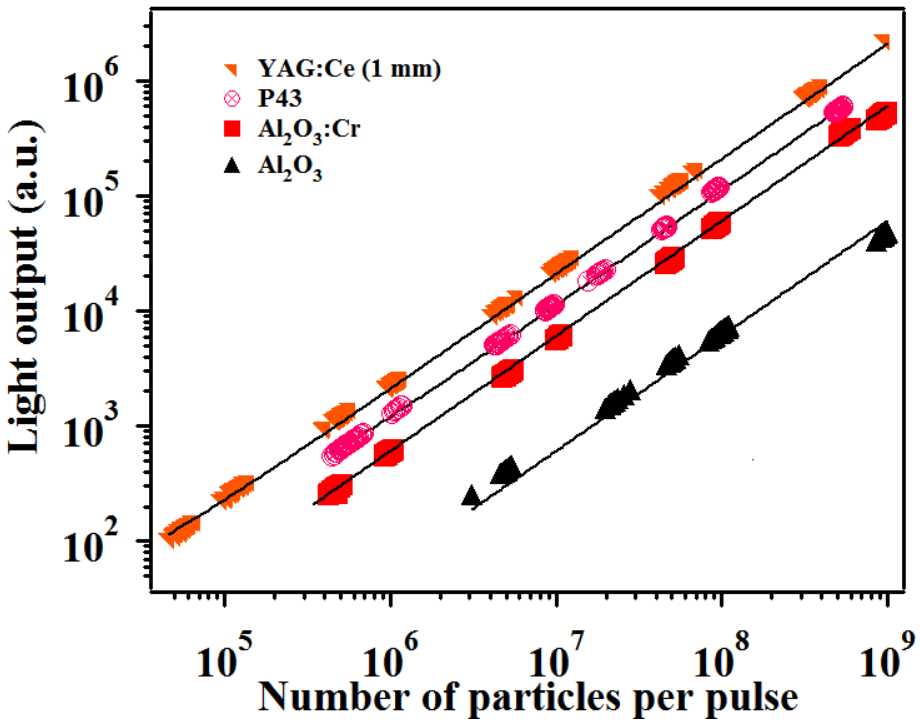


Figure 5.13: Light output obtained from selected scintillation screens. Beam parameters: Argon at 292 MeV/u, 0.3 s pulse length and 0.33 Hz repetition rate.

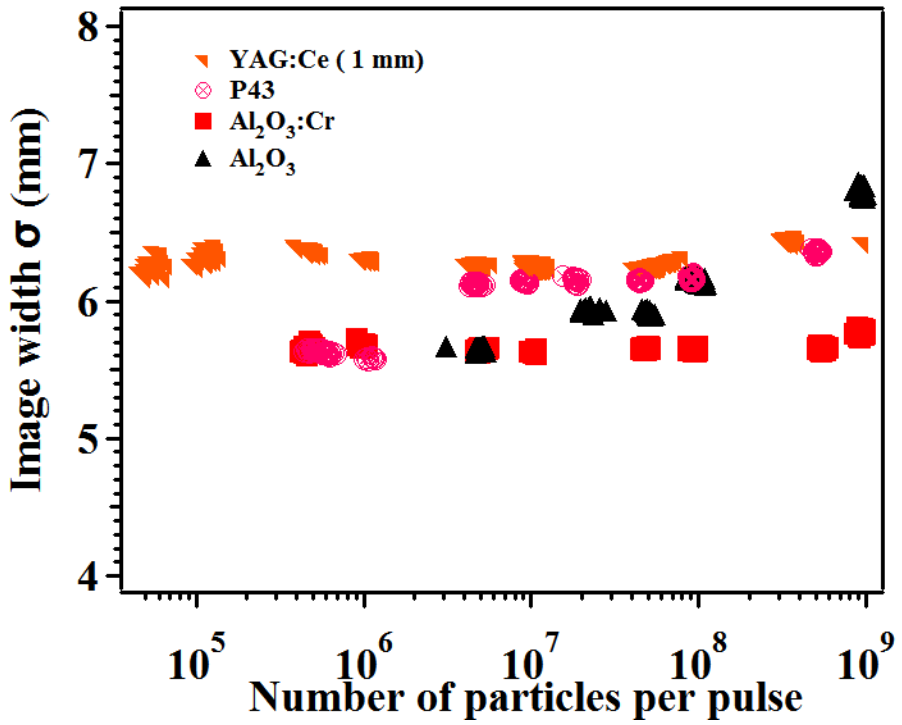


Figure 5.14: Image width σ calculated using Gaussian fit (algorithm 4, Chapter 4.5) for Argon ion beam. The fluctuation in the obtained image width was most probably due to the unstable beam conditions. Beam parameters are the same as in Figure 5.13.

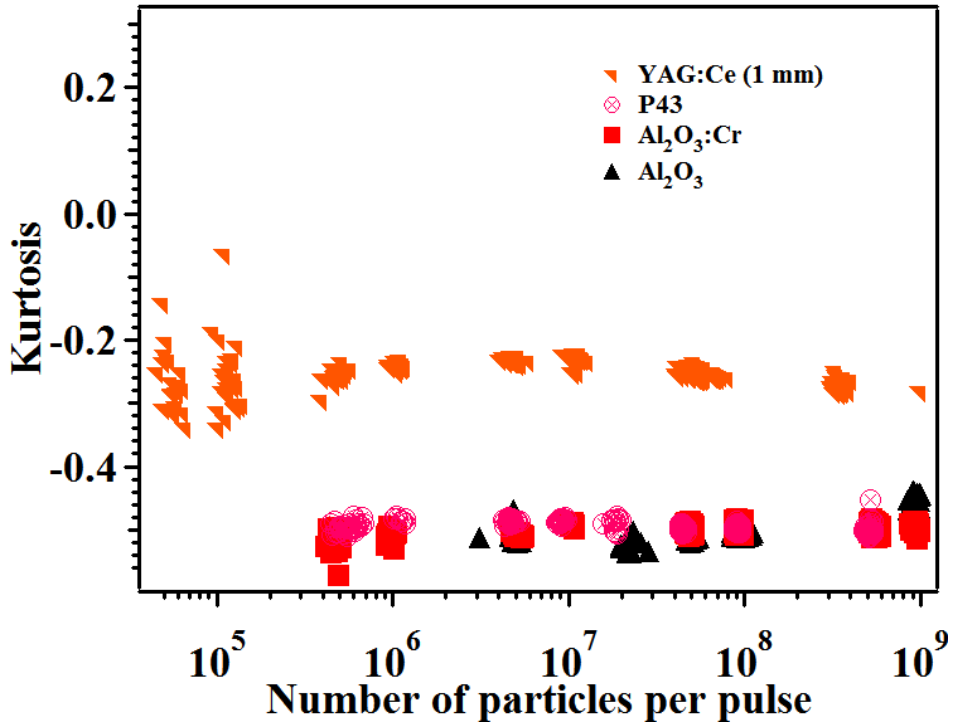


Figure 5.15: Kurtosis calculated for Argon ion beams. The stable trend obtained for P43, $Al_2O_3$:Cr and $Al_2O_3$ suggests that the variation in σ values was due to unstable beam conditions during the experiment. Beam parameters are the same as in Figure 5.13.

### 5.1.5 Results from Uranium ions

The Uranium ion beam with particle intensities ranging from $10^4$ to $10^9$ ppp was accelerated to 300 MeV/u. After passing through the vacuum windows the ion beam reached the scintillation screen with the kinetic energy of 269 MeV/u.

*The findings from the light output plot are listed below.*

- The highest light output was recorded from the standard scintillator material CsI:Tl.
- Scintillation light was observed from $10^4$ ppp which is the minimum number of particles accelerated in the SIS ring. The light output from the CsI:Tl screen increases linearly with the particle intensity, as shown in Figure 5.16.
- A linear light output over 3 orders of magnitude of particle intensity was acquired from YAG:Ce (1 mm) and P43 standard screens.
- The $Al_2O_3$:Cr ceramic material also produced similar results as standard scintillators.
- The light output from the Ce doped quartz glass also showed a linear behaviour. The light from the doped glass was higher than the one of the undoped glass material.

- The pure aluminium oxide produced one order of magnitude less light than Chromox. For the minimum gain setting the first measurable scintillation light was observed from $Al_2O_3$ at an intensity of $10^6$ ppp.

- After irradiation, the color of the $Al_2O_3$ sample changed from pale white to yellow.

- The lowest light output was observed from Herasil. Even though it has a linear behaviour at higher intensity, it has a very poor sensitivity to ionizing radiation with respect to luminescence.

- Y- and Mg- doped $ZrO_2$ ceramics showed a very unstable light output behaviour. The light output from these screens decreased at higher particle intensity and deviated from the linear behaviour. Similar behaviour was noticed also in the preliminary experiment (chapter 5.1.1) see Figure A 1 and Figure A 2).

Due to the saturation of the CCD sensors the measurement with high particle intensity was limited for the standard scintillators like CsI:Tl, YAG:Ce (1 mm) and P43. Due to some technical restriction during the experiment, the Ce-doped quartz glass material was investigated only with higher particle intensities.

*The image reproduction behaviour of the screens with Uranium ions is listed below.*

- In the image reproduction, the largest image widths were recorded from $ZrO_2$:Y. In this sample the image width increased with particle intensity (Figure 5.17).

- Next to $ZrO_2$:Y, the standard scintillating crystals CsI:Tl and YAG:Ce (1 mm) produced larger image widths, see Figure 5.17.

- The opaque samples P43, $Al_2O_3$:Cr and $Al_2O_3$ reproduce the image width within a difference of ±4 %.

- The other three sample materials Quartz:Ce, $ZrO_2$:Mg and Herasil produced smallest image width compared to other materials.

- In Mg- and Y-doped $ZrO_2$, the absorption of light within the material leads to a decreased light output and therefore image deformation took place at higher particle intensity.

- The propagation of kurtosis (Figure 5.18) towards positive direction in $ZrO_2$:Y indicates the absorption of light produced within the materials.

- In $ZrO_2$:Y and $ZrO_2$:Mg the color of the sample changed as a result of irradiation. The $ZrO_2$:Y sample turned dark purple due to the formation of color centers (Figure 5.37), in analogy to findings for lower ion energies [9, 96-97].

- In the standard scintillation screens, the broadening of the image profiles was attributed to multiple photon interactions and light transportation in thick scintillators [98].

- Within the investigated materials, a difference up to 50 % in image width was recorded between $ZrO_2$:Y and Herasil.

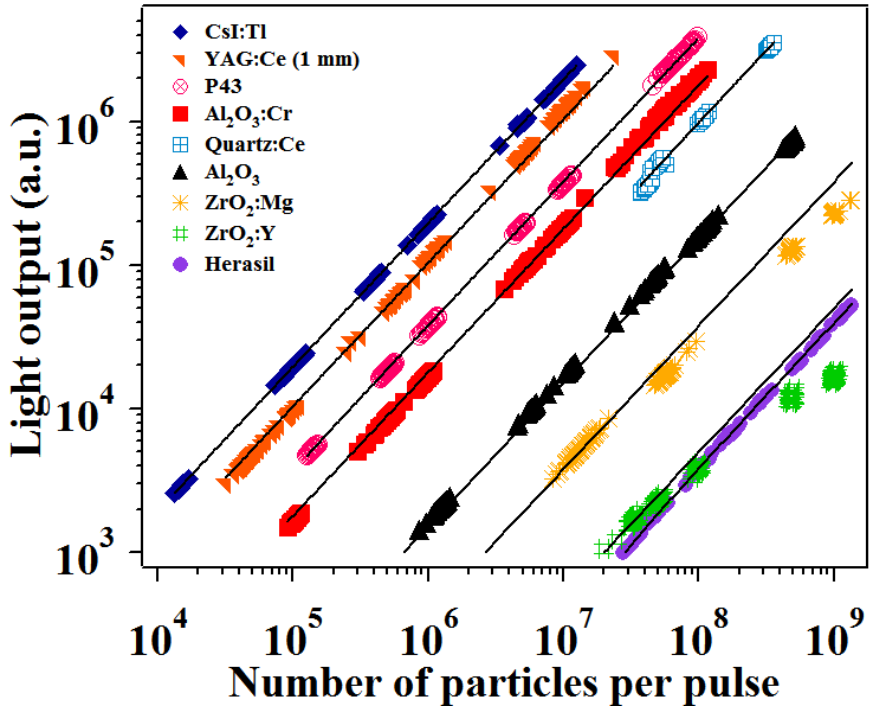


Figure 5.16: Light output from several scintillation screens. Beam parameters: Uranium at 269 MeV/u, 0.3 s pulse length and 0.25 Hz repetition rate.

- The smallest image width recorded from the glass materials was considered as underestimated image width in [65].

- The statistical moments calculated from the vertical projection are presented from Figure A 15 to Figure A 18.

Among the investigated materials, the light output obtained from Herasil and Quartz:Ce was linear with particle intensity. Due to stable light output, a stable behaviour in image reproduction was also expected from these samples. However, the image width σ increased over particle intensity on irradiation. A detailed analysis showed that this unstable behaviour was due to the beam fluctuation during the measurement. The unstable beam conditions contributed to increased σ values. In Herasil, a maximum difference of 0.45 mm σ was noticed between $2\times10^7$ ppp and $1\times10^9$ ppp and in Quartz:Ce, a maximum difference of 0.46 mm σ was noticed between $3\times10^7$ ppp and $3\times10^8$ ppp.

Compared to other materials, Herasil and Quartz:Ce glass sample recorded the smallest image width. This behaviour was considered as underestimation of the ion beam [58]. Moreover the Herasil sample produced the lowest light output compared to other materials even with the heavy ion Uranium irradiation. Due to the low light output and underestimation of beam width, these glass samples were excluded from further investigations.

In $ZrO_2$:Y and $ZrO_2$:Mg, the light output deviated from linear behaviour and the image width σ values increased with particle intensity due to the absorption of light within the ceramic

material. This unstable image reproduction and nonlinear light output behaviour was recorded also during the preliminary experiment where the samples were irradiated with Uranium ions (Figure A 1 and Figure A 2) and the image capturing was carried out with maximum camera gain settings. In the preliminary experiment, due to the light absorption within the materials, the light output was reduced and the image width σ increased at higher particle intensities (Figure A 1 and Figure A 2).

But in the linearity measurement (Figure 5.16) in addition to light absorption within the material, the unstable beam conditions has also contributed to image broadening in $ZrO_2$:Y and $ZrO_2$:Mg samples. Thus due to these two factors, the image profile obtained from these screens became distorted and deviated from the Gaussian distribution. At higher particle intensities, larger errors were obtained during curve fitting which clearly exhibits the deviation of the profiles from Gaussian shape.

In $ZrO_2$:Y, the image width σ obtained increased with particle intensity due to unstable beam condition and light absorption, see Figure 5.17. However, at $10^9$ ppp, smaller σ values compared to $5\times10^8$ ppp were obtained. To understand this behaviour the profiles obtained at various particle intensities was compared (Figure 5.19). At $5\times10^8$ ppp, broad profiles with large shoulders were obtained compared to the profiles obtained at $3\times10^7$ ppp. But at $10^9$ ppp, the profile becomes narrow with broad shoulders compared to the profiles at lower intensities ($3\times10^7$ and $5\times10^8$ ppp). This resulted in smaller σ values with larger errors bars, exhibiting that the profiles deviated from Gaussian distribution. Due to the absorption of light within the materials and intensity dependent behaviour, the Y and Mg doped $ZrO_2$ samples were excluded from further profile measurements.

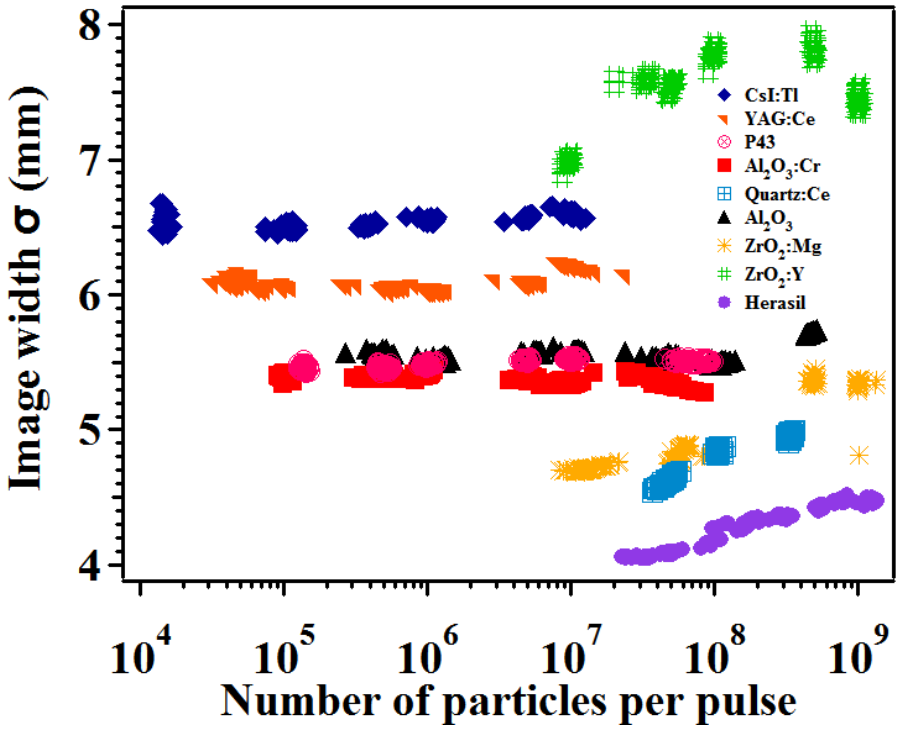


Figure 5.17: Image width σ calculated using Gaussian fits (algorithm 4, Chapter 4.5) from different scintillation screens for Uranium ion beams.

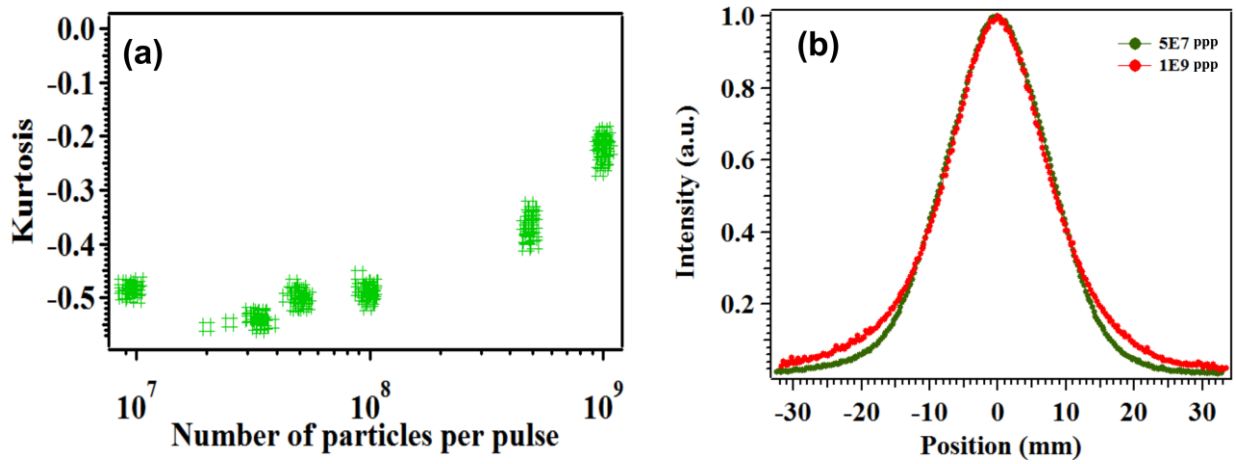


Figure 5.18: (a) Kurtosis calculated from $ZrO_2$:Y using the reduced intensity algorithm for Uranium ion beam. The image width obtained increases with particle numbers. The development of kurtosis towards positive value is an indication of a strong absorption of light within the ceramic material. (b) The image profile obtained from $ZrO_2$:Y screen at various particle intensities. The broader image profile at higher particle intensity contributed to large σ values.

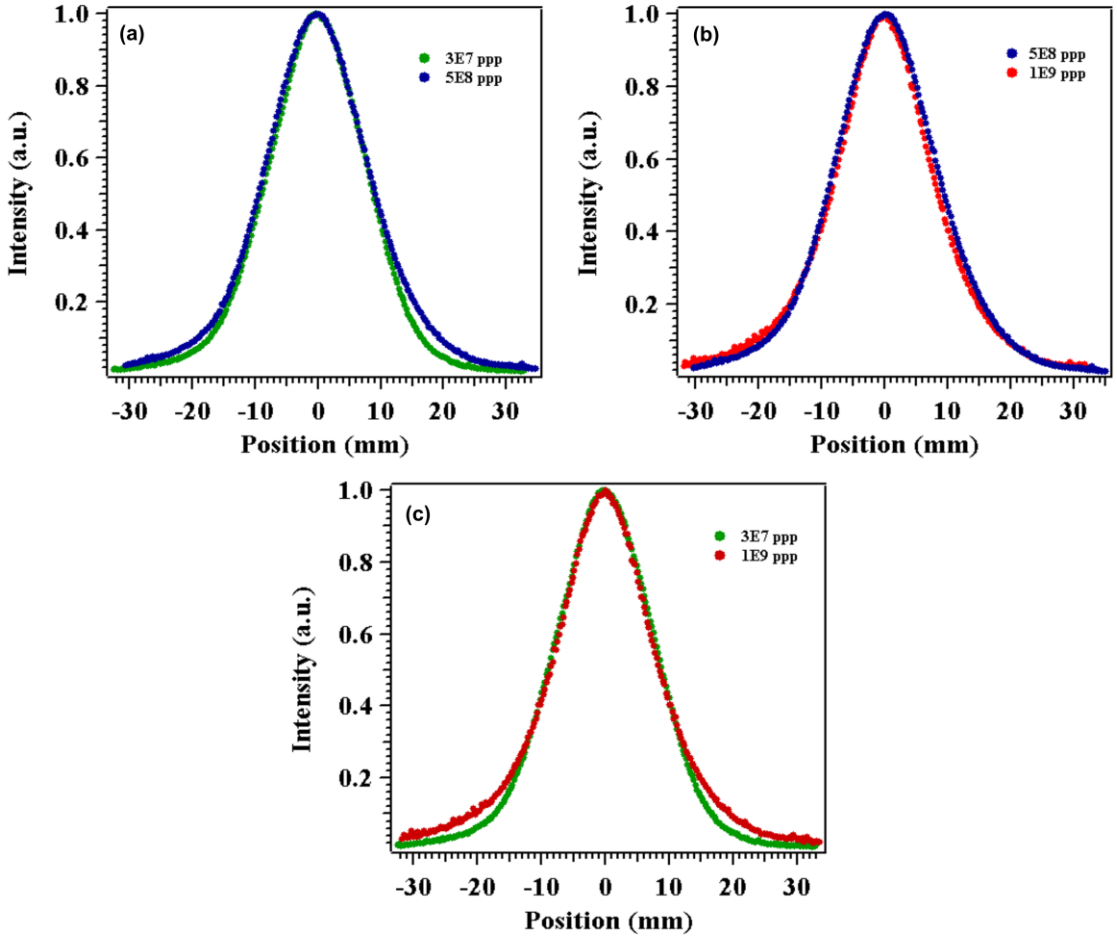


Figure 5.19: Image profiles obtained from $ZrO_2$:Y at various particle intensities. (a) The profile obtained for $5\times10^8$ ppp were broader than profiles obtained for $3\times10^7$ ppp. (b) and (c) The narrowed, broad shouldered image profile obtained for $10^9$ ppp compared to profiles from $3\times10^7$ and $5\times10^8$ ppp.

### 5.1.6 Results from Tantalum ions

To understand the linear behaviour of the screens over the complete dynamic range available in the experimental area, the data acquisition process was carried out using two cameras (chapter 4.3.5). The accelerated Tantalum ion beam reaches the targets with maximum kinetic energy of 275 MeV/u. The measurement was started with $10^4$ ppp and further progressed up to the maximum available beam intensity. While measuring the YAG:Ce (1 mm) screens the first camera got saturated at $10^7$ ppp. Therefore, further higher intensity measurements were carried out using the second camera equipped with 5 % grey filter.

A remarkable linear light intensity over 5 orders of magnitude of particle intensity was recorded for all the materials (Figure 5.20). The ordering in light output was similar as in previous measurements. The results obtained from Tantalum measurements confirm again the linear behaviour of the investigated scintillation screens over increasing particle intensity. The stable reproduction behaviour of the screen was recorded for more than 300 beam pulses (Figure 5.21). The image width σ calculated from the vertical plane is presented in Figure A 19 and Figure A 20.

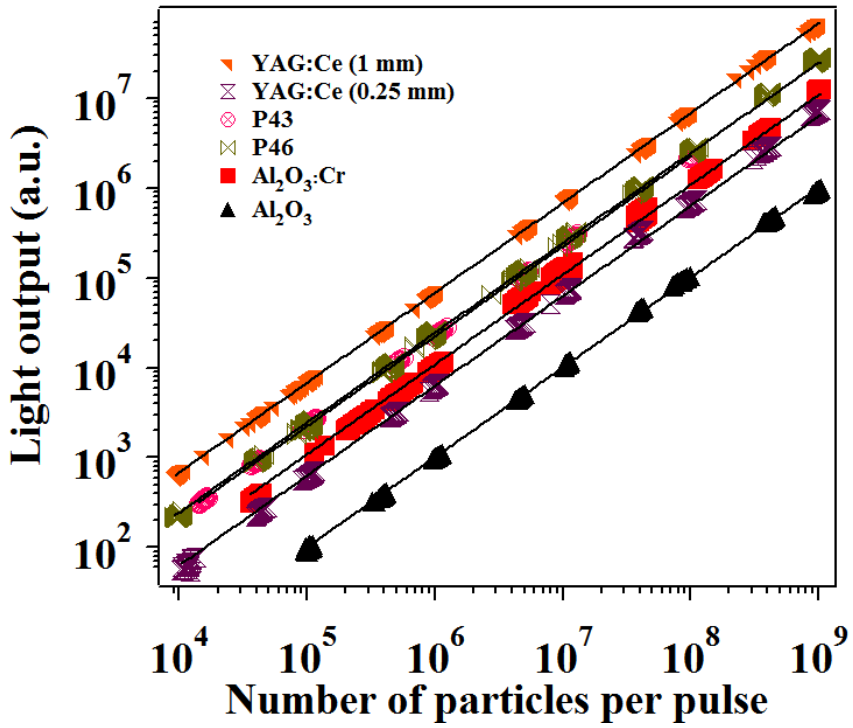


Figure 5.20: Light output from various scintillation screens vs. particle intensity. Beam parameters: Tantalum at 275 MeV/u, 0.3 s pulse length and 0.25 Hz repetition rate. A linear light output over 5 orders of particle intensity was measured.

### 5.1.7 Comparison with reference detector

Different image width readings were observed from the investigated materials. The standard scintillation screens CsI:Tl and YAG:Ce (1 mm) and (0.25 mm) also produced different image widths. The image width obtained from YAG:Ce (1 mm) and the other samples shows a

difference up to 16 %. In order to find the real width of the ion beam, the profiles reproduced by the scintillation screens were compared to the reference detector MWPC, see (Figure 5.22).

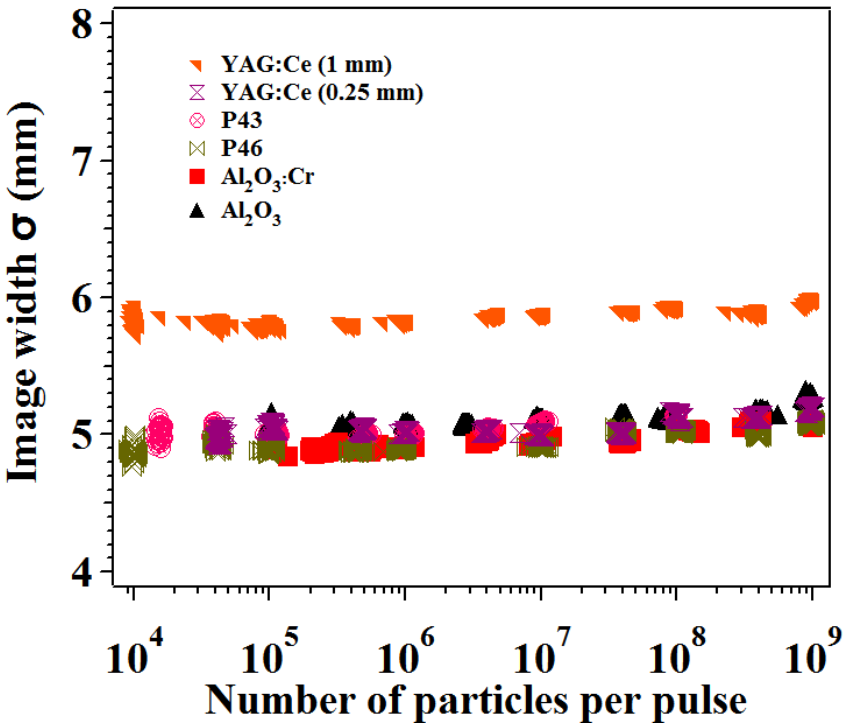


Figure 5.21: Image width σ calculated using Gaussian fit (algorithm 4, Chapter 4.5) for different scintillation screens. Beam parameters were the same as in Figure 5.20.

$Al_2O_3$:Cr was chosen to compare with MWPC since the profile obtained from $Al_2O_3$:Cr matches well with other materials such as P43, P46, $Al_2O_3$ and YAG:Ce (0.25 mm) (Figure 5.11). The image profiles obtained from $Al_2O_3$:Cr and YAG:Ce (1 mm) at different particle intensities were compared with the profiles from MWPC. The profiles from $Al_2O_3$:Cr screen matches well with the MWPC, whereas the profile obtained from YAG:Ce (1 mm) does not match with the MWPC measurements. Due to the process of light absorption and multi photon interaction, broad image profiles were obtained from YAG:Ce (1 mm) samples. The comparison of the profiles at higher particle intensity was restricted due to the saturation of the MWPC.

### 5.1.8 Relative and absolute comparisons

A detailed analysis was performed by comparing the relative and absolute light outputs obtained from various scintillation screens. The scale for all the light output plots coincides within 10 % error range. The energy loss within the material and the relative light output with respect to YAG:Ce (1 mm) were calculated and compiled in Table 5:1. The light output from $Al_2O_3$:Cr was always a factor of 10 higher than the one of $Al_2O_3$. This factor remains constant for every ion species.

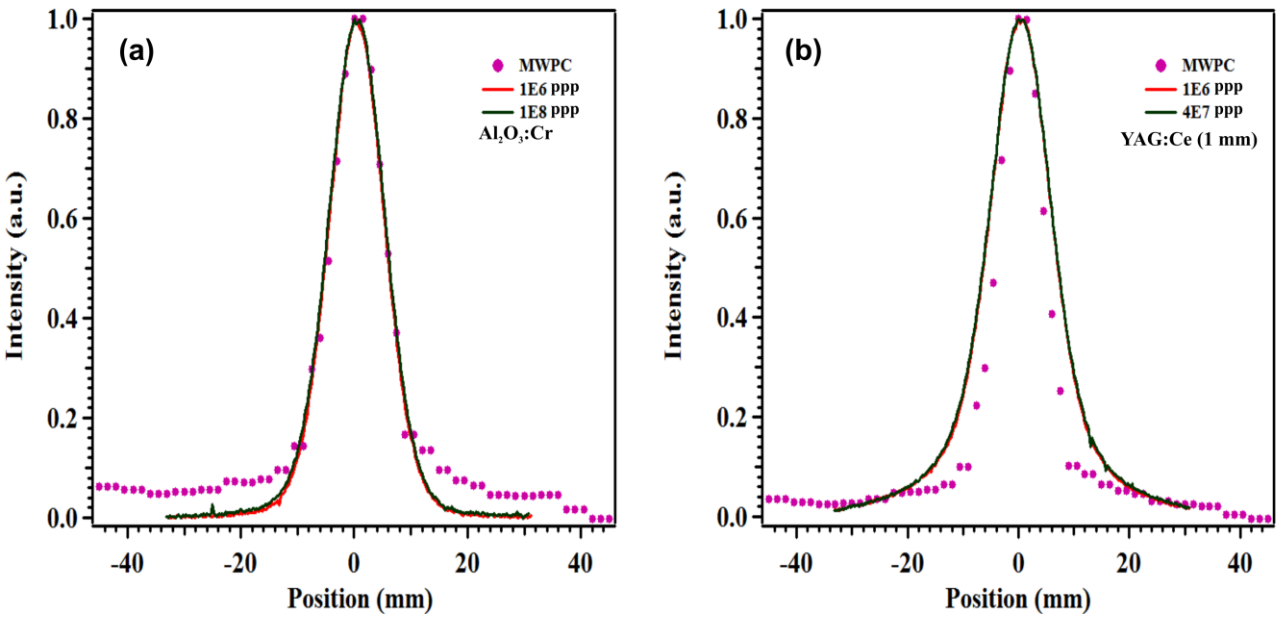


Figure 5.22: Comparison of Tantalum ion beam image profiles obtained from (a) $Al_2O_3$:Cr, (b) YAG:Ce (1 mm) at different particle intensities with the reference detector MWPC.

Table 5:1 Compilation of the relative light output from different scintillation materials and total energy deposited by a single ion in the materials

| Sample | Thickness (mm) | Carbon | | Neon | | Tantalum | | Uranium | |
|---|---|---|---|---|---|---|---|---|---|
| | | ΔE (GeV) | $Y_{rel}$ (%) | ΔE (GeV) | $Y_{rel}$ (%) | ΔE (GeV) | $Y_{rel}$ (%) | ΔE (GeV) | $Y_{rel}$ (%) |
| YAG:Ce | 1.0 | 0.044 | 100 | 0.119 | 100 | 6.5 | 100 | 10.5 | 100 |
| YAG:Ce | 0.25 | - | - | 0.029 | 10 | 1.605 | 9.6 | - | - |
| P43 | 0.05 | 0.0026 | 40 | 0.0079 | 50 | 0.405 | 33 | 0.67 | 34 |
| P46 | 0.1 | - | - | 0.0125 | 40 | 0.634 | 35 | - | - |
| $Al_2O_3$:Cr | 0.8 | 0.032 | 17 | 0.09 | 21 | 4.95 | 15 | 7.9 | 15 |
| $Al_2O_3$ | 0.8 | 0.032 | 1.7 | 0.09 | 2.2 | 4.95 | 1.4 | 7.9 | 1.5 |

**ΔE:** Total energy deposited by a single ion in the material.
**$Y_{rel}$ (%):** Relative light output calculated from different scintillation materials with respect to YAG:Ce (1 mm) screen.

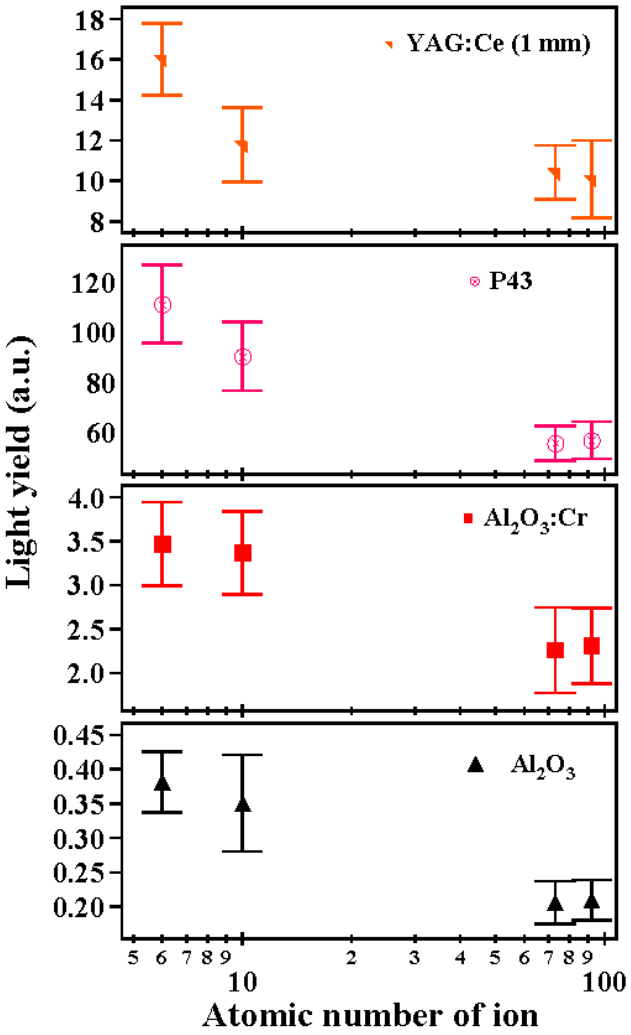


Figure 5.23: The light yield per energy deposition by a single ion calculated for different ion beams. For the same energy deposition the sample produces different light yield.

The absolute light yield from each sample was calculated by normalising the energy deposited in the materials. The light output obtained for different particle intensities were normalised to a single particle (light output/particle). The obtained value was further normalised to 1 MeV of energy deposition in the materials (light output/particle/1 MeV energy deposition), and this value is the absolute light yield for 1 MeV of energy deposited. The standard deviation values obtained during the normalisation of light output to the particle intensity were given as error bars. The absolute light yield obtained for different ions is shown in Figure 5.23.

The results clearly state that the light output from the materials depends on the ion beam used for irradiation. In general, a higher light yield was recorded for lighter ions than for heavy ions for same energy deposition. A difference up to 50 % was observed from P43 screens for Carbon and Uranium ion beams, showing a non-proportional behaviour as found for nuclear particles, see [89-90]. A similar behaviour was found also for other samples. This non-proportional behaviour was considered as the intrinsic property of the ionization density in material by Gwin and Murray [99]. In later years more models were proposed which suggest that the non-proportional behaviour was due to destruction of excitons through excitons collision [100] and non-radiative decay of e-h pair through ionization quenching effect [101] as mentioned in Chapter 3.4.9.

## 5.2 Performance concerning possible irradiation damage

In daily accelerator operation the screens are continuously irradiated with different ions at different particle intensities. Therefore, apart from the linearity measurements described in chapter 5.1, the radiation stability of the scintillation screens has to be studied. Hence stability measurements were carried out using the heavy ion Uranium at higher particle intensity. Among the investigated materials a stable performance was noticed from P43, P46, $Al_2O_3$:Cr and $Al_2O_3$ screens (chapter 5.1). These screens were irradiated with 250 and 1000 pulses of

300 MeV/u Uranium ion beam with $6\times10^8$ ppp. To understand the behaviour at high energy deposition the measurement was performed also with Uranium at 200 MeV/u of kinetic energy. The typical energy loss in the materials at different kinetic energies is presented in Table 5:2.

Table 5:2: Calculated energy loss in materials by a single ion and electronic energy loss for two different energies (200 and 300 MeV/u of initial kinetic energy) of Uranium ions.

| Sample | Thickness (mm) | Energy loss (MeV/u) by single ion at 269 MeV/u | Electronic energy loss (dE/dx) at 269 MeV/u (keV/nm) | Energy loss (MeV/u) by single ion at 162 MeV/u | Electronic energy loss (dE/dx) at 162 MeV/u (keV/nm) |
|---|---|---|---|---|---|
| P43 | 0.05 | 2.73 | 12.96 | 3.57 | 16.94 |
| P46 | 0.1 | 4.25 | 10.05 | 5.63 | 13.23 |
| $Al_2O_3$:Cr | 0.8 | 33.06 | 9.53 | 46.8 | 12.58 |
| $Al_2O_3$ | 0.8 | 33.06 | 9.53 | 46.8 | 12.58 |

### 5.2.1 Low energy ion beam measurements

To investigate the stability with low energy ion beams (high energy deposition), the thick ceramic screens $Al_2O_3$:Cr and $Al_2O_3$ were irradiated with 500 pulses of Uranium accelerated to 200 MeV/u. The screens were irradiated with a beam intensity of $4\times10^8$ ppp at 0.25 Hz repetition rate. In addition to these two screens, two non-irradiated $Al_2O_3$ and $Al_2O_3$:Cr screens were used as a reference. The reference screens were irradiated with few pulses at the beginning and end of the measurement to estimate the beam fluctuation. These reference screens also help to understand the effects induced by light absorption.

The results obtained show a constant light output from both the screens (Figure 5.24) even at higher energy deposition. The difference in light output between the screens remains constant similar to previous linearity measurements. From the image reproduction measurement, a difference in σ up to 8 % was recorded between the doped and undoped $Al_2O_3$ screens due to slight change in beam alignment during the break between the measurements. However within one single measurement, a stable behaviour was noticed from the 1$^{st}$ pulse to the 500$^{th}$ pulse of the measurement. The measurements from the heavily irradiated screen coincide with the image width recorded from the reference screens.

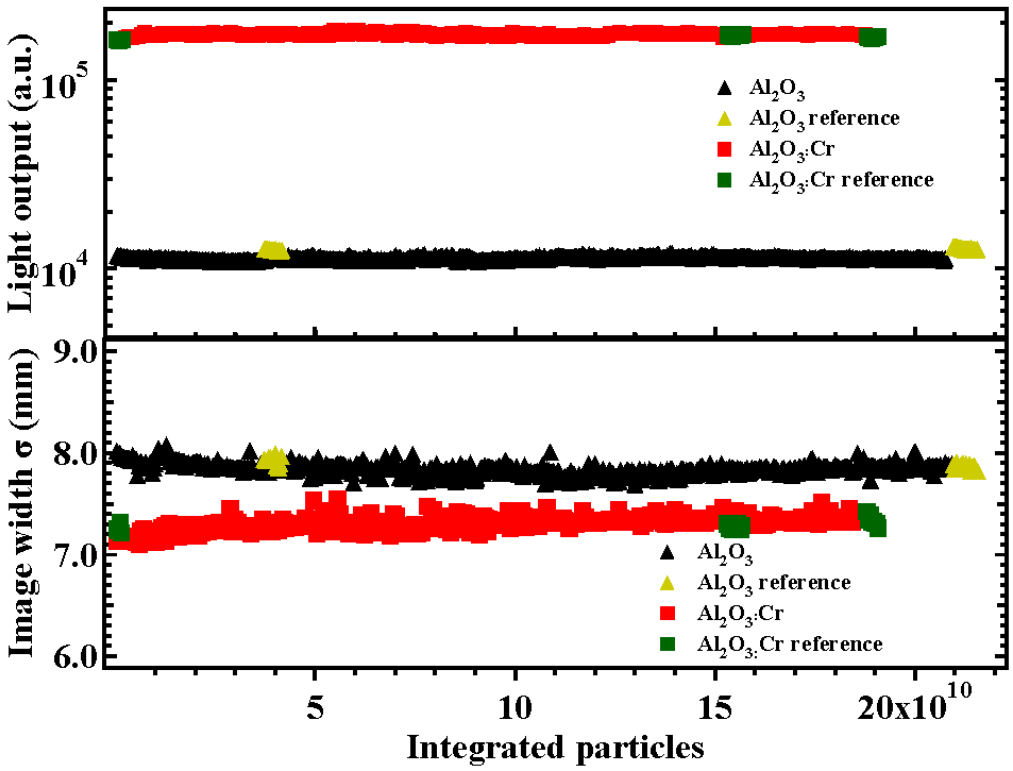


Figure 5.24: Light output and image width obtained from aluminium oxide scintillators. Beam parameters: Uranium at 200 MeV/u, 500 beam pulses, 4 $\times 10^8$ ppp and 0.25 Hz repetition rate.

### 5.2.2 Measurements with moderate beam energy

Along with aluminium oxide samples the powder screens P43 and P46 were irradiated with Uranium ions accelerated to 300 MeV/u. Here, the P46 sample was chosen since it is more sensitive to ionization radiation than YAG:Ce (0.25 mm). To study the properties of the scintillation screens at extreme radiation conditions, the screens were irradiated with a higher number of Uranium beam pulses. The four selected screens were irradiated with 1000 pulses of Uranium at $6\times10^8$ ppp. Two grey filters (12.5 %+ 25 %) with final transmission of 3.125 % were installed to avoid the CCD saturation.

Among the investigated samples a very stable, long standing behaviour and a constant light output were obtained from the oxide ceramics, especially from $Al_2O_3$:Cr (Figure 5.25). The light output, image width and the higher statistical moments were stable for more than 1000 beam pulses. The difference in light output measured between the first and last pulse was around 2 % and the image width increased only by 0.7 % which is in acceptable range. Moreover no significant difference in the physical appearance of the sample was noticed.

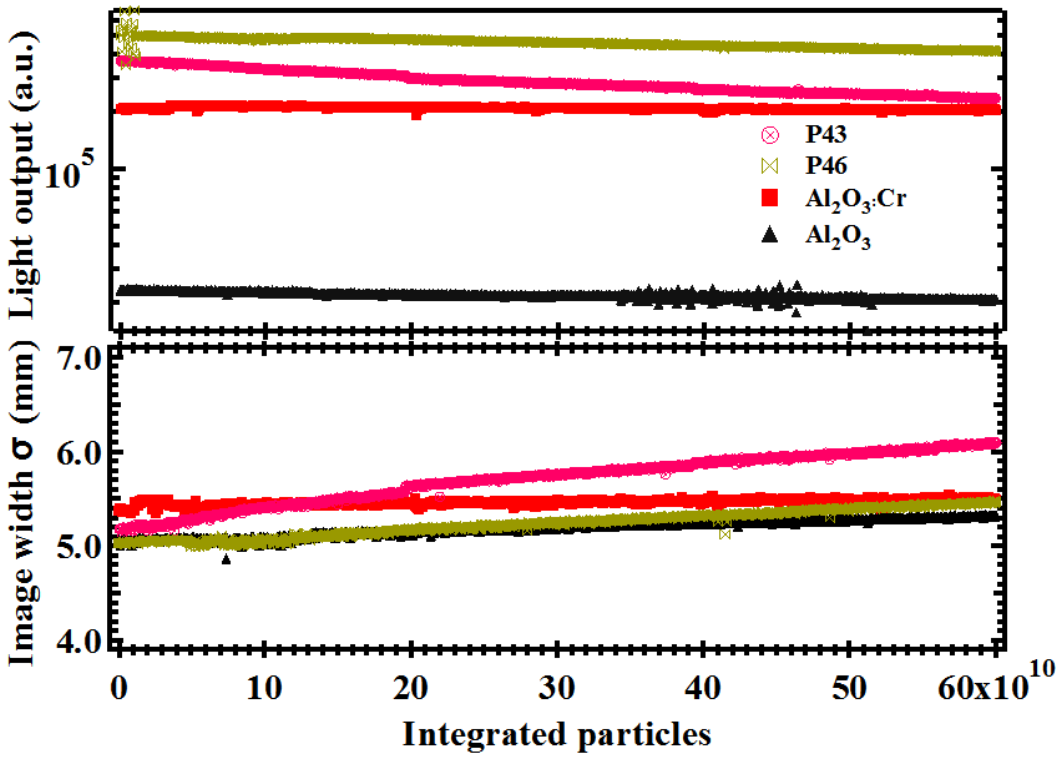


Figure 5.25: Light output and image width calculated from selected scintillation screens. Beam parameters: U at 300 MeV/u, $6\times10^8$ ppp at 0. 25 Hz repetition rate, 1000 beam pulses.

Pure $Al_2O_3$ screen shows a slight variation in the light output and image width in comparison to $Al_2O_3$ :Cr. A decrease in light output up to 11 % and 5 % image broadening was recorded for $Al_2O_3$. The image profiles were further characterised by calculating the higher statistical moments skewness and kurtosis (Figure 5.26). The skewness shows that profiles were almost symmetrically distributed over its center. The change in kurtosis towards more negative values (Figure 5.26) indicates that the light output gets saturated with irradiation in P43, P46 and $Al_2O_3$. After irradiation, the color of $Al_2O_3$ sample turned to yellow from pale white indicating the formation of color centers. No change in color was observed for the other two powder screens P43 and P46.

A maximum of 44 % decrease in light output was measured from the P43 screen. The saturation effect in light output leads to a significant profile broadening up to 16 %. In case of P46 screen 20 % decrease in light output leads to 8.5 % increased image widths. To understand this unstable behaviour, the average dose deposited over the thickness of the sample was calculated. A maximum dose of 1.980 kGy was deposited in the P46 powder screen by a single pulse ($6\times10^8$) in ±1 σ area. The dose deposited in other samples such as $Al_2O_3$:Cr and P43 was 1.700 kGy and 1.500 kGy, respectively. The total dose deposited in each screen at the end of the measurement was a factor 1000 more than these values. These high radiation doses induced excitation quenching and saturation of luminescent centers in the samples. Similar effects have been reported in the literature [19-20].

In the powder screens, a high dose was deposited in a small volume since the thickness of the active layers was in the micrometers range (P43: 50 $\mu$m and P46: 100 $\mu$m thick). However, normalisation of the results shows that the highest radiation was experienced by the P43

screen which was 2 orders of magnitude higher than the one of aluminium oxide ceramics. Hence such a high radiation deposition induced an unstable behaviour in the P43 screen. Since the temperature rise in the sample was negligible, there was no thermal quenching possible.

The profiles obtained from these screens at various pulse numbers are plotted in Figure 5.27. Since only an increase of 1.3 % in image width was noticed from Chromox screen, the projections obtained were indistinguishable. In other samples, the image broadening was clearly visible, particularly for P43 screen (Figure 5.28)

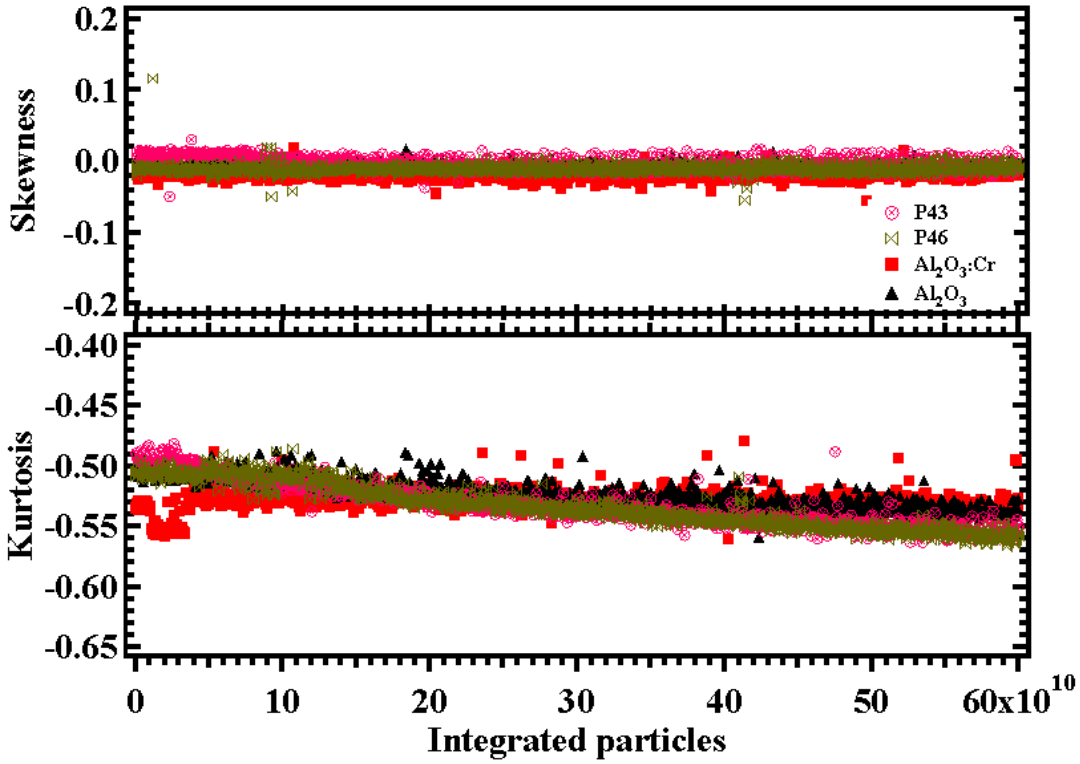


Figure 5.26: Statistical moments calculated for the selected scintillation screens. Beam parameters: U at 300 MeV/u, $6\times10^8$ ppp at 0. 25 Hz repetition rate, 1000 beam pulses.

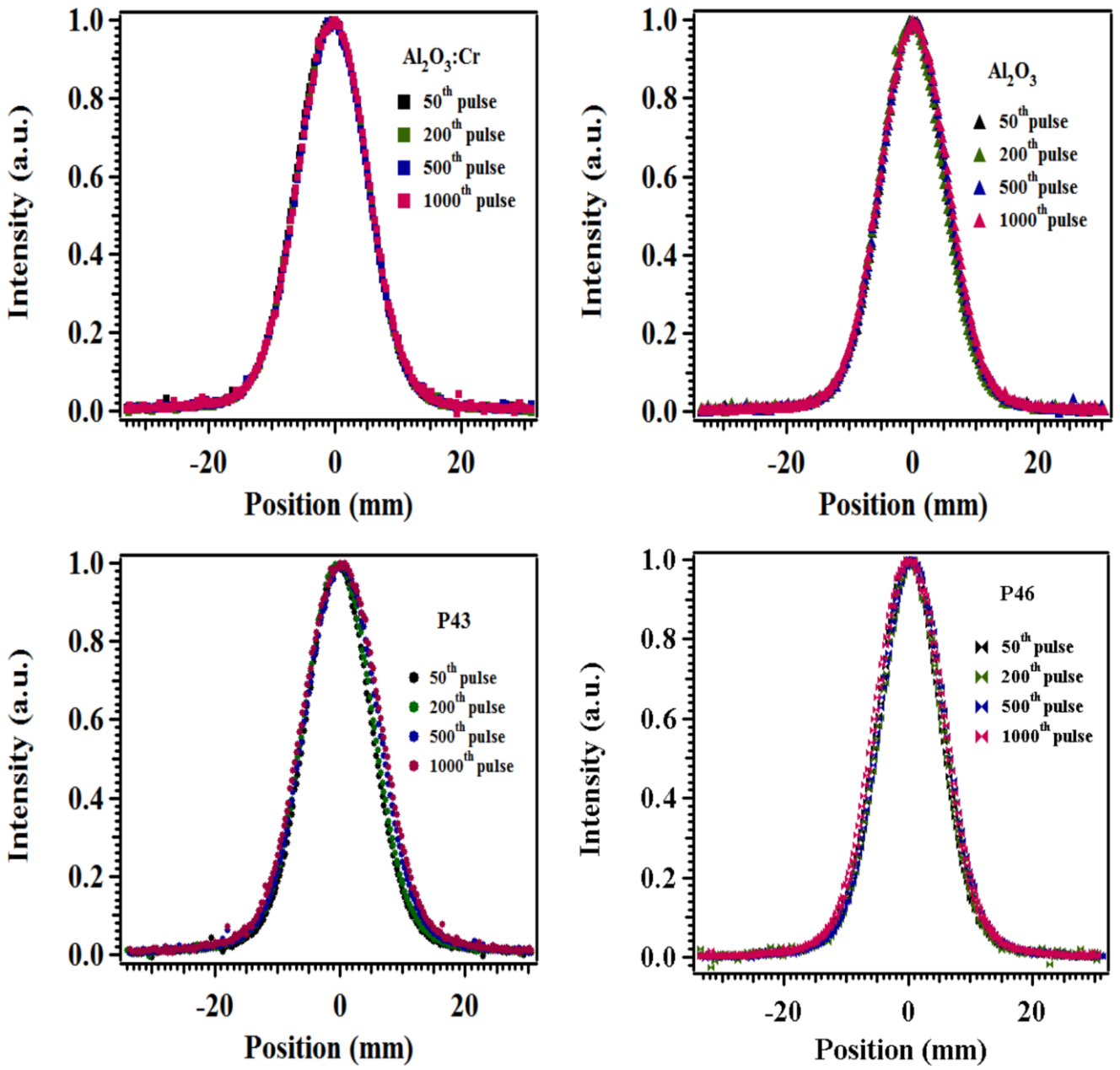


Figure 5.27: Image profiles obtained from the screens at various pulse numbers. Beam parameters are the same as in Figure 5.25.

The image profiles obtained from $Al_2O_3$:Cr screens remain constant and no significant change was observed. In other samples, the saturation effect leading to image broadening was clearly seen from the image profiles. The unsymmetrical broadening of the image width indicates that the ion beam was also not stable during the measurement. The results suggest that the saturation effect and beam fluctuation are responsible for the image broadening in P43 screens.

### 5.2.3 Stability under reduced intensity

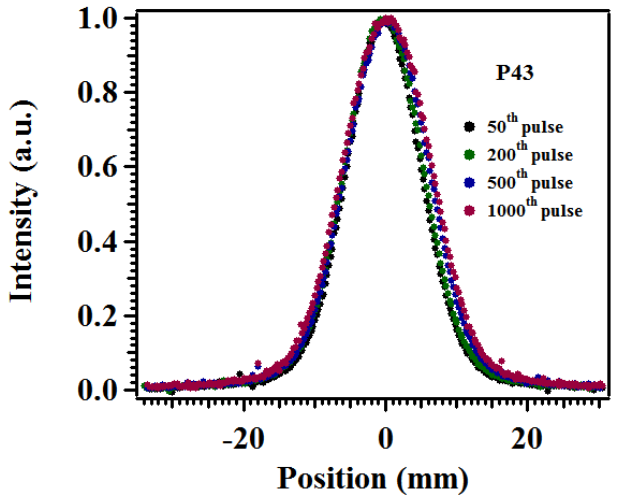


Figure 5.28: Image profiles obtained from P43 screen at different beam pulses. The profile broadening was clearly seen on the right side of the profile.

During irradiation with $6\times10^8$ ppp of Uranium ions, an unstable behaviour was experienced from the screens except for $Al_2O_3$:Cr. Therefore, further measurements were continued with reduced particle intensity after 24 hours of the previous measurement. The intensity of the ion beam was in the range of $4\times10^8$ ppp. In comparison to the previous measurement, the transmission of the lens system was reduced in order to have maximum opening of the iris. The camera was fixed with two grey filters each with transmission of 12.5 % resulting in total transmission of 1.5 %. Each screen was irradiated with 250 beam pulses and the statistical moments were calculated. The total fluence applied to each screen was $13\times10^{10}$ particles.

The image width calculated from these screens show stable image reproduction behaviour over the measurements (Figure 5.29).

In the previous linearity measurements (chapter 5.1), the image widths obtained from these materials show only ±4 % difference. However, during the stability measurements, different image widths were recorded from the above mentioned four materials. This was due to the interval between the measurements. Due to different beam alignments, these samples register different image widths. But the result obtained from each screen remains constant from the 1st to the last beam pulse. The maximum difference obtained between the 1st and 250th pulse was 0.6 % from P43 and $Al_2O_3$ screens. The calculated higher statistical moments, skewness and kurtosis show that the delivered beam was not the same for all the samples. However, for each screen a constant behaviour was noticed over 250 beam pulses. The profiles obtained from the screens at different pulses are plotted in Figure 5.30. The projection obtained from aluminium oxide samples resembles almost a normal distribution. A close observation of the profiles obtained reveals that the P43 and P46 screens have slightly skewed distributions, P43 towards negative direction and P46 towards positive direction.

In this measurement, no considerable saturation effects in light output were noticed from the screens (Figure 5.25). After 24 hours, the samples are recovered from the unstable light output and image reproduction behaviour. This indicates that the instability in the previous measurement was due to temporary excitation quenching effects in the materials.

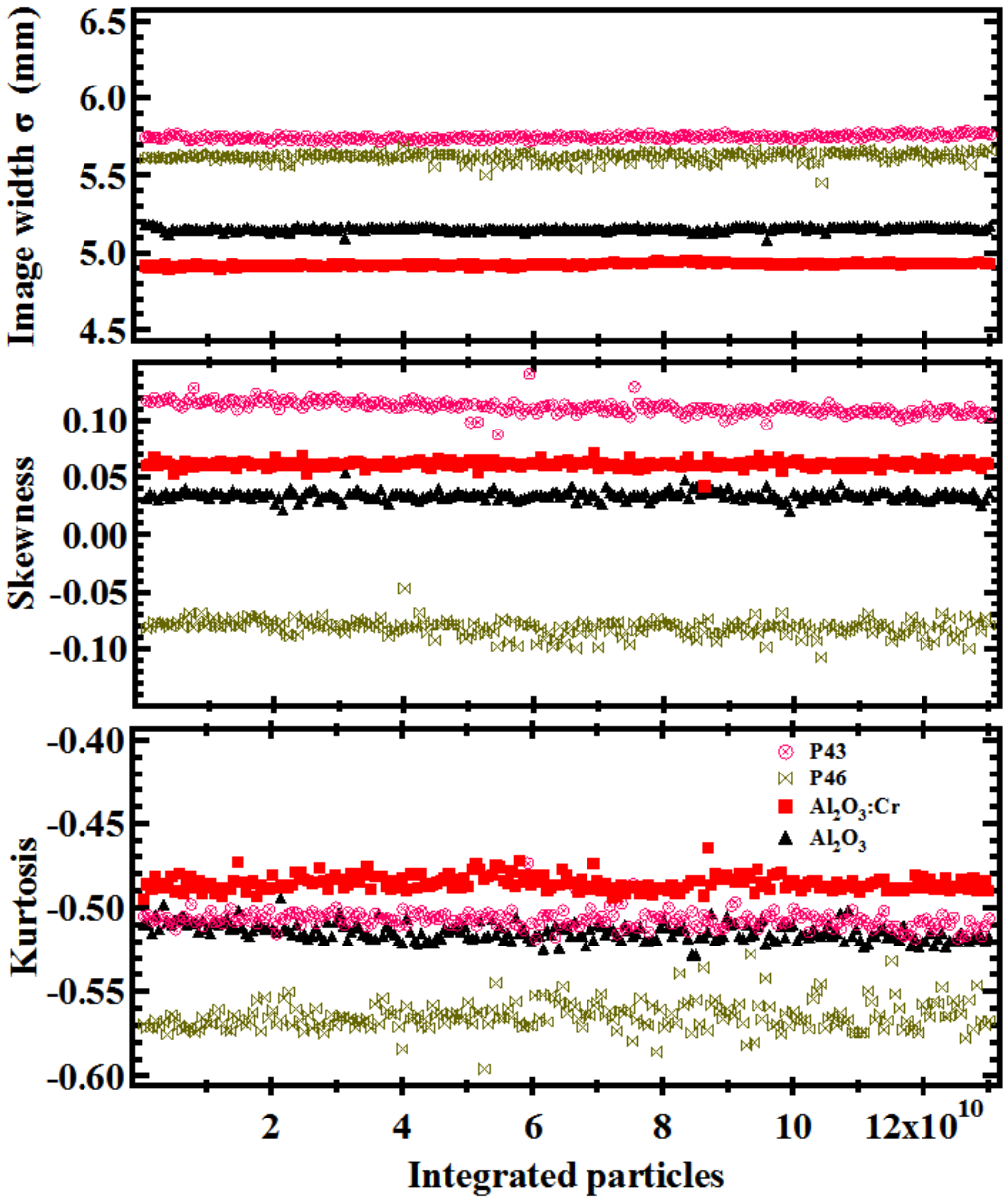


Figure 5.29: The statistical moments calculated for different screens for 300 MeV/u Uranium ion beams. The screens were irradiated with 250 beam pulses at 0.25 Hz repetition rate.

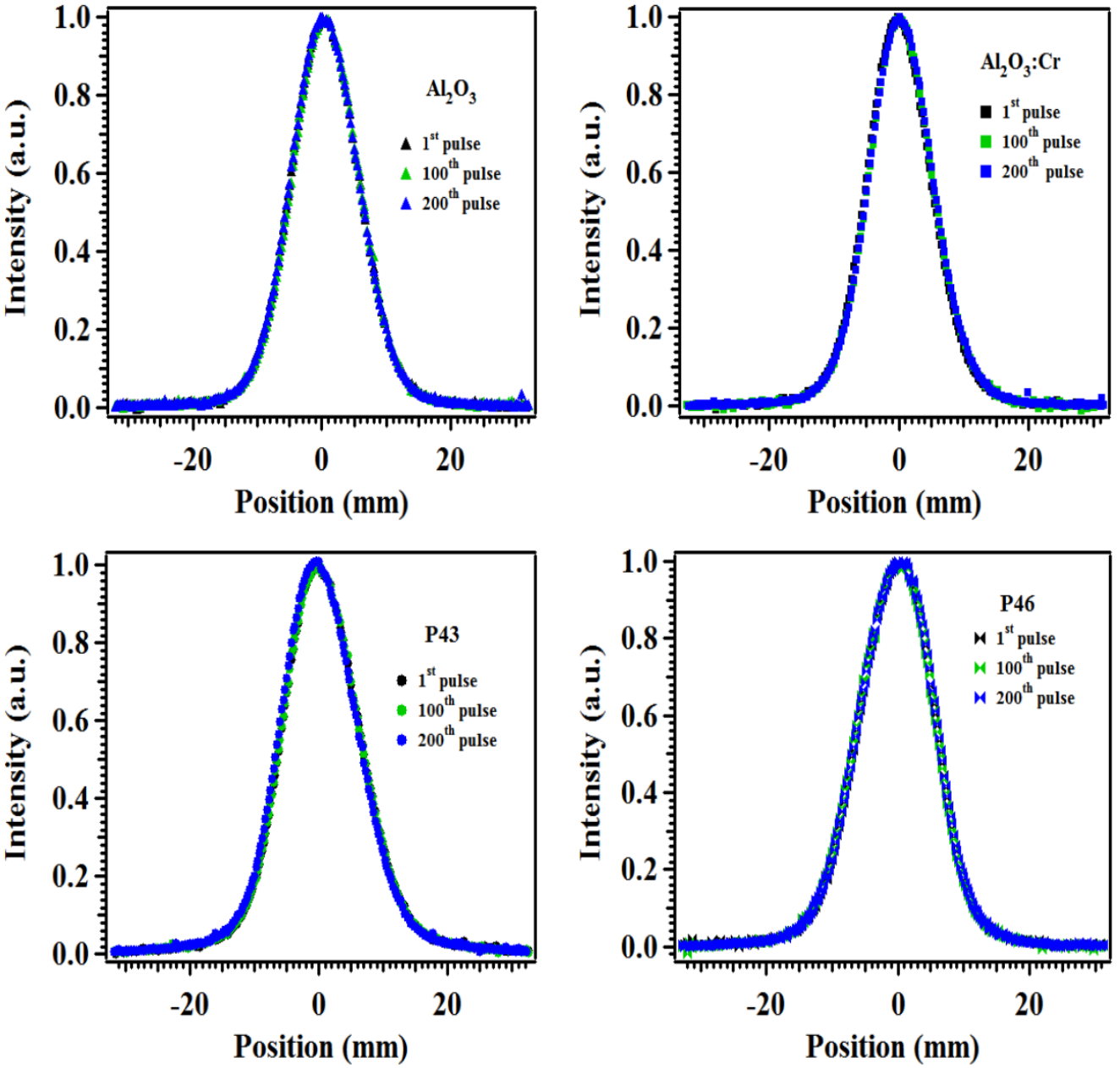


Figure 5.30: Image profiles obtained from scintillation screens at different pulse numbers. The shape of the beam profiles remain the same for the 1st, 100th and 200th beam pulse.

## 5.3 Radiation modification analysis

An important factor to be analysed while investigating the scintillation screen is the effect of swift heavy ions on the irradiated material. In general, heavy ion irradiation induces considerable changes in the materials such as phase transformation [102-107], amorphisation [108-113], displacement of atoms [114], stress accumulation [115] and formation of point defects and color centers [116-120]. Some of these radiation damages have influence on the luminescence properties of the materials. For example, the color centers formed during irradiation produce radiation induced absorption bands. These absorption bands reduce the light output from the materials by reducing the light attenuation length [116].

A small decrease in light output was noticed from P43, P46 and $Al_2O_3$ screens under continuous irradiation (Figure 5.25). These samples were analysed using Raman spectroscopy and X-ray diffraction for radiation induced structural modification and the color centers formation in $Al_2O_3$ and $ZrO_2$:Y was analysed by recording the UV-Vis absorption spectra.

### 5.3.1 Powder screens

Among the investigated samples, about 44 %, 20 % and 11 % decrease in light output was noticed from P43, P46 and $Al_2O_3$ screens after irradiating with 1000 pulses of Uranium ions with an intensity of $6\times10^8$ ppp. Apart from the color centers in $Al_2O_3$ and $ZrO_2$ samples no visible macroscopic damage was noticed in these samples.

To estimate the radiation induced damages, it is necessary to calculate the energy loss in the screen materials. Because of the high ion energy, the time for the interaction between the ion and the materials was very small and the energy loss obtained from the samples lies in the Bethe-Bloch regime. The electronic, nuclear energy loss and the projectile range of ions in these samples were calculated using SRIM [23] (given in Table 5:3).

Table 5:3: Electronic energy loss, nuclear energy loss and range of Uranium ions at 252 MeV/u.

| Sample | Electronic energy loss ( keV/nm) | Nuclear energy loss (keV/nm) | Projectile range (mm) |
|---|---|---|---|
| YAG:Ce | 10.39 | 0.0027 | 3.76 |
| P43 | 13.39 | 0.0035 | 2.96 |
| $Al_2O_3$ | 9.85 | 0.0026 | 3.94 |
| $ZrO_2$:Y | 12.08 | 0.0032 | 3.25 |

No considerable change was noticed in the Raman spectra obtained from the irradiated spot of P43 sample. The positions and the intensity of the peaks at 108, 195, 428 and 453 $cm^{-1}$ [121] remain the same as the spectra from unirradiated regions. No traces of new peaks, peak broadening or peak position shifting was noticed from the spectrum. Although the light output from the material decreased under irradiation, no considerable modification was found in the sample. This also confirms that the unstable behaviour of the screens under intense irradiation is a temporary phenomenon and not due to any irreversible structural radiation damage in the material. No significant change in the intensity and peak position was observed for P46 except

the increased fluorescence background in the irradiated region see Figure 5.32. Similar effects were also noticed for 0.25 mm and 1 mm YAG:Ce single crystals.

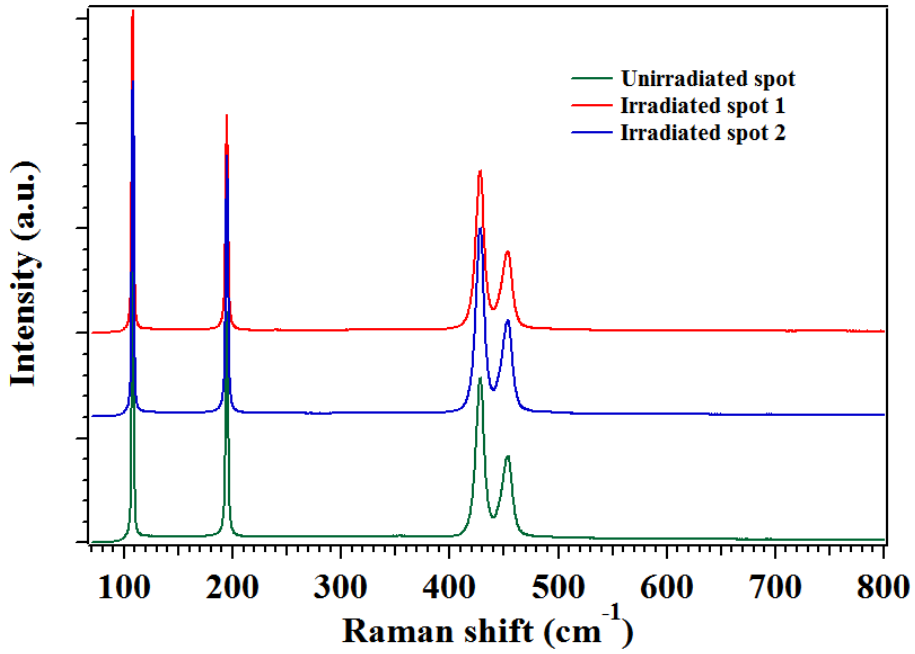


Figure 5.31: Raman spectra of P43 powder screen used for both linearity and stability measurements. No significant change in the peak positions, intensity and fluorescence background was noticed in the spectrum in the irradiated region.

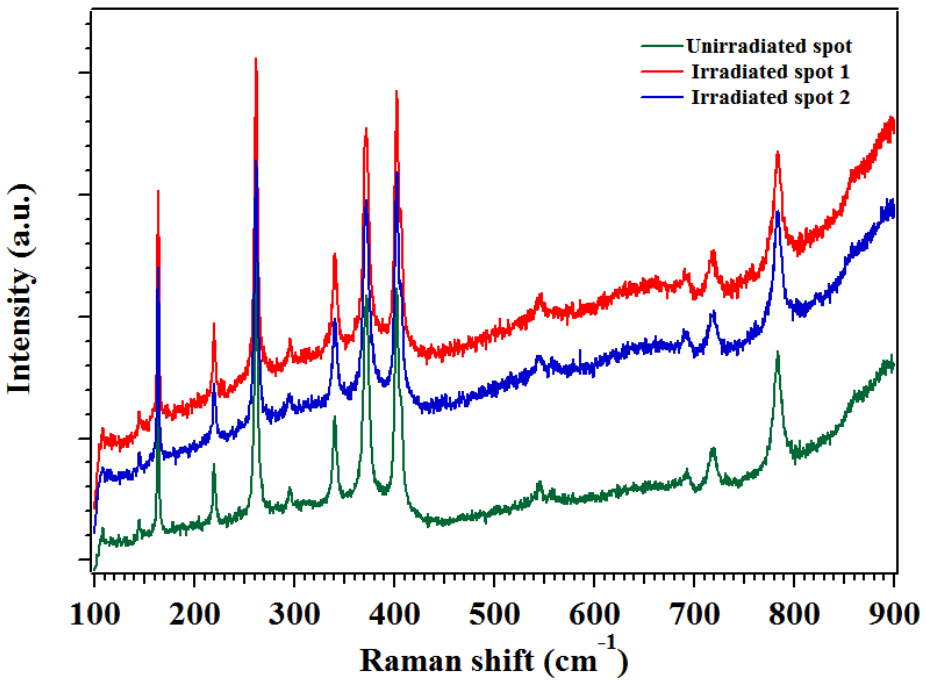


Figure 5.32: Raman spectra of P46 (YAG:Ce) powder screens. A strong fluorescence background was noticed in the spectrum in the irradiated region. The peak intensity and positions remain the same in measured spectra.

## 5.3.2 Ceramics samples

Among the materials used for the stability measurement, considerable change in the light output and image width reproduction was noticed from $Al_2O_3$. In addition, a visible change in the color of the samples took place upon irradiation (Figure 5.33). To analyse the radiation damage, Raman spectra were recorded at 5 positions over the diameter of the sample. Along with the $Al_2O_3$ sample used for the stability measurement, $Al_2O_3$ used for the linearity measurement was also analysed for radiation damage. During the profile measurement, the ion beam was always aligned to hit the center of the targets. In Raman spectra a strong fluorescence background was noticed, especially at the center of the sample. In Figure 5.33, the spectra of samples used in linearity measurements (top) and stability measurements (bottom) are exemplarily shown. The intensity of the fluorescence decreases as we move from the center to the edge of the sample (Figure 5.33).

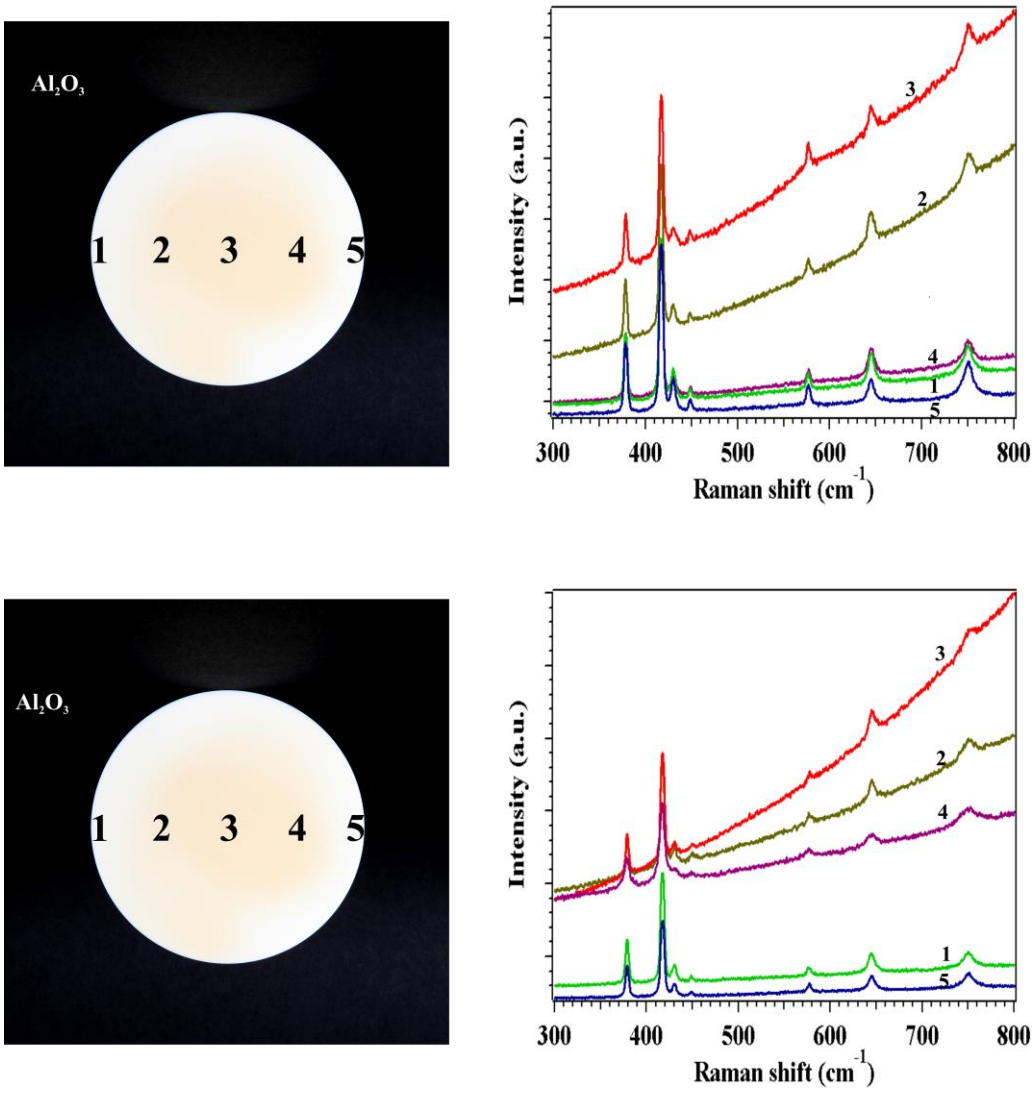


Figure 5.33: (Top) Raman spectra obtained from $Al_2O_3$ irradiated with Ne, Ar and Ta ions; (Bottom) $Al_2O_3$ irradiated with 1250 pulses of Uranium ions. The Raman spectra were recorded in 5 different positions over the diameter of the sample.

Due to strong fluorescence, the weak Raman peaks were not clearly visible in the sample irradiated with Uranium ions. Since the shape of the ion beam was almost Gaussian, 61 % of the particle intensity was within ±1 σ area. This area which has more particle fluence tends to show larger fluorescence background (red curves). The primary radiation damage induced by ionization radiation in the materials is the displacement of atoms with crystal defects (Frenkel defects) and interstitials. [114, 120, 122-124].

Apart from the appearance of the fluorescence background, no considerable change in the Raman spectra such as a shift of the peak position was noticed.

According to the literature, $Al_2O_3$ is a particularly radiation-hard material. N. Khalfaoui *et al*. [125] analysed $Al_2O_3$ by irradiating it with different ions between Ni and U with kinetic energies in the range from 1 to 11 MeV/u with electronic energy losses between 10 and 43 keV/nm and fluences up to $10^{13}$ $cm^{-2}$. For the experiments, scanning force microscopy, profilometry and channelling Rutherford backscattering were used in order to measure hillock formation, swelling and crystal lattice damage. The results showed that the mean electronic energy loss threshold value for damage creation of the mentioned kinds in $Al_2O_3$ was calculated as 9.5 ± 1.5 keV/nm. The authors state that the material suffers from serious radiation damage below ion beam energies of 80 MeV/u.

In the present case, the electronic energy loss in $Al_2O_3$ by 269 MeV/u Uranium ions calculated using SRIM 2008 was around 9.53 keV/nm which is just at the threshold. However, since the maximum number of particles used for irradiation (accumulated fluence $1.7\times10^{11}$ $cm^{-2}$) was below the range mentioned in [125], no considerable microstructural radiation damage was to be expected for $Al_2O_3$.

Fluorescence effects in oxides can be attributed to defects, interstitials, color centers [126] and surface contaminations [127]. In the present case of ion irradiation (without measurable microstructural damage), it is most likely that the color centers are the main reason for fluorescence.

In Raman spectra, the obtained fluorescence background decreased with laser exposure for 10 to 20 minutes (Figure 5.34). The process of exposing samples to the laser is called 'burn-out method' [127] or photo bleaching [128-129]. During this process, the color of the $Al_2O_3$ sample changed from yellow to pale white which is an indication of recovery from the color centers formed during irradiation. Even though the color centers formed were removed after 20 minutes of photo bleaching, a certain fluorescence background still remained in the spectra. The fluorescence effects were noticed also in $Al_2O_3$:Cr samples which do not have any color center formation. Therefore various other factors like Frenkel defects and impurities might be responsible for the fluorescence formation in $Al_2O_3$:Cr. In contrast, in Y and Mg doped $ZrO_2$, no significant changes and no fluorescence background were noticed in the Raman spectra obtained from the irradiated area.

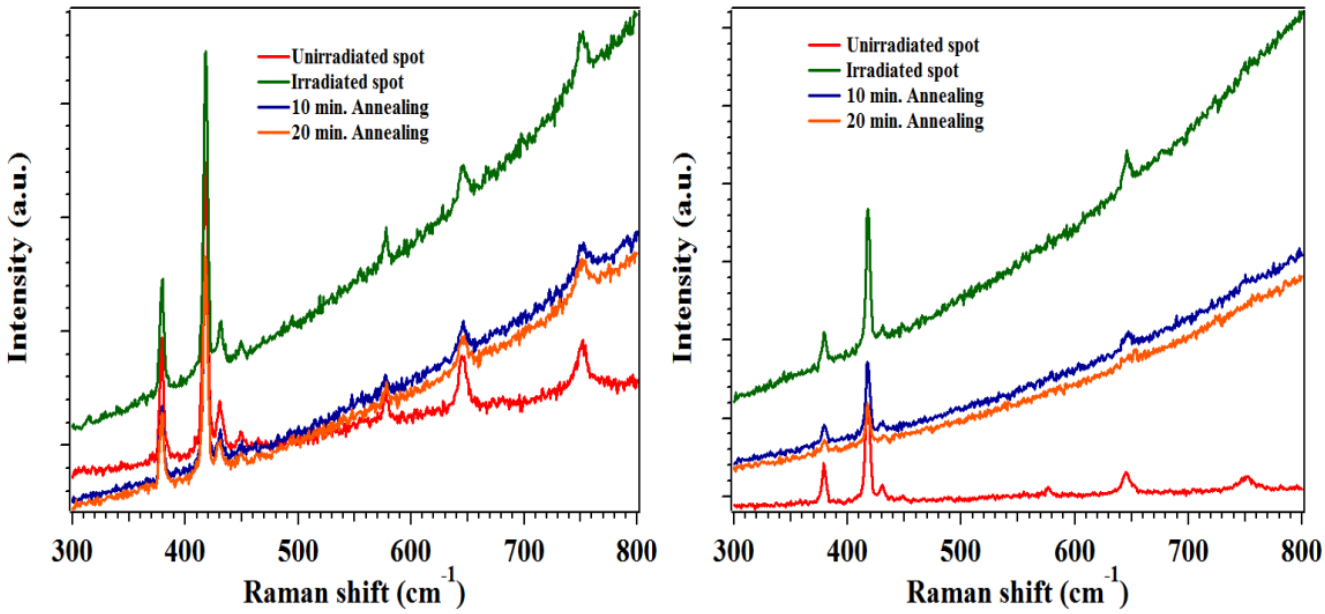


Figure 5.34: Raman spectra obtained from $Al_2O_3$ samples before and after exposing to laser; (left) irradiated with Ne, Ar and Ta ions; (Right) irradiated with Uranium ions. A strong decrease in the background was recorded after exposing the spot to a laser (473.5 nm) for 20 minutes.

### 5.3.3 X-ray Diffraction analysis

In addition to the Raman spectroscopy, the heavily irradiated ceramic samples $Al_2O_3$ and $Al_2O_3$:Cr were analysed for radiation induced structural modification using X-ray diffraction. After cutting the sample (~4 $cm^2$) using a diamond point, the diffraction pattern was recorded at two different positions (a) the center of the sample which has the maximum ion impact and (b) the edges of the sample which do not have any ion irradiation. The diffraction patterns recorded at these two locations were plotted and compared in Figure 5.35 and Figure 5.36. The plotted pattern showed the characteristic peaks of α-$Al_2O_3$ in pure and irradiated area of 99.9% pure $Al_2O_3$ and $Al_2O_3$:Cr samples. No traces of amorphisation or destruction of crystalline structure of the sample due to irradiation was noticed.

However, a significant change was noticed in the FWHM of the peaks recorded at two different locations. A smaller FWHM was noticed for the peaks recorded from the irradiated region than the peaks from pristine region. This corresponds to larger grain size in the irradiated region compared to the pristine region. The effect was more pronounced in pure $Al_2O_3$ sample than Cr doped $Al_2O_3$, see Figure 5.35 and Figure 5.36.

In literature, irradiation of $Al_2O_3$ sample with swift heavy ions producing amorphisation in material due to high electronic energy loss was reported [108, 130-131]. In the present analysis a reverse effect of irradiation induced grain growth was observed in the $Al_2O_3$ sample. The effect of ion induced grain growth was reported in thin films [132] [133] and oxides [134-135] where the grain diameter increased linearly with dose applied to the materials. G. H. Vineyard [136] and D. Kaoumi *et al.* [137] proposed a model based on the effect of

thermal spike on grain boundaries. It states that the grain boundary migration occurs by atomic jumps within the thermal spikes, biased by the local grain boundary curvature driving. Y. Zhang *et al*. [135] noticed similar effect in irradiated cubic zirconia and explained the process using a defect driven mechanism. The high concentration of defects created during irradiation produced a mechanical instability near grain boundaries by non-equilibrium processes. In such case, the enhanced defect diffusion leads to grain-boundary migration which in turn leads to grain growth, and the phenomena was essentially independent on irradiation temperature.

In $Al_2O_3$, the color of the sample turned from pale white to yellow after irradiation (Figure 5.37). Unlike the $ZrO_2$:Y and $ZrO_2$:Mg (where the color centers were formed only in the irradiated region and resembles the shape of the ion beam, Figure 5.37 ), the color centers were produced over a larger area of the $Al_2O_3$ sample. From the literature, the grain growth in $Al_2O_3$ was attributed to the migration of defects produced on or near grain boundaries. The decoloration of $Al_2O_3$ sample in the unirradiated area clearly shows that the color centers produced during irradiation migrated on further irradiation, thereby increasing the grain size of the material after irradiation, as mentioned in [134-137]. This effect was more pronounced in $Al_2O_3$ than $Al_2O_3$:Cr which clearly shows that the intensity of the defects produced during irradiation is significantly lower in $Al_2O_3$:Cr than $Al_2O_3$.

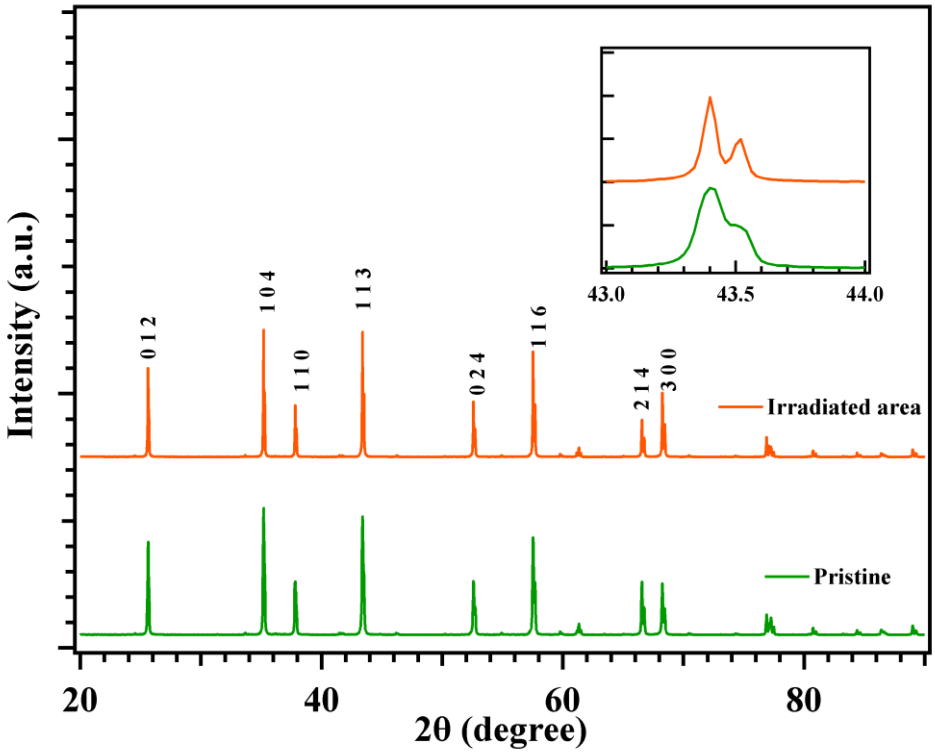


Figure 5.35: The X-ray diffraction obtained from $Al_2O_3$ sample at two different locations (a) Pristine area without any ion impact and (b) center of the sample which has maximum ion irradiation. In the latter, the reflexes are sharper, indicating a larger crystallite size.

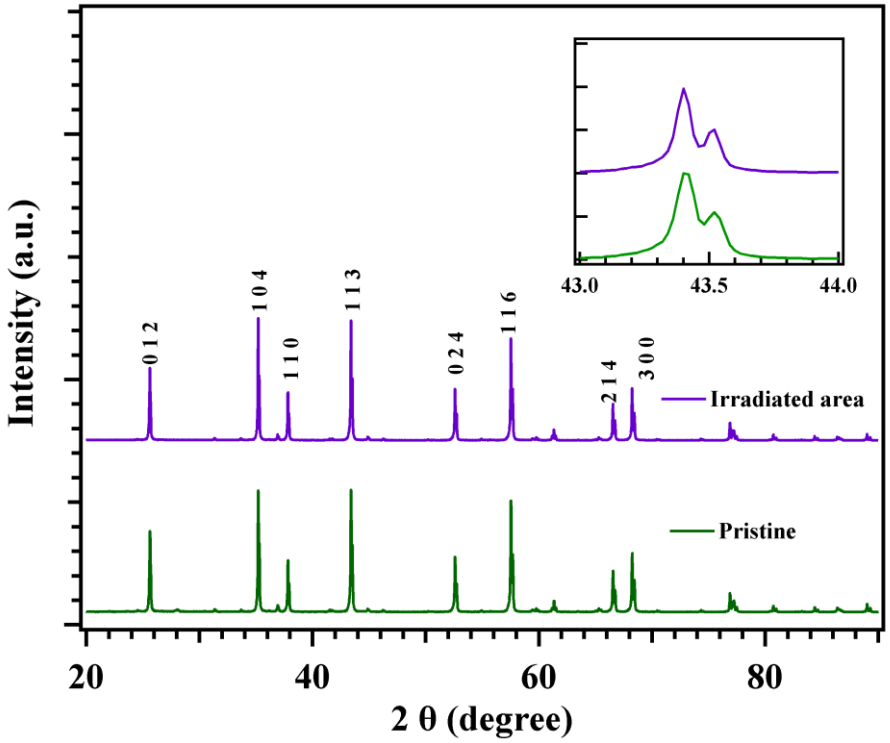


Figure 5.36: The X-ray diffraction obtained from $Al_2O_3$:Cr sample at two different locations (a) Pristine area without any ion impact and (b) center of the sample which has maximum ion irradiation

### 5.3.4 Formation of color centers

During irradiation, due to the formation of color centers, a visible change of the color of $Al_2O_3$ and $ZrO_2$:Y samples is noticed, see Figure 5.37.

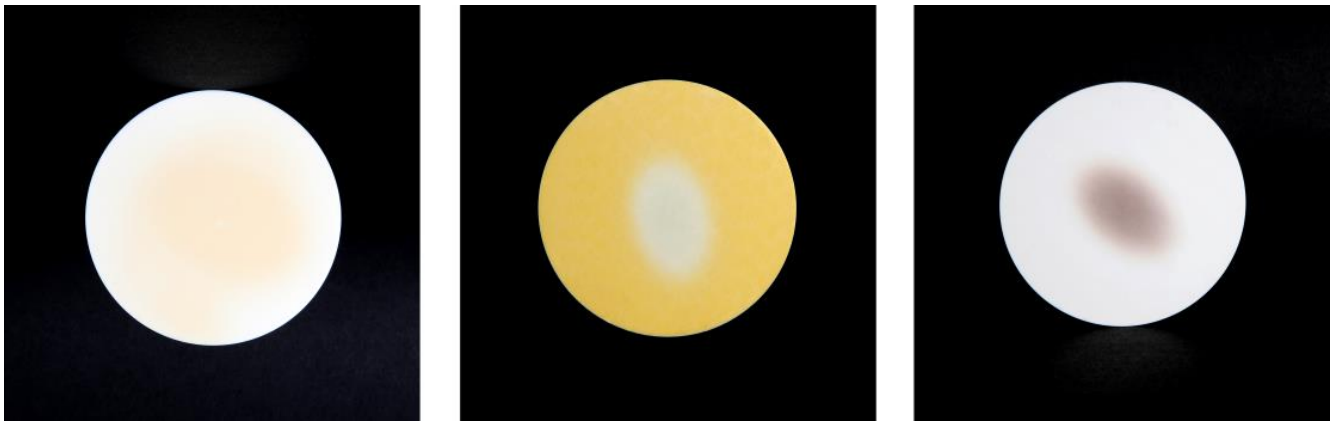

Figure 5.37: Color centers formation in $Al_2O_3$, $ZrO_2$:Mg and $ZrO_2$:Y samples due to ion beam irradiation. The $Al_2O_3$ sample turned from pale white to yellow and $ZrO_2$:Y turned into deep purple. In $ZrO_2$:Mg the screen turned from yellow to white. In both Zirconia samples the shape of the color centers resembles the beam shape whereas in $Al_2O_3$ the color centers spread over the sample.

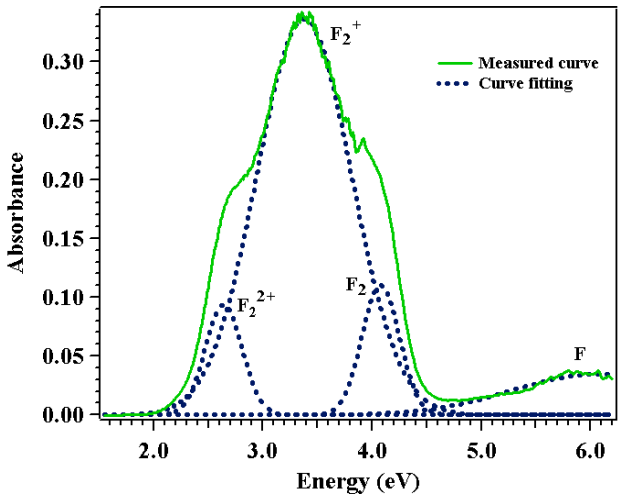


Figure 5.38: Absorption spectra vs. photon energy recorded from $Al_2O_3$ screens irradiated with Ne, Ar and Ta ions. The broad spectrum was fitted with 4 Gaussian curves at 2.65 eV, 3.35 eV, 4.06 eV and 6.06 eV.

These color centers were analysed using the absorption bands obtained from UV-Vis spectrometry [138]. In $Al_2O_3$ (used for the stability measurement, chapter 5.2.2), a broad absorption spectrum obtained was de-convoluted into 4 Gaussian peaks at 2.65 eV, 3.35 eV 4.06 eV and 6.06 eV (see Figure 5.38). According to the literature review these peak positions correspond to color centers in oxides [120] namely $F_2^{2+}$ centers (455 nm, two oxygen vacancies with 2 electrons), $F_2^{+}$ centers (355 nm, two oxygen vacancies with 3 electrons), $F_2$ centers (300 nm, two oxygen vacancies with 4 electrons) and F centers (205 nm). These higher order color centers are called dimer defects ($F_2$, $F_2^{+}$ and $F_2^{2+}$), produced by the clustering of individual oxygen vacancies [117-118, 139-141].

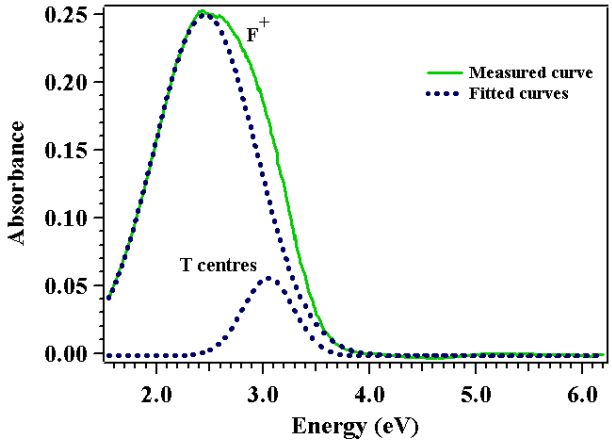


Figure 5.39: Absorption spectra vs. photon energy recorded from $ZrO_2$:Y screens irradiated with Uranium ions. The broad spectrum obtained was fitted with 2 Gaussian curves, corresponding to $F^+$ (2.45 eV) and T centers (3.05 eV).

In case of $ZrO_2$:Y sample, at the irradiated spot, the sample color changed from pure white to purple after irradiating with Uranium ions (linearity measurements, chapter 5.1). The light output from the screen decreased with increase in particle intensity. The measured absorption spectrum shows a broad band with maximum at 2.5 eV (see Figure 5.39). This broad band was de-convoluted into two Gaussian peaks at 2.45 eV (FWHM=0.9 eV) and 3.05 eV (FWHM=0.5 eV). In literature, these bands were associated with $F^+$ center (~500 nm, singly ionised oxygen vacancy) produced by elastic collision and T center (~375 nm, $Zr^{3+}$ in a trigonal symmetry) by electronic excitation, observed using electron paramagnetic resonance spectroscopy (EPR) [96-97].

These color centers are also called intrinsic point defects [142]. The Y- doped $ZrO_2$ sample has a very broad emission spectrum between 300 and 600 nm with maximum at 450 nm [73]. Therefore the strong absorption lines of T centers and $F^+$ centers may overlap with the emission spectrum and lead to the observed decreased light output.

# 6 Summary and Outlook

In the Facility of Antiproton and ion Research (FAIR), scintillation screens will be installed at various locations for ion beam profile measurement. For daily operation, a stable scintillation screen is necessary to perform profile measurements. The major advantage of scintillation screens over other diagnostics devices are (a) Production of high resolution 2-dimensional beam image (b) simple device and (c) reasonable cost. In this PhD thesis work, different types of scintillation screens (i) single crystals (CsI:Tl, YAG:Ce), (ii) Powder screens (P43, P46), (iii) Ceramics ($Al_2O_3$:Cr, $Al_2O_3$, $ZrO_2$:Mg and $ZrO_2$:Y) and (iv) glass material (Herasil, Quartz:Ce) were investigated to understand their imaging properties.

The above mentioned scintillation materials were irradiated with various ion beams extracted from the heavy ion synchrotron SIS-18. The ion beams chosen for the investigation act as the representatives of different elements in the periodic table: Carbon and Neon as an example of light weight ions, Argon as medium weight ion, Tantalum and Uranium as heavy ions. These ion beams were accelerated to energies of 200 MeV/u and 300 MeV/u and applied to the screens. To understand the behaviour of the screens at different particle intensities, the investigation was also carried out using a wide range of particle intensities from $10^4$ to $10^9$ ppp (linearity measurements). For each intensity range with 40 ion pulses, the beam image was captured using a CCD camera and quantitative data analysis was performed. The light output, image width and higher statistical moments were calculated for each beam pulse and compared.

The following properties of the above mentioned scintillation screens were studied with different ion beams,

- Light output
- Image reproduction
- Radiation hardness

The radiation hardness of the screens was examined using Uranium ions accelerated to 200 and 300 MeV/u. An investigation with low energy ions was performed to understand the behaviour of the screens at high energy deposition. The radiation induced modifications in the material was analysed using Raman spectroscopy, X-ray diffraction and UV-Vis absorption spectroscopy.

## Light output

Irrespective of the ion beam, most of the sample showed a very linear light output over particle intensities except Y- and Mg- doped $ZrO_2$ samples. Different light output was recorded depending on the scintillation screen, ion beam and beam intensity. The highest light output was recorded from CsI:Tl, and Herasil yielded the lowest one. Next to CsI:Tl, YAG:Ce (1 mm), P43, P46, $Al_2O_3$:Cr, Quartz:Ce, YAG:Ce (0.25 mm) and $Al_2O_3$ took the consecutive positions. Linear light output over three orders of magnitude particle intensity was noticed for Carbon,

Neon, Argon and Uranium ions, respectively. With very heavy ions such as Uranium, the profile measurement of the high intensity ion beam with sensitive screens was restricted due to CCD saturation. The installation of a second camera with grey filter helped to investigate the screens with high intensity heavy ion beams. The screens were irradiated with the heavy ion Tantalum and the images were captured in both cameras. A significant linear light output over 5 orders of magnitude particle intensity was recorded from $10^4$ to $10^9$ ppp, which is the maximum particle range available in the experimental location.

The scintillation screens showed the following unique properties independent on the ion beam used.

(a) The Cr- doped aluminium oxide ($Al_2O_3$:Cr) always produced a factor 10 more light output than undoped aluminium oxide ($Al_2O_3$).

(b) A factor two higher light output was registered from P46 compared to crystalline YAG:Ce (0.25 mm) which were both prepared from the same source material.

(c) A factor of 10 more light output was noticed from the single crystals YAG:Ce (1 mm, produced by Saint-Gobain) in comparison to YAG:Ce (0.25 mm, produced by Crytur Ltd). Because the method of crystal growth and the Cerium concentration for the Saint-Gobain product was not disclosed, this result cannot be interpreted.

In addition, when the light output was normalised to energy deposition, the samples showed a non-proportional behaviour. A factor of 2 higher light yields is obtained for lighter ions in comparison to heavy ions.

## Image reproduction

In the image reproduction, different image widths were obtained for the same ion beam. A maximum difference up to 50 % was recorded between $ZrO_2$:Y and Herasil. Among the investigated screens, broader image profiles were registered for the standard scintillators CsI:Tl ,YAG:Ce (1 mm) and $ZrO_2$:Y compared to other materials and the reference detector MWPC. The other materials P43, P46, $Al_2O_3$:Cr, $Al_2O_3$ and YAG:Ce (0.25 mm) reproduce the image width within a difference of ±4 %, from lower to higher particle intensities. Further, the higher statistical moments characterized the constant behaviour of the screens over the wide intensity range. Broader image profiles obtained from the thick scintillations screens is due to the multi photon interaction and light transportation in single crystals.

## Radiation hardness

After recording a satisfactory behaviour of the scintillation screens in linearity measurements, these screens were subjected to radiation tolerance test with continuous irradiation with Uranium ions. Among the four selected samples ($Al_2O_3$:Cr, $Al_2O_3$, P43 and P46), a stable behaviour over 1000 pulses was recorded for $Al_2O_3$:Cr. The other materials such as P43, P46 and $Al_2O_3$ got saturated upon irradiation. About 40 % decreased light output between the 1$^{st}$ and the 1000$^{th}$ pulse was recorded for P43 (20 % in P46 and 11 % in $Al_2O_3$). The dose deposited over the thickness of the sample is much higher in case of powder screens than in case of aluminium oxide ceramics. This resulted in quenching of excitations in the powder

screens. Nevertheless, all these screens showed a stable tendency over 250 pulses at reduced intensity ($4\times10^8$ ppp).

The scintillation screen radiation modification analysis was carried out using Raman spectroscopy, X-ray diffraction and UV-Vis spectroscopy. Except a strong fluorescence background, no significant change was obtained in the Raman spectra recorded from the irradiated region of P46, $Al_2O_3$:Cr and $Al_2O_3$. The intensity of the fluorescence background was higher in the center of the samples which was irradiated with higher particle fluence. These fluorescence backgrounds were attributed to defects and color centers produced in the material during irradiation. In the X-ray diffraction analysis, no traces of amorphisation were noticed. However a smaller FWHM was noticed in the peaks recorded from the irradiated region of $Al_2O_3$ and $Al_2O_3$:Cr corresponding to irradiation induced grain growth by grain boundary migration.

In $Al_2O_3$ and $ZrO_2$:Y a significant change in the color of the samples was noticed at the irradiated part. This color change was due to the formation of color centers during irradiation. The curve fitting of UV-Vis absorption spectra measured at the irradiated area of the $Al_2O_3$ sample suggests the formation of F, $F_2$, $F_2^+$ and $F_2^{2+}$ centers. In case of $ZrO_2$:Y, the absorption spectrum analysis indicates the formation of $F^+$ and T centers.

## Outlook

Among the investigated scintillation screen materials, Cr doped $Al_2O_3$ gave the best behaviour both in linearity test and stability test. However, the light output was a factor of 2 less compared to P43. For this material, a stable behaviour in linearity and radiation stability test was registered up to a certain threshold. In addition, P43 and P46 did not show any radiation damage over the complete investigation. This characteristic property suggests to consider P43 and P46 for profile measurements up to the threshold region. Measurements at higher particle intensity can be performed using $Al_2O_3$:Cr screens.

In the FAIR accelerator, heavy ions like Uranium will be accelerated to a maximum energy of 20 GeV/u. The highly accelerated ion will deposit less energy in the material since it will penetrate it with lower energy loss per unit length and volume. At 2 GeV/u, the Uranium ions will deposit a factor 2 less energy in materials than at 269 MeV/u (Figure A 21). Thus the use of the scintillation screen is limited at lower intensity of highly accelerated ions due to the decreased light output due to low energy deposition. A more advanced experimental device (with intensifier cameras) may help to perform the experiments under such conditions.

The results presented are only the response of the screens irradiated with slow extracted ion beams. The properties and the results may vary when the materials are irradiated with fast extracted beams, where the total energy deposition will take place for time duration of some $\mu s$. In such condition, specific research work has to be carried out to find a suitable screen for profile measurements. A detailed analysis using fast extracted beams will help to understand the complete nature of the scintillation screens towards heavy ion irradiation.

# 7 Bibliography


[1] S. Y. Lee, *Accelerator physics*, Second edition, Singapore: world scientific publishing Co.Pte. Ltd, 2004.

[2] E. J. N. Wilson, *An introduction to particle accelerators*. New York: Oxford University Press, 2001.

[3] P. Forck, "Lecture Notes on Beam Instrumentation and Diagnostics," Joint University Accelerator School (JUAS), 2009.

[4] P. Strehl, *Beam Instrumentation and Diagnostics*: Springer Verlag: Berlin, Heidelberg, New York, 2006.

[5] P. J. Ouseph, *Introduction to nuclear radiation detectors* vol. 2. New York: Plenum Press, 1975.

[6] C. Grupen and B. Shwartz, *Particle detectors*, Second edition, New York: Cambridge University Press, 2008.

[7] G. F. Knoll, *Radiation Detection and Measurement*, Second edition, New York: John Wiley & Sons, 1989.

[8] R. Jung*, et al.*, "Single pass optical profile monitoring," in *Proceedings of European Workshop on Beam Diagnostics and Instrumentation for Particle Accelerators (DIPAC)*, Mainz, Germany, 2003.

[9] C. Bal*, et al.*, "Scintillating screens study for LEIR/LHC heavy ion beams," in *Proceedings of European Workshop on Beam Diagnostics and Instrumentation for Particle Accelerators (DIPAC),* Lyon, France, 2005.

[10] A. H. Lumpkin*, et al.*, "Optical techniques for electron -beam characterisations on the APS SASE FEL project," *Nuclear Instruments and Methods in Physics Research A,* vol. 429, pp. 336-340, 1999.

[11] http://www.gsi.de.

[12] "Operation regulations for the GSI accelerators and experimental facilities," GSI, Darmstadt, December 2009.

[13] http://www.fair-center.de/de/oeffentlichkeit/was-ist-fair/beschleuniger.html.

[14] P. Spiller and G. Franchetti, "The FAIR accelerator project at GSI," *Nuclear Instruments & Methods in Physics Research Section a-Accelerators Spectrometers Detectors and Associated Equipment,* vol. 561, pp. 305-309, 2006.

[15] http://www.fair-center.de.

[16] W. R. Leo, *Techniques for Nuclear Physics Experiments*, Second revised edition, Springer Verlag: Berlin, Heidelberg, New York ,1994.

[17] G. Blasse and B. C. Grabmaier, *Luminescent Materials*. Springer Verlag: Berlin, Heidelberg, New York, 1994.

[18] A. N. Vasil'ev, "Relaxation of hot electron excitation in scintillators: account for scattering, track effects, complicated electronic structure.," in *International conference on Inorganic scintillators and their applications*, Moscow, 2000.

[19] P. Lecoq*, et al.*, *Inorganic Scintillators for Detector Systems*. Springer Verlag: Berlin, Heidelberg, New York, 2006.

[20] P. A. Rodnyi, *Physical processes in inorganic scintillators*. New York: CRC press, 1997.

[21] M. Gaft*, et al.*, *Luminescence spectroscopy of minerals and materials*. Springer Verlag: Berlin, Heidelberg, New York, 2010.

[22] E. B. Podgoršak, *Radiation Physics for Medical Physicists*: Springer Verlag: Berlin, Heidelberg, New York, 2006.

[23] http://www.srim.org/.

[24] M. J. Weber, "Scintillation: mechanism and new crystals," *Nuclear Instrumentation and Methods in Physics Research A,* vol. 527, pp. 9-14, 2004.

[25] F. H. Marshall*, et al.*, "The Photo-Multiplier Radiation Detector," *The Review of Scientific Instruments,* vol. 19, p. 28, 1948.

[26] H. Kallmann, "Quantitative Measurements with Scintillation Counters," *Physical Review,* vol. 75, pp. 623-626, 1949.

[27] M. Furst and H. Kallman, "High Energy Induced Fluorescence in Organic Liquid Solution " *Physical Review,* vol. 85, pp. 816-825, 1952.

[28] M. J. Weber*, et al.*, "Measurements of ultrafast scintillation rise times:evidence of energy fransfer mechanisms," *Journal of Luminescence,* vol. 87, p. 3, 2000.

[29] P. A. Rodnyi*, et al.*, "Energy-Loss in Inorganic Scintillators," *Physica Status Solidi B-Basic Research,* vol. 187, pp. 15-29, 1995.

[30] A. Lempicki, "The physics of inorganic scintillators," *Journal of Applied Spectroscopy,* vol. 62, p. 16, 1995.

[31] A. Kitai, *Luminescent materials and application*. Chichester: John Wiley & Sond Ltd, 2008.

[32] B. Henderson and G. F. Imbusch, *Optical spectroscopy of inorganic solids*. NewYork: Oxford University Press, 1989.

[33] S. W. S. McKeever, *Thermoluminescence of Solids*: Cambridge University Press, 1988.

[34] J. Solé*, et al.*, *An Introduction to the Optical Spectroscopy of Inorganic Solids*: John Wiley &Sons Ltd, Chichester, 2005.

[35] A. N. Belsky*, et al.*, "Luminescence quenching as a probe for the local density of electronic excitations in insulators," *Journal of Electron Spectroscopy and Related Phenomena,* vol. 79, pp. 147-150, 1996.

[36] R. A. Glukhov and A. N. Vasilev, "Monte-Carlo simulation of the creation of excited regions in insulators by a photon," *Radiation Effects and Defects in Solids,* vol. 135, pp. 813-817, 1995.

[37] D. J. Gardiner*, et al.*, *Practical Raman spectroscopy*: Springer Verlag: Berlin, Heidelberg, New York, 1989.

[38] E. Smith and G. Dent, *Modern Raman Spectroscopy: A Practical Approach*. West Sussex: John Wiley & Sons Ltd, 2005.

[39] P. Larkin, *Infrared and Raman Spectroscopy; Principles and Spectral Interpretation*. Elsevier Science, Amsterdam, 2011.

[40] P. B. Hirsch, *X-Ray Diffraction by Polycrystalline Materials*. London: John Wright & Sons Ltd, 1955.

[41] M. Kakudo and N. Kasai, *X-Ray Diffraction by Polymers*. Tokyo: Kodansha LTD, 1972.

[42] E. Lifshin, *X- ray Characterisation of Materials*. Wiley-VCH Verlag GmbH: Weinheim, New York, Chichester, Brisbane, Singapore, Toronto, 1999.

[43] R. Guinebretière, *X-Ray Diffraction by Polycrystalline Materials*. London: ISTE Ltd, 2007.

[44] D. K. Bowen and B. K. Tanner, *High Resolution X-Ray Diffractometry And Topography*. *London*: Taylor & Francis, 2005.

[45] D. Brandon and W. D. Kaplan, *Microstructural Characterisation of Materials*. Chichester: John Wiley & Sons, 1999.

[46] C. Koch*, et al.*, *Structural Nanocrystalline Materials: Fundamentals and Applications*, Cambridge University Press, 2007.

[47] P. Forck*, et al.*, "Beam Diagnostics for the upgraded UNILAC at GSI," in *Proceedings of European Particle Accelerator Conference* (*EPAC)*, Stockholm, Sweden, 1998.

[48] P. Strehl, "Diagnostics in heavy ion machines," in *Proceedings of European Workshop on Beam Diagnostics and Instrumentation for Particle Accelerators (DIPAC)*, Chester, UK, 1999.

[49] K. Unser, "A Toroidal DC Beam Current Transformer with High-Resolution," *IEEE Transactions on Nuclear Science,* vol. 28, pp. 2344-2346, 1981.

[50] P. Forck*, et al.*, "Detectors for Slowly Extracted Heavy Ions at the GSI Facility," in *Proceedings of European Workshop on Beam Diagnostics and Instrumentation for Particle Accelerators (DIPAC)*, Frascati, Italy, 1997.

[51] A. Peters*, et al.*, "A cryogenic current comparator for the absolute measurement of nA beams," in *Proceedings of Beam instrumentation workshop (BIW)*, Stanford, California (USA), pp.163-180, 1998.

[52] P. Forck*, et al.*, "Intensity Measurement in the High Energy Beam Lines," p.157, GSI scientific report 1995.

[53] P. Forck*, et al.*, "Intensity Measurement of High-Energy Heavy Ions at the GSI Facility," in *Proceedings of Beam instrumentation workshop* (*BIW)*, Argonne, pp.422-429, 1996.

[54] A. Breskin*, et al.*, "Multistep Avalanche Chamber - New Family of Fast, High-Rate Particle Detectors," *Nuclear Instruments & Methods,* vol. 161, pp. 19-34, 1979.

[55] H. Stelzer, "Multiwire chambers with a two-stage gas amplification," *Nuclear Instruments and Methods in Physics Research A,* vol. 310, pp. 103-106, 1991.

[56] P. Lecoq, "Results on New Scintillating Crystals from the Crystal Clear Collaboration," *IEEE Transactions on Nuclear Science,* vol. 40, pp. 409-412, 1993.

[57] P. Lecoq and M. Korzhik, "Scintillator developments for high energy physics and medical imaging," *IEEE Transactions on Nuclear Science,* vol. 47, pp. 1311-1314, 2000.

[58] W. W. Moses*, et al.*, "Prospects for dense, infrared emitting scintillators," *IEEE Transactions on Nuclear Science,* vol. 45, pp. 462-466, 1998.

[59] I. G. Valais*, et al.*, "Luminescence emission properties of (Lu, Y)(2)$SiO_5$ : Ce (LYSO : Ce) and (Lu, Y)$AlO_3$ : Ce (LuYAP : Ce) single crystal scintillators under medical imaging conditions," *IEEE Transactions on Nuclear Science,* vol. 55, pp. 785-789, 2008.

[60] I. G. Valais*, et al.*, "Comparative evaluation of single crystal scintillators under x-ray imaging conditions," *Journal of Instrumentation,* vol. 4, issue 6, pp. 6-13, 2009.

[61] N. R. Comins*, et al.*, "Preparation and Evaluation of P-47 Scintillators for a Scanning Electron-Microscope," *Journal of Physics E-Scientific Instruments,* vol. 11, pp. 1041-1047, 1978.

[62] A. R. Wilson, "The Response of Yttrium-Aluminum-Garnet Scintillator and Photodiode-Array Detectors Used in Peels," *Measurement Science & Technology,* vol. 4, pp. 835-841, 1993.

[63] H. Retot, *et al.*, "Synthesis and optical characterization of $SrHfO_3$ : Ce and $SrZrO_3$ : Ce nanoparticles," *Optical Materials,* vol. 30, pp. 1109-1114, 2008.

[64] R. Autrata and J. Hejna, "Detectors for Low-Voltage Scanning Electron-Microscopy," *Scanning,* vol. 13, pp. 275-287, 1991.

[65] E. Gütlich, *et al.*, "Scintillation Screen Investigations for High-Current Ion Beams," *IEEE Transaction on Nuclear Science,* vol. 57, pp. 1414-1419, 2010.

[66] A. Peters, *et al.*, "Transverse beam profile measurements using optical methods," in *Proceedings of European Workshop on Beam Diagnostics and Instrumentation for Particle Accelerators (DIPAC)*, ESRF,Grenoble, 2001.

[67] A. Peters, *et al.*, "2D-Characterisation of ion beams using viewing screens," in *Proceedings of European Particle Accelerator Conference (EPAC)*, Paris, France, 2002.

[68] http://www.detectors.saint-gobain.com/uploadedFiles/SGdetectors/Documents/Product_Data_Sheets/YAG-Data-Sheet.pdf.

[69] A. Quaranta, *et al.*, "Radiation damage mechanisms in CsI(Tl) studied by ion beam induced luminescence," *Nuclear Instruments & Methods in Physics Research Section B-Beam Interactions with Materials and Atoms,* vol. 266, pp. 2723-2728, 2008.

[70] J. A. Mares, *et al.*, "Scintillation response of Ce-doped or intrinsic scintillating crystals in the range up to 1 MeV," *Radiation Measurements,* vol. 38, pp. 353-357, 2004.

[71] H. J. Eichler, *et al.*, "Orange, Red and Deep-Red Flashlamp-Pumped Pr3+-Liyf4 Laser with Improved Output Energy and Efficiency," *Applied Physics B-Lasers and Optics,* vol. 58, pp. 421-424, 1994.

[72] E. Gütlich, *et al.*, "Quantitative scintillation screen studies at GSI-LINAC and related model calculation," in *Proceedings of European Workshop on Beam Diagnostics and Instrumentation for Particle Accelerators (DIPAC)*, Hamburg, Germany, p. 179, 2011.

[73] E. Gütlich, "Abbildungseigenschaften von Scintillatoren für Schwerionenstrahlen und diesbezügliche Modellrechnungen," Ph.D Thesis, Material Analysis, Technical University of Darmstadt, Darmstadt, 2011.

[74] K. J. McCarthy, *et al.*, "Response of chromium-doped alumina screens to soft x rays using synchrotron radiation," *Journal of Applied Physics,* vol. 94, pp. 958-962, 2003.

[75] S. E. Paje and J. Llopis, "Photoluminescence-Spectra study of Yttria-stablised Zirconia," *Journal of Applied Physics A,* vol. 57, pp. 225-228, 1993.

[76] E. J. Popovici, *et al.*, "Synthesis and characterisation of rare earth oxysulphide phosphors. I. Studies on the preparation of $Gd_2O_2S$ : Tb phosphor by the flux method," *Optical Materials,* vol. 27, pp. 559-565, 2004.

[77] M. A. Gevelber, *Dynamics and Control of the Czochralski Process*: Massachusetts Institute of Technology, Department of Mechanical Engineering, 1988.

[78] G. M. Wolten, "Diffusionless Phase Transformations in Zirconia and Hafnia," *Journal of the American Ceramic Society,* vol. 46, pp. 418-422, 1963.

[79] T. Lefevre*, et al.*, "A large scintillating screen for the LHC dump line," in *Proceedings of European Workshop on Beam Diagnostics and Instrumentation for Particle Accelerators (DIPAC)*, Venice, Italy, 2007.

[80] http://www.alliedvisiontec.com/de.

[81] R. Haseitl*, et al.*, "Beamview - A data acquisation system for optical beam instrumentation " in *Proceedings of International Workshop on Personal Computer and Particle Accelerator Controls (PCaPAC)*, Ljubljana, Slovenia, 2008.

[82] T. Hoffmann*, et al.*, "A fast VME data acquisation system for spill analysis and beam loss measurements," in *Proceedings of Beam instrumentation workshop (BIW)*, Upton, New York, pp. 329-336, 2002.

[83] http://www.itos.de/deutsch/schott/dichtefilter/dichtefilter.php.

[84] http://en.wikipedia.org/wiki/Data_analysis.

[85] http://learntech.uwe.ac.uk/da/Default.aspx?pageid=1423.

[86] W. H. Press*, et al.*, *Numerical Recipes*. Cambridge University Press: New York, 2007.

[87] T. T. Soong, *Fundamentals of probability and statistics for engineers*. John Wiley &Sons, Ltd: Chichester, 2004.

[88] http://rsbweb.nih.gov/ij/features.html.

[89] K. Michaelian*, et al.*, "Scintillation Response of Nuclear-Particle Detectors," *Nuclear Instruments & Methods in Physics Research Section a-Accelerators Spectrometers Detectors and Associated Equipment,* vol. 356, pp. 297-303, 1995.

[90] W. W. Moses*, et al.*, "Scintillator non-proportionality: Present understanding and future challenges," *IEEE Transactions on Nuclear Science,* vol. 55, pp. 1049-1053, 2008.

[91] http://www.wavemetrics.net.

[92] K. Levenberg, "A Method for Solution of Certain Non-Linear Probles in Least Squares," *The Quaterly of Applied Mathematics,* vol. 2, pp. 164-168, 1944.

[93] D. W. Marquardt, "An algorithn for least squares estimation of nonlinear parameters," *Journal of the society for industrial and applied mathematics,* vol. 11, pp. 431-441, 1963.

[94] HORIBA Jobin Yvon HR800 $^{TM}$ User manual.

[95] http://www.crytur.cz/pages/9/scintillation-detectors.

[96] J. M. Costantini, *et al.*, "Generation of colour centers in yttria-stabilized zirconia by heavy ion irradiations in the GeV-range," *Journal of Physics-Condensed Matter,* vol. 22, 2010.

[97] J. M. Costantini, *et al.*, "Colour centre production in yttria-stabilized zirconia by swift charged particle irradiations," *Journal of Physics-Condensed Matter,* vol. 16, pp. 3957-3971, 2004.

[98] P. Antich, *et al.*, "3D position readout from thick scintillators," *Nuclear Instruments and Methods in Physics Research Section A: Accelerators, Spectrometers, Detectors and Associated Equipment,* vol. 480, pp. 782-787, 2002.

[99] R. Gwin and R. B. Murray, "Scintillation Process in CsI(Tl). II. Emission Spectra and the Possible Role of Self-Trapped Holes," *Physical Review,* vol. 131, pp. 508-512, 1963.

[100] J. B. West, "A theoretical model for the migration of energy from the particle track in an inorganic scintillator," *Journal of Physics B: Atomic and Molecular Physics,* vol. 3, p. 1692, 1970.

[101] R. Katz and E. J. Kobetich, "Response of NaI(Tl) to Energetic Heavy Ions," *Physical Review,* vol. 170, pp. 397-400, 1968.

[102] M. Lang, *et al.*, "Review of A(2)B(2)O(7) pyrochlore response to irradiation and pressure," *Nuclear Instruments & Methods in Physics Research Section B-Beam Interactions with Materials and Atoms,* vol. 268, pp. 2951-2959, 2010.

[103] B. Schuster, *et al.*, "Response behavior of $ZrO_2$ under swift heavy ion irradiation with and without external pressure," *Nuclear Instruments & Methods in Physics Research Section B-Beam Interactions with Materials and Atoms,* vol. 277, pp. 45-52, 2012.

[104] B. Schuster, *et al.*, "Structural phase transition in $ZrO_2$ induced by swift heavy ion irradiation at high-pressure," *Nuclear Instruments & Methods in Physics Research Section B-Beam Interactions with Materials and Atoms,* vol. 267, pp. 964-968, 2009.

[105] A. Benyagoub, "Kinetics of the crystalline to crystalline phase transformation induced in pure zirconia by swift heavy ion irradiation," *Nuclear Instruments & Methods in Physics Research Section B-Beam Interactions with Materials and Atoms,* vol. 206, pp. 132-138, 2003.

[106] A. Benyagoub, "Phase transformations in oxides induced by swift heavy ions," *Nuclear Instruments & Methods in Physics Research Section B-Beam Interactions with Materials and Atoms,* vol. 245, pp. 225-230, 2006.

[107] M. Tang, *et al.*, "Heavy ion irradiation-induced phase transformation in polycrystalline $Dy_2O_3$," *Philosophical Magazine,* vol. 86, pp. 1597-1613, 2006.

[108] H. Abe, *et al.*, "Amorphization in aluminum oxide induced by ion irradiation," *Nuclear Instruments & Methods in Physics Research Section B-Beam Interactions with Materials and Atoms,* vol. 127, pp. 170-175, 1997.

[109] G. Sattonnay, *et al.*, "Effect of composition on the behavior of pyrochlores irradiated with swift heavy ions," *Nuclear Instruments & Methods in Physics Research Section B-Beam Interactions with Materials and Atoms,* vol. 272, pp. 261-265, 2012.

[110] M. Lang, *et al.*, "Swift heavy ion-induced amorphization of $CaZrO_3$ perovskite," *Nuclear Instruments & Methods in Physics Research Section B-Beam Interactions with Materials and Atoms,* vol. 286, pp. 271-276, 2012.

[111] J. M. Costantini, *et al.*, "Amorphization and recrystallization of yttrium iron garnet under swift heavy ion beams," *Journal of Applied Physics,* vol. 87, pp. 4164-4174, 2000.

[112] A. Audouard, *et al.*, "Structural modifications induced by electronic energy loss in $Ni_3B$ irradiated with GeV heavy ions," *European Physical Journal-Applied Physics,* vol. 3, pp. 149-158, 1998.

[113] R. Kumar, *et al.*, "Study of columnar amorphization and structural symmetry changes produced by swift heavy ion irradiation in $YBa_2Cu_3O_{7-y}$ thin films using STM," *Solid State Communications,* vol. 106, pp. 805-810, 1998.

[114] S. J. Zinkle, *et al.*, "On the conflicting roles of ionizing radiation in ceramics," *Nuclear Instruments & Methods in Physics Research Section B-Beam Interactions with Materials and Atoms,* vol. 191, pp. 758-766, 2002.

[115] G. Bujnarowski, *et al.*, "Accumulation of mechanical stress in $Al_2O_3$:Cr under swift heavy ion irradiation," *Radiation Effects and Defects in Solids,* vol. 164, pp. 409-416, 2009.

[116] R. Y. Zhu, "Radiation damage in scintillating crystals," *Nuclear Instruments & Methods in Physics Research Section a-Accelerators Spectrometers Detectors and Associated Equipment,* vol. 413, pp. 297-311, 1998.

[117] Y. Chen and M. M. Abraham, "Radiation damage in $Al_2O_3$ crystals implanted with 3.8 MeV Fe2+ ions," *Nuclear Instrumentation and Methods in Physics Research B,* vol. B59/60, pp. 1163-1166, 1991.

[118] P. W. Levy, "Color Centers and Radiation-Induced Defects in $Al_2O_3$," *Physical Review,* vol. 123, pp. 1226-1233, 1961.

[119] Y. F. Song, *et al.*, "Color center formation in alpha-$Al_2O_3$ induced by high energy heavy ions," *Nuclear Instruments & Methods in Physics Research Section B-Beam Interactions with Materials and Atoms,* vol. 254, pp. 268-272, 2007.

[120] E. A. Kotomin and A. I. Popov, "Radiation-induced point defects in simple oxides," *Nuclear Instruments and Methods in Physics Research Section B: Beam Interactions with Materials and Atoms,* vol. 141, pp. 1-15, 1998.

[121] T. T. Basiev, *et al.*, "Optical Fluoride and Oxysulphide Ceramics: Preparation and Characterization," in *Developments in Ceramic Material Research*, D. Rosslere, Ed., ed New York: Nova science publishers, Inc, p. 80, 2007.

[122] L. W. Hobbs, *et al.*, "Radiation effects in ceramics," *Journal of Nuclear Materials,* vol. 216, pp. 291-321, 1994.

[123] W. J. Weber, *et al.*, "Radiation effects on materials in high-radiation environments: A workshop summary," *Journal of Nuclear Materials,* vol. 184, pp. 1-21, 1991.

[124] S. J. Zinkle and C. Kinoshita, "Defect production in ceramics," *Journal of Nuclear Materials,* vol. 251, pp. 200-217, 1997.

[125] N. Khalfaoui, *et al.*, "Damage creation threshold of $Al_2O_3$ under swift heavy ion irradiation," *Nuclear Instruments and Methods in Physics Research Section B: Beam Interactions with Materials and Atoms,* vol. 286, pp. 247-253, 2012.

[126] C. L. Angell, "Raman Spectroscopic Investigation of Zeolites and Adsorbed Molecules," *Journal of Physical Chemistry,* vol. 77, pp. 222-227, 1973.

[127] H. Jeziorowski and H. Knozinger, "Scattering Background in Laser Raman-Spectra of Oxide Surfaces," *Chemical Physics Letters,* vol. 42, pp. 162-165, 1976.

[128] R. M. Gilbert, "Photobleaching of Radiation-Induced Color-Centers in a Germania-Doped Glass-Fiber," *IEEE Transactions on Nuclear Science,* vol. 29, pp. 1484-1488, 1982.

[129] V. N. Kuznetsov and N. Serpone, "Photoinduced Coloration and Photobleaching of Titanium Dioxide in $TiO_2$/Polymer Compositions upon UV- and Visible-Light Excitation of Color Centers' Absorption Bands: Direct Experimental Evidence Negating Band-Gap Narrowing in Anion-/Cation-Doped $TiO_2$," *The Journal of Physical Chemistry C,* vol. 111, pp. 15277-15288, 2007.

[130] K. R. Nagabhushana, *et al.*, "Ion beam induced modifications in electron beam evaporated aluminum oxide thin films," *Nuclear Instruments and Methods in Physics Research Section B: Beam Interactions with Materials and Atoms,* vol. 266, pp. 1475-1479, 2008.

[131] N. Okubo, *et al.*, "Surface amorphization in $Al_2O_3$ induced by swift heavy ion irradiation," *Nuclear Instruments and Methods in Physics Research Section B: Beam Interactions with Materials and Atoms,* vol. 314, pp. 208-210, 2013.

[132] P. Wang, *et al.*, "Implantation and grain growth in Ni thin films induced by Bi and Ag ions," *Nuclear Instruments and Methods in Physics Research Section B: Beam Interactions with Materials and Atoms,* vol. 16, pp. 288-292, 1986.

[133] P. Wang, *et al.*, "Implantation of Ni thin films and single crystals with Ag ions," *Nuclear Instruments and Methods in Physics Research Section B: Beam Interactions with Materials and Atoms,* vol. 7–8, Part 1, pp. 97-102, 1985.

[134] Y. Zhang, *et al.*, "The effect of electronic energy loss on irradiation-induced grain growth in nanocrystalline oxides," *Physical Chemistry Chemical Physics,* vol. 16, pp. 8051-8059, 2014.

[135] Y. Zhang*, et al.*, "Grain growth and phase stability of nanocrystalline cubic zirconia under ion irradiation," *Physical Review B,* vol. 82, p. 184105, 2010.

[136] G. H. Vineyard, "Thermal spikes and activated processes," *Radiation Effects,* vol. 29, pp. 245-248, 1976.

[137] D. Kaoumi*, et al.*, "A thermal spike model of grain growth under irradiation," *Journal of Applied Physics,* vol. 104, 2008.

[138] http://instrumentalanalysis.community.uaf.edu/files/2013/01/UV-Vis_manual2.pdf.

[139] A. Al Ghamdi and P. D. Townsend, "Ion beam excited luminescence of sapphire," *Nuclear Instruments and Methods in Physics Research Section B: Beam Interactions with Materials and Atoms,* vol. 46, pp. 133-136, 1990.

[140] G. J. Pogatshnik*, et al.*, "A Model of Lattice-Defects in Sapphire," *IEEE Transactions on Nuclear Science,* vol. 34, pp. 1709-1712, 1987.

[141] R. Ramirez*, et al.*, "Optical properties of vacancies in thermochemically reduced Mg-doped sapphire single crystals," *Journal of Applied Physics,* vol. 101, 2007.

[142] C. Jean-Marc and B. François, "Point defects induced in yttria-stabilized zirconia by electron and swift heavy ion irradiations," *Journal of Physics: Condensed Matter,* vol. 23, p. 115902, 2011.

# Abbreviations

| | |
|---|---|
| ABLASS | A beam loss measurement and scaling system |
| ADC | Analog digital converter |
| ASCII | American standard code for information interchange |
| BGO | Bismuth germanium oxide |
| BNC | Bayonet Neill-Concelman |
| CCD | Charge coupled device |
| CAD | Computer-aided drafting |
| e-h | Electron-hole |
| FAIR | Facility of Antiproton and Ion Research |
| GSI | Gesellschaft für Schwerionenforschung |
| HEBT | High energy beam transport |
| IC | Ionization chamber |
| KGy | Kilo Grey |
| LINAC | Linear accelerator |
| LHC | Large hadron collider |
| MEVVA | Metal vapour vacuum arc |
| MeV/u | Mega electron volt per nucleon |
| MUCIS | Multi cusp ion source |
| MWPC | Multi wire proportional chamber |
| NIM | Nuclear instrumentation module |
| ppp | Particles per pulse |
| pps | Particles per second |
| PET | Positron emission tomography |
| P43 | Powder screen Gadolinium oxy sulphide ($Gd_2O_2S$:Tb) |
| P46 | Powder screen Yttrium aluminium garnet ($Y_3Al_5O_{12}$:Ce) |
| PWO | Lead tungstate |

| | |
|---|---|
| RHIC | Relativistic heavy ion collider |
| ROI | Region of interest |
| SIS18 | Schwerionensynchrotron with rigidity 18 Tm |
| SIS 100/300 | Schwerionensynchrotron with rigidity 100/300 Tm |
| SEM | Secondary electron monitor |
| SPECT | Single photon emission computed tomography |
| SRIM | Stopping and range of ions in matter |
| STH | Self trapped hole |
| STE | Self trapped exciton |
| TRIM | Transport of Ions in Matter |
| TTL | Transistor-transistor logic |
| UNILAC | Universal linear accelerator |
| VGA | Video graphic array |
| YAG | Yttrium aluminium garnet |

# Appendix

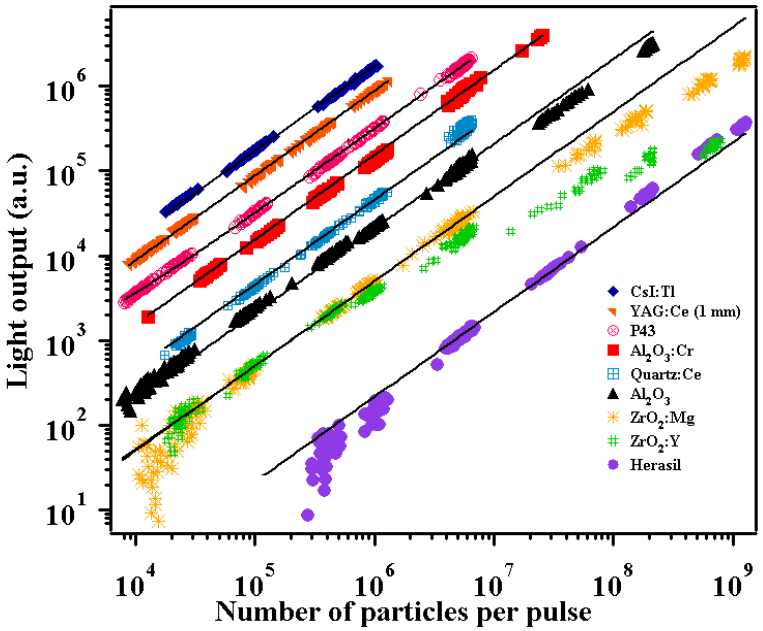


Figure A 1: Light output obtained from several scintillation screens in preliminary measurements. Beam parameters: Uranium at 269 MeV/u, 0.3 s pulse length and 0.25 Hz repetition rate.

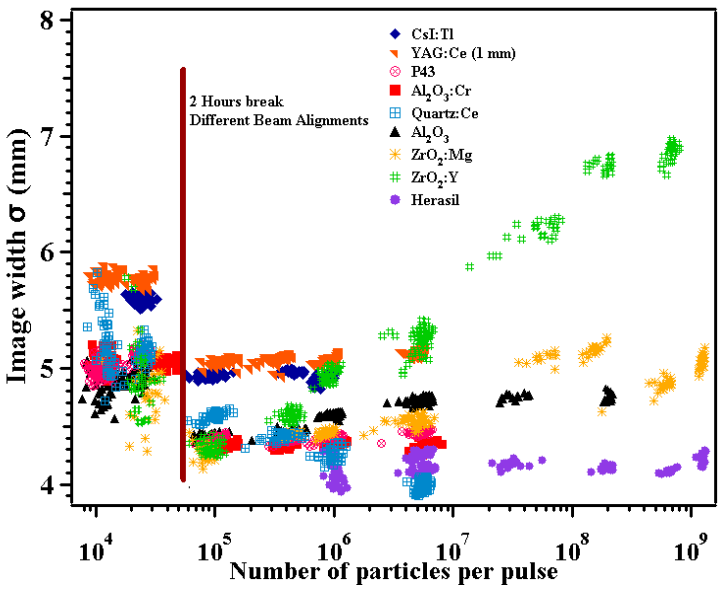


Figure A 2: Image width σ obtained from several scintillation screens in preliminary measurements. Beam parameters were same as Figure A 1.

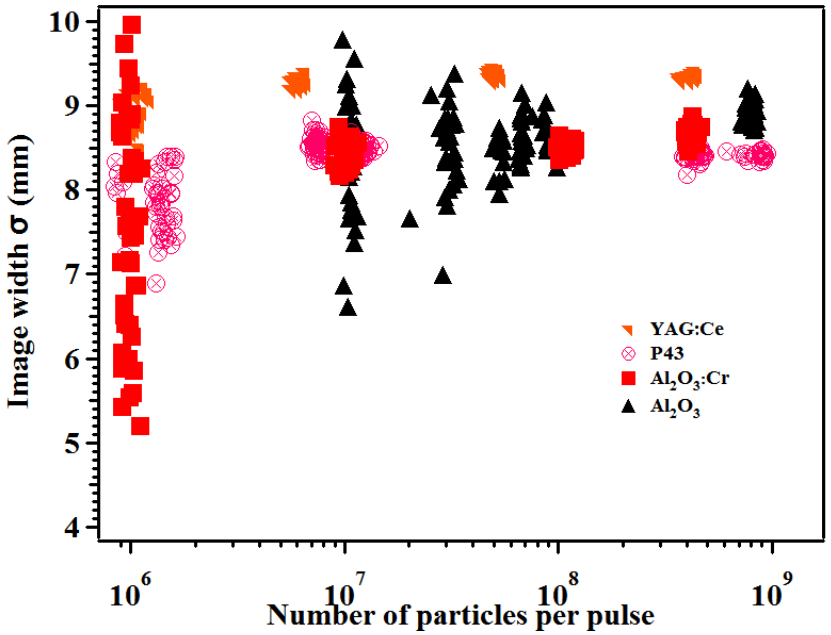


Figure A 3: Image width σ calculated for vertical direction using raw data (algorithm 1, Chapter 4.5) for Carbon ion beam.

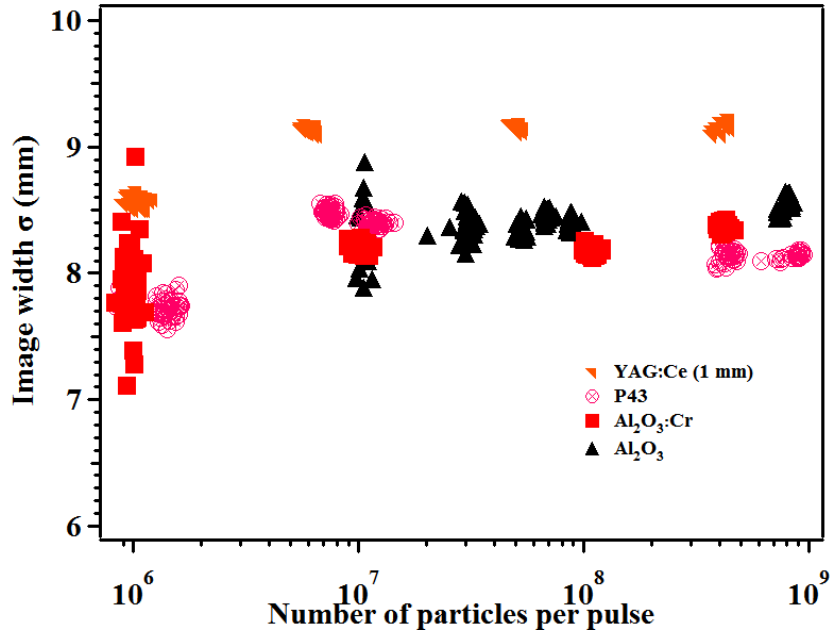


Figure A 4: Image width σ calculated for vertical direction using Gaussian fit (algorithm 4, Chapter 4.5) for Carbon ion beam.

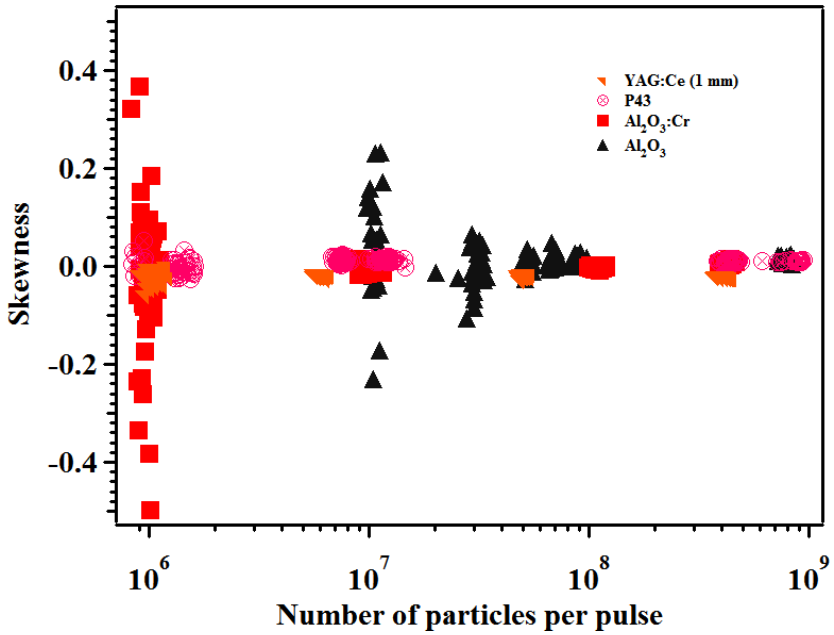


Figure A 5: The skewness γ calculated for vertical projection of Carbon ion beams.

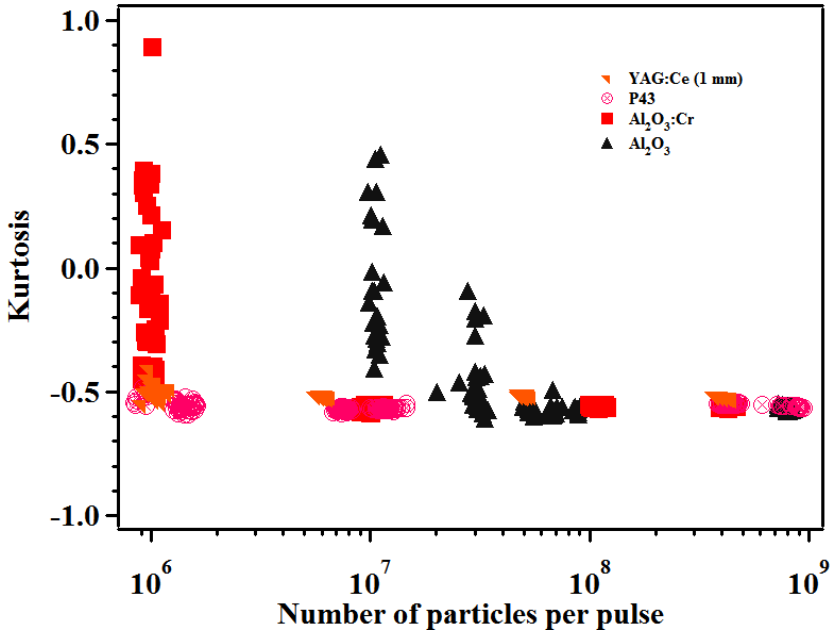


Figure A 6: The peakedness of the distribution kurtosis, κ calculated for the vertical projection of Carbon ions.

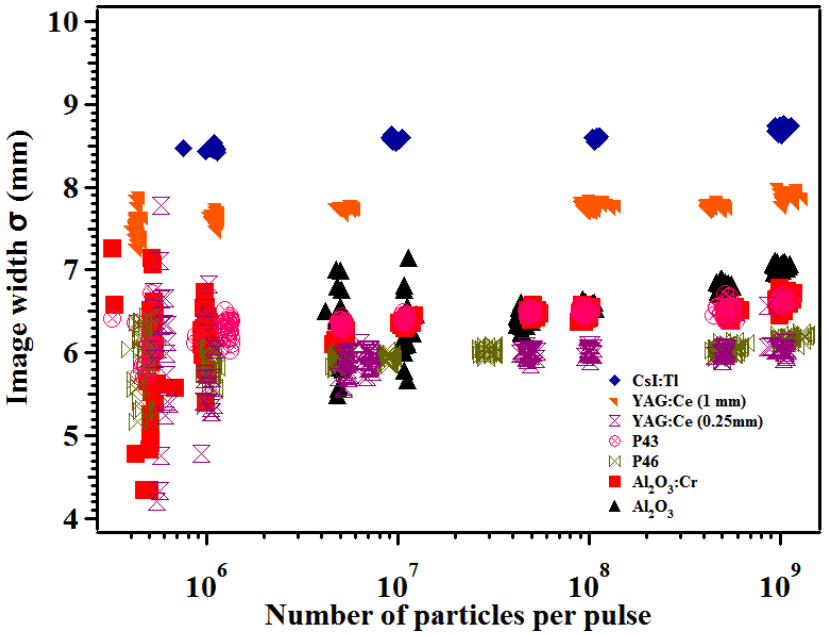


Figure A 7: Image width σ calculated for vertical direction using raw data (algorithm 1, Chapter 4.5) for Neon ion beam.

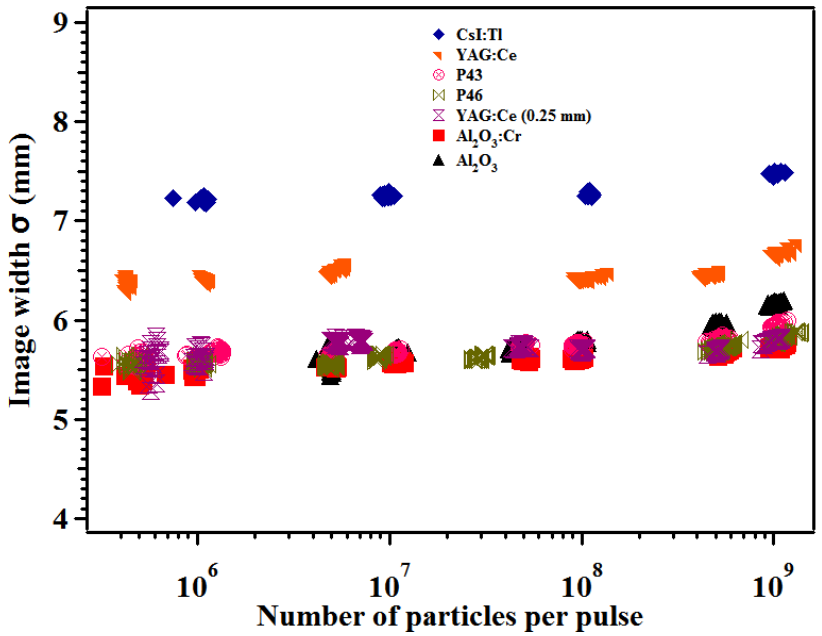


Figure A 8: Image width σ calculated for vertical direction using Gaussian fit (algorithm 4, Chapter 4.5) for Neon ion beam.

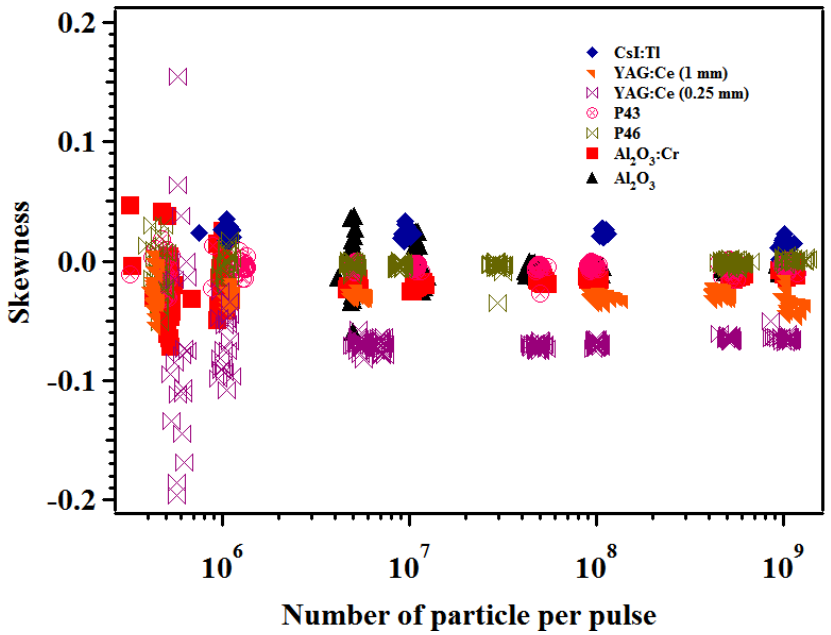


Figure A 9: The skewness γ calculated for vertical projection of Neon ion beams.

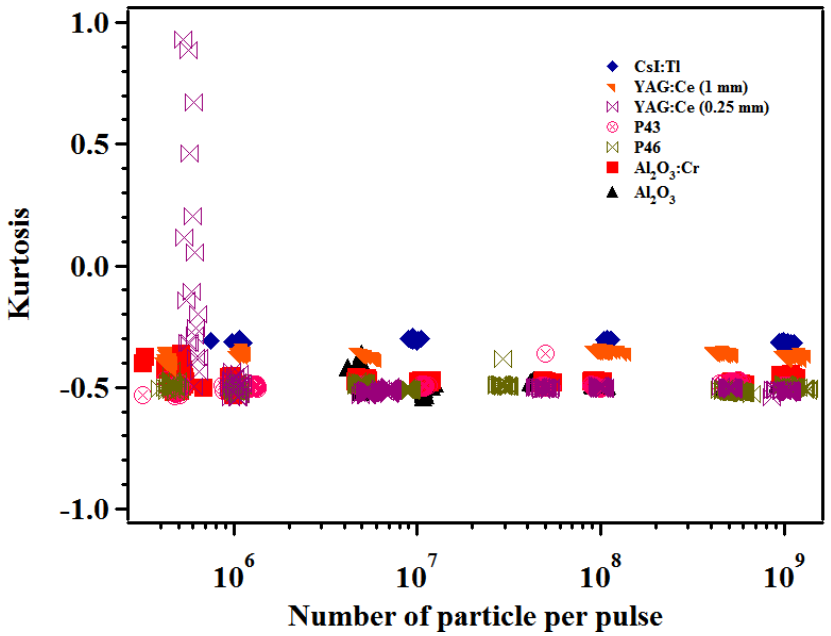


Figure A 10: The peakedness of the distribution kurtosis, κ calculated for the vertical projection of Neon ions.

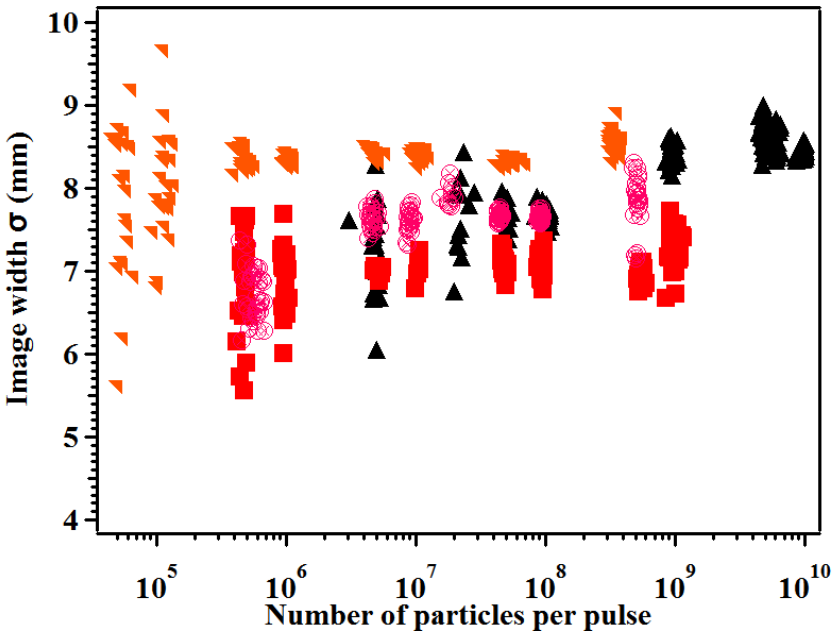


Figure A 11: Image width σ calculated for vertical direction using raw data (algorithm 1, Chapter 4.5) for Argon ion beam.

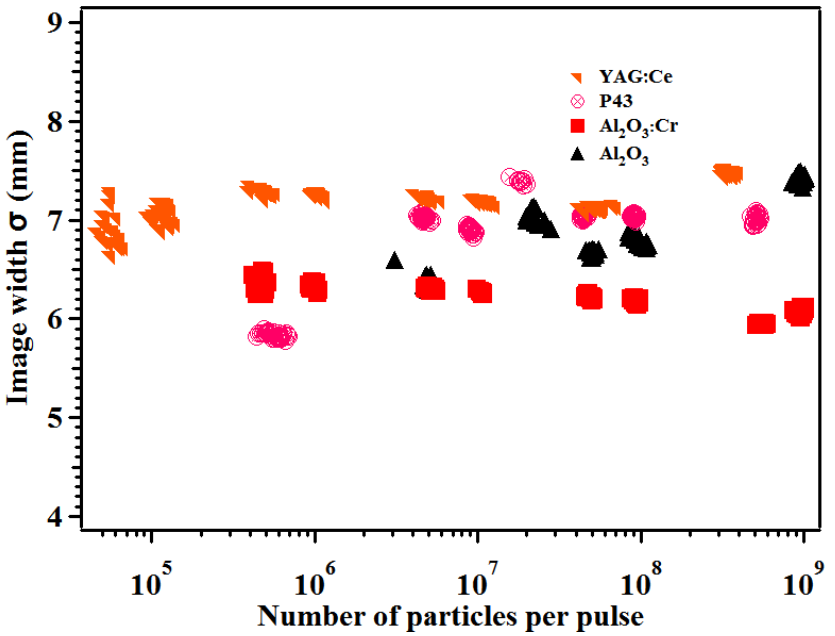


Figure A 12: Image width σ calculated for vertical direction using Gaussian fit (algorithm 4, Chapter 4.5) for Argon ion beam.

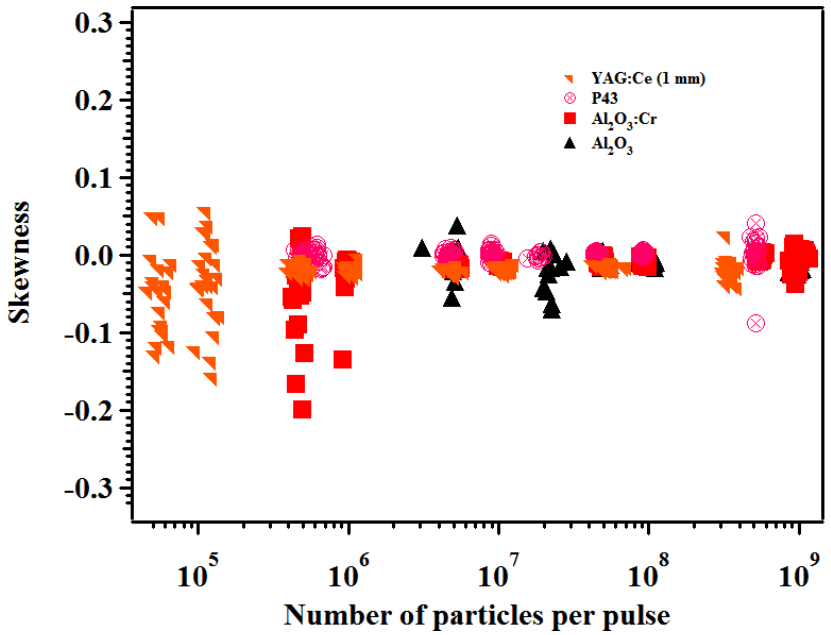


Figure A 13: The skewness γ calculated for vertical projection of Argon ion beams.

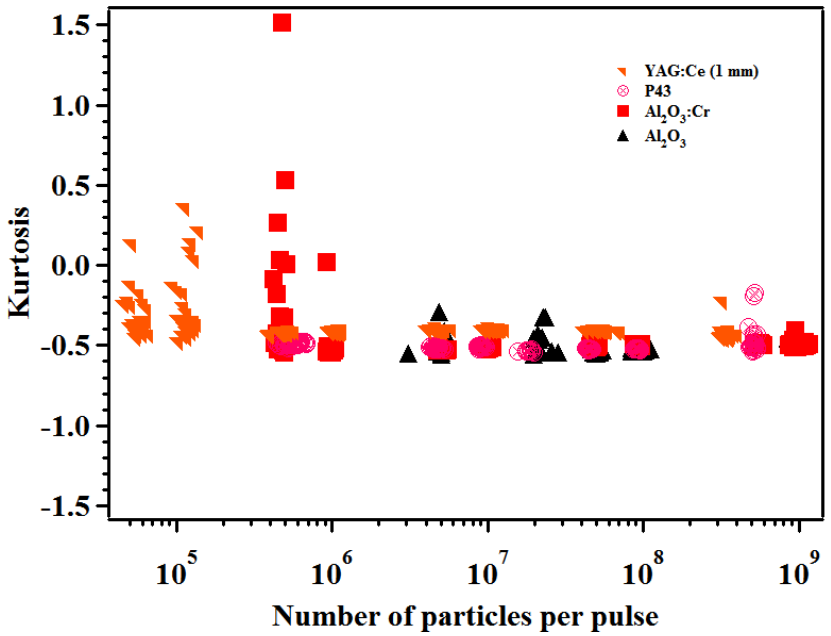


Figure A 14: The peakedness of the distribution kurtosis, κ calculated for the vertical projection of Argon ions.

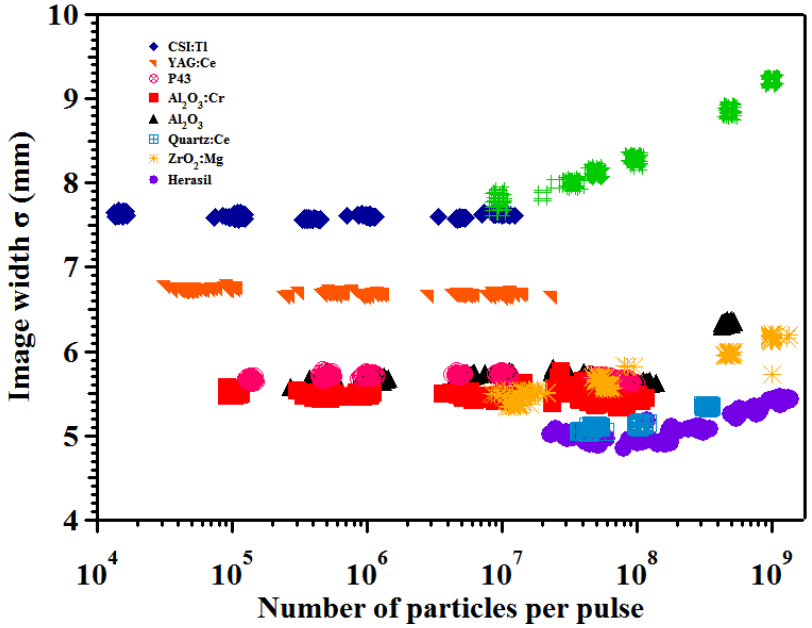


Figure A 15: Image width σ calculated for vertical direction using raw data (algorithm 1, Chapter 4.5) for Uranium ion beam.

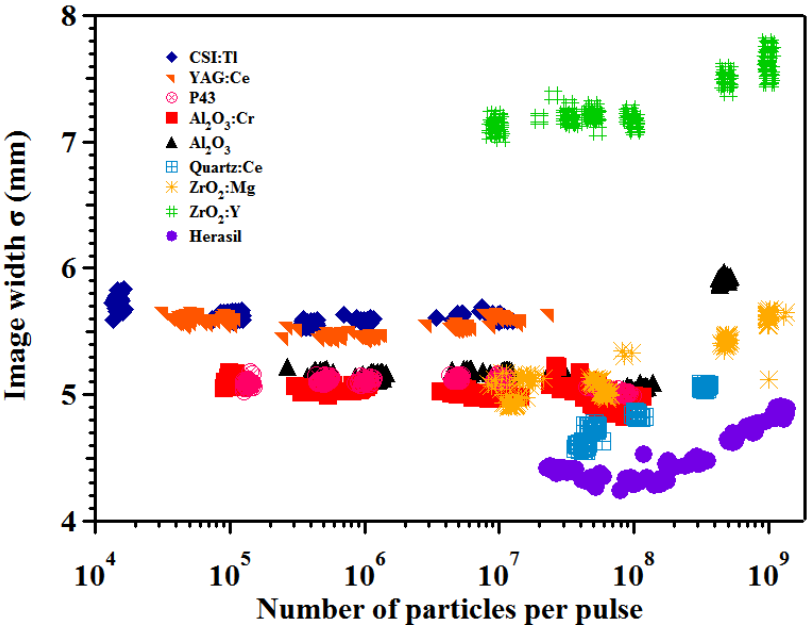


Figure A 16: Image width σ calculated for vertical direction using Gaussian fit (algorithm 4, Chapter 4.5) for Uranium ion beam.

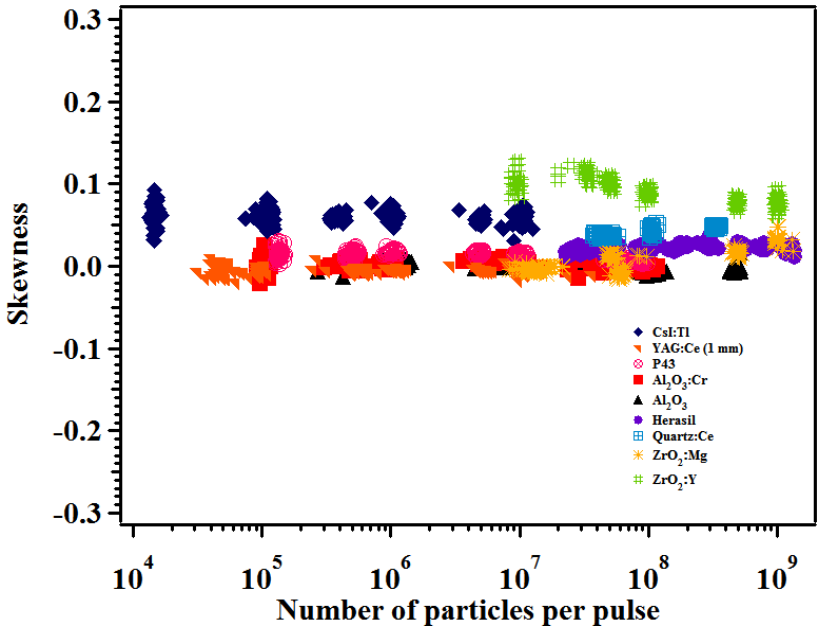


Figure A 17: The skewness γ calculated for vertical projection of Uranium ion beams.

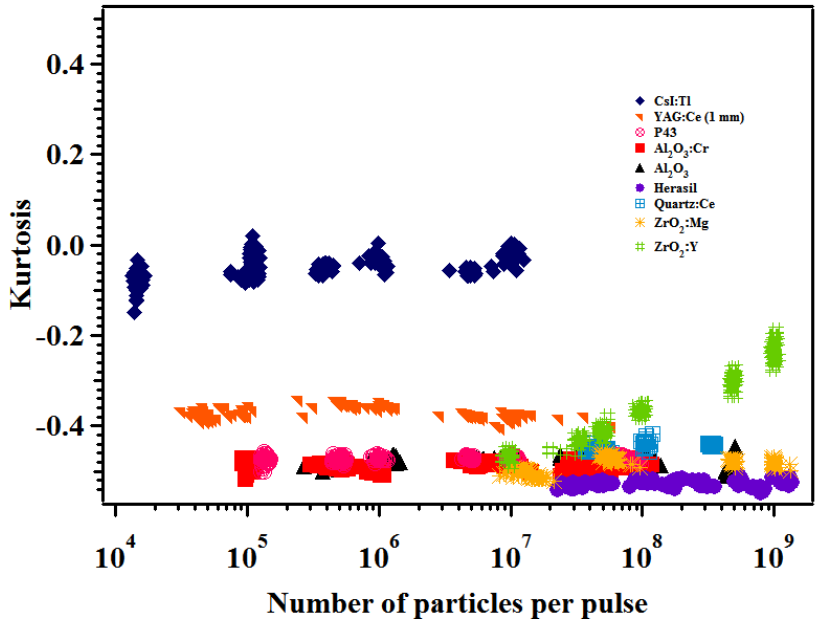


Figure A 18: The peakedness of the distribution kurtosis, κ calculated for the vertical projection of Uranium ions.

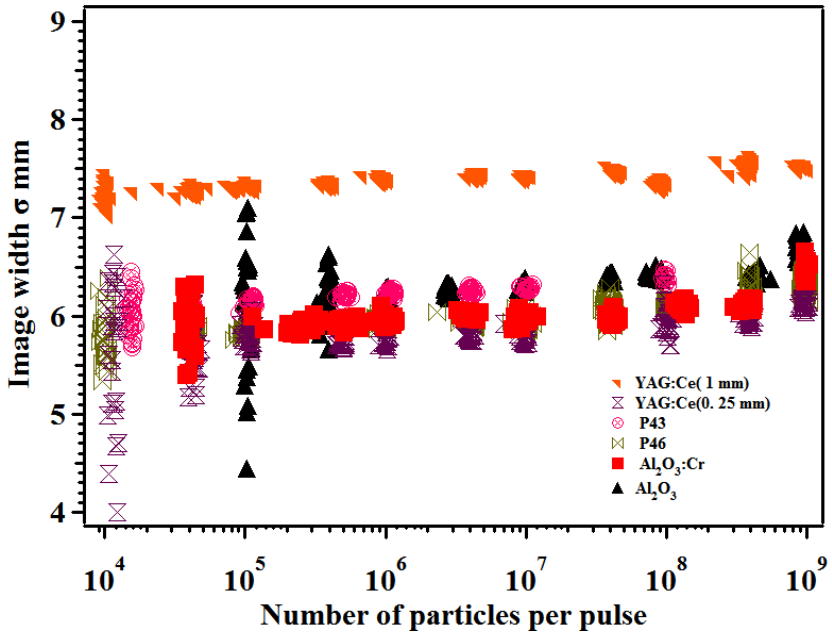


Figure A 19: Image width σ calculated for vertical direction using raw data (algorithm 1, Chapter 4.5) for Tantalum ion beam.

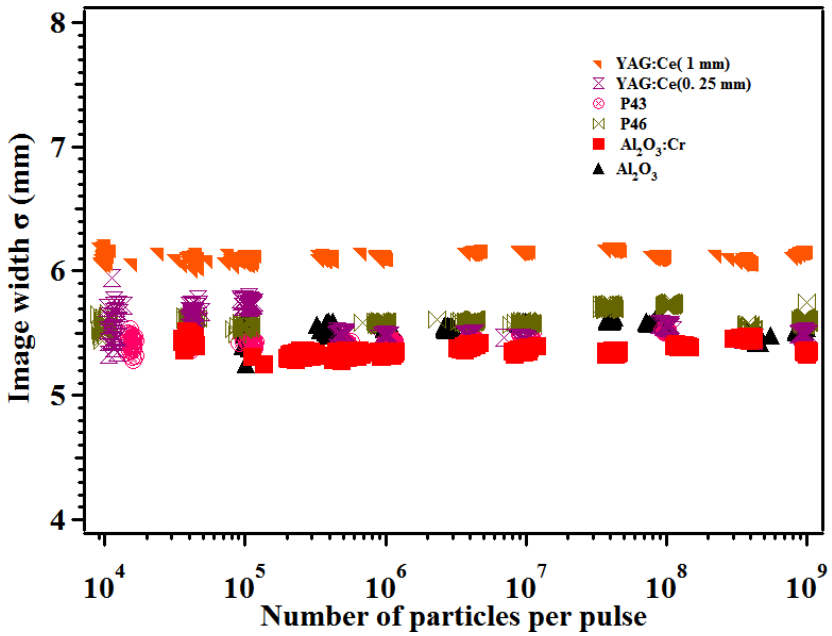


Figure A 20: Image width σ calculated for vertical direction using Gaussian fit (algorithm 4, Chapter 4.5) for Tantalum ion beam.

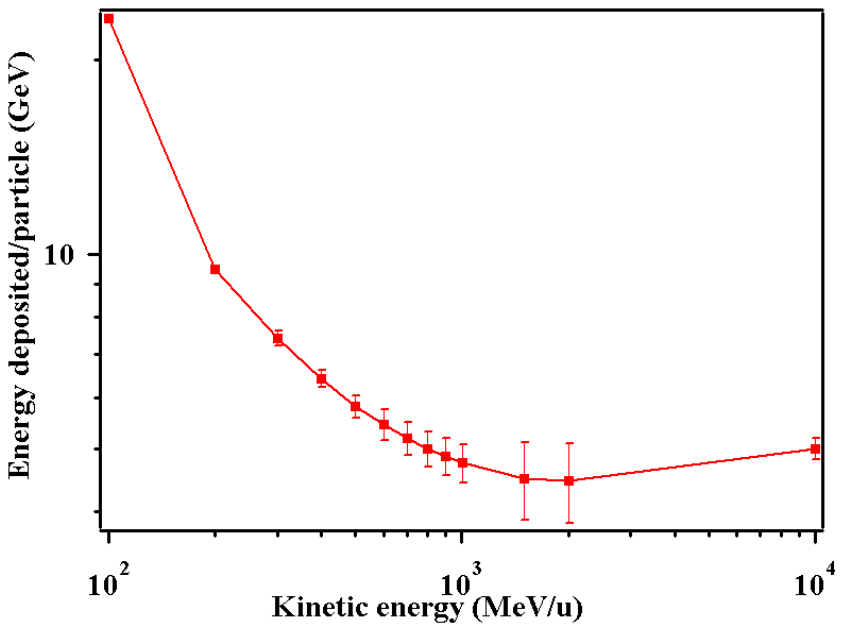


Figure A 21: Energy deposited in $Al_2O_3$:Cr a by single Uranium particle accelerated to different energy, calculated using SRIM 2008 program.

## Publications

- **K. Renuka**, F. Becker, W. Ensinger, P. Forck, R. Haseitl, B. Walasek-Höhne,“ *Imaging properties of scintillation screen for high energetic ion beams “IEEE Transactions on Nuclear Science 59*, pp. 2301-2306, 2012.

- **K. Renuka**, W. Ensinger, C. Andre, F. Becker, P. Forck, R. Haseitl, A. Reiter, B. Walasek-Höhne, “ *Transverse beam profile monitoring using scintillation screens for high energy ion beams “* Proceedings of Beam Instrumentation Workshop (*BIW*) Virginia, USA, pp. 183-185, 2012.

- **K. Renuka**, F. Becker, W. Ensinger, P. Forck, R. Haseitl, B. Walasek-Höhne,“*Scintillation screen investigation for 300 MeV/u ion beams*” p. 339, GSI scientific report 2011.

- P. Forck, C. Andre, F. Becker, R. Haseitl, A. Reiter, B. Walasek-Höhne, **R. Krishnakumar**, W. Ensinger, “*Scintillation screen investigations for high energetic ion beams at GSI”*, Proceedings of 10th European Workshop on Beam Diagnostics and Instrumentation for Particle Accelerators *(DIPAC),* Hamburg, Germany, pp. 170-173, 2011.

- B. Walasek-Höhne, C. Andre, F. Becker, W. Ensinger, P. Forck, E. Guetlich, K. Guetlich, R. Haseitl, **R. Krishnakumar**, A. Reiter,” *Investigation of scintillation screens for FAIR”,* pp. 312, GSI scientific report 2010.

## Conferences and Workshops

- Oral presentation in workshop on ‘Scintillation screen application in beam diagnostics’, Feb 2011, GSI, Darmstadt, Germany, http://www-bd.gsi.de/ssabd/index.html

- Oral presentation in 11th International conference on ‘Inorganic scintillators and their application’, (SCINT 2011), Sep 2011, Giessen, Germany.

- Poster presentation in 15th Beam Instrumentation Workshop (*BIW*), Apr 2012, Newport News, USA.

- Participation in 8th International conference on ‘Luminescent detectors and transformers of ionizing radiation (LUMDETR 2012), Sep 2012, Halle (Saale), Germany.

.

# Acknowledgement

It would not have been possible to write this doctoral thesis without the help and support of the kind people around me. I use this opportunity to express my sincere thanks to,

- Prof. Dr. Ensinger for accepting me as a PhD student, support, encouragement and supervising during the study.
- Dr. M. Schwickert for the nice opportunity to carry out my doctoral study in Beam diagnostics department of GSI.
- Dr. P. Forck for introducing me the field of accelerators. His esteemed supervision, guidance and moral support helped me to do this doctoral research.
- Dr. F. Becker for guidance and inspiration to learn about the accelerators, helping in designing and building the experimental set up.
- B. Walasek-Höhne, C. Andre and R. Haseitl for optical setup installations and their moral support during beam time and for correcting manuscripts.
- Dr. A. Reiter and Dr. E. Gütlich for many scientific discussion and suggestion in the detailed data analysis process.
- Dr. J. Zimmermann for absorption and transmission spectra measurements and many scientific discussions concerning the luminescence properties of the materials.
- Dr. J. Brötz and S. Lederer for the XRD measurements and result analysis.
- D. Lyakin and R. Boywitt for explaining the electrical, electronic operations and programming the linear drive.
- K. Gütlich for CAD drawings of the target holder and the experimental set up.
- The operators of the GSI for their skilled beam alignment to the target location.
- Dr. Beatrice Schuster and Dr. M. Tomut for helping me in handling Raman spectrometer and many scientific discussions on the obtained results.

Finally, I would like to acknowledge all the members of Beam Diagnostics department of GSI for their friendly nature and support throughout the study.

Thank you!

# Curriculum vitae

## Personal data

| | |
|---|---|
| Name | Renuka Krishnakumar |
| Date of Birth, place | 28.06.1985 in Karur, Tamilnadu, India |

# Education

| | |
|---|---|
| 10.2009 - 12.2014 | Doctoral student in Material Analysis Department, TU Darmstadt "Scintillation Screen Materials for Beam Profile Measurement of High Energy Ion Beams" |
| 08.2007 - 03.2008 | Certificate course in Industrial Pollution Control, Annamalai University, Chidambaram, India |
| 07.2005 - 05.2007 | M.Sc Chemistry, P.G.P College of Arts and Science, Namakkal, India |
| 07.2002 - 05.2005 | B.Sc Chemistry, Sri Saratha Niketan College of Science for Women, Karur, India |
| 07.2000 - 05.2002 | St. Theresa's Girls Hr. Secondary School, Karur, India |
| 06.1989 - 05.2000 | St. Theresa's Matriculation School, Karur, India |

# Work Experience

| | |
|---|---|
| 10.2009 - 09.2012 | Guest worker in GSI Helmholtz Centre for Heavy Ion Research, Darmstadt |
| 12.2006 - 02.2007 | Internship in SPIC Pharmaceuticals, Cuddalore, India |
| 05.2006 - 06.2006 | Internship in Tamilnadu Newsprint and Paper Limited (TNPL), Karur, India |